Effects of Longitudinal Disorder on the Magnetic Field Distribution in $Bi_2Sr_2CaCu_2O_{8+\delta}$

A Dissertation

Presented to

The Faculty of the Department of Physics

The College of William & Mary in Virginia

In Partial Fulfillment

Of the Requirements for the Degree of

Doctor of Philosophy

---

by

Xuewen Wan

2002

APPROVAL SHEET

This dissertation is submitted in partial fulfillment of

the requirements for the degree of

Doctor of Philosophy

Xuewen Wan

Xuewen Wan

Approved, August 2002

William J. Kossler
Thesis Advisor

Kenneth G. Petzinger

Harlan E. Schone

Anne C. Reilly

Carey E. Stronach

Carey E. Stronach
Virginia State University

To my wife, Juan Zhou, for her love and encouragement

Table of Contents

ACKNOWLEDGMENTS

I would like to thank my adviser, Dr. William J. Kossler, for brilliant suggestions and ideas to improve this work. He proved to be not only an outstanding researcher but an incredible human being and I extend my gratitude to him for the great effort he devoted to this project in particular and to my professional formation in general. I consider myself very lucky to have been his disciple in the μSR research field. He is truly a mentor and a physicist who seeks nothing but truth.

I am also very grateful to Dr. Carey E. Stronach and Dr. David R. Noakes, advisors for my master's degree, for introducing me into the μSR research field and for their encouragement and support throughout the whole project.

I also want to thank the members of my defense committee for agreeing to review and evaluate my work.

Special thanks to Dr. John D. Walecka and Dr. William E. Cooke, Chairs of the Physics Department, who created a wonderful academic environment here. Thanks are also due to the administrative and technical staffs of the department, Paula C. Perry, Sylvia J. Stout, Dianne B. Fannin, Eric J. Dawnkaski, and Edward H. Lawrence.

I am grateful to Dr. Kenneth G. Petzinger, Christopher D. Carone, and Henry Krakauer for their guidance in my course work.

Special thanks to my Chinese fellow students in the department, Shuquan Nie, Zhigang Wu, Donghua Zhou, Dongmei Wang, Wei Yang, Xin Zhao, and Ping Tang for their trust, useful discussions and frequent help whenever I encountered difficulties.

This work would have not been possible without the support of S. Kreitzman, B. Hitti and other members of the TRIUMF technical staff.

Last, but certainly not least, I would like to thank my family for their unconditional care, love and support.

ABSTRACT

Transverse Field muon spin relaxation (TF-μSR) experiments were performed in external magnetic fields 1.0, 2.7, 3.0, 4.5, 5.5, 6.0 and 7.0 T along the Bi2212 crystalline c-axis. For the first time, the heterodyned fitting analysis technique shows that the field profiles on the ab basal planes of single crystal Bi2212 are symmetric in all experimental fields 1.0-7.0 T and at all experimental temperatures 2.0-90.0 K. The muon spin relaxation rates due to the mixed state of Bi2212 were found to increase linearly from 0 μs^{-1} at the transition temperature, 90.0 K, to about 1.0 μs^{-1} at the lowest temperature, 2.0 K. The relaxation rates have much less field dependence than the temperature dependence and the field dependence of the relaxation rate is of opposite sign to that seen for YBCO, which is undoubtedly due to vortex lattice disorder caused by the weak coupling between the CuO planes. The scaled magnetic field penetration depths $\frac{\lambda}{\lambda(0)}$ were found to be independent of magnetic field B in the temperature range 0-50.0 K. Fitting $\frac{\lambda}{\lambda(0)}$ by currently available models was attempted. A proposed pancake vortex disorder model strongly suggests pancake disordering at all temperatures including 2.0 K, the lowest temperature reached in our experiment. Our experiments and the computer simulation from the pancake vortex disorder model showed that μSR data in this temperature and field range are attributed to the 2-D anisotropic vortex characteristics of Bi2212.

Effects of Longitudinal Disorder on the Magnetic Field Distribution in $Bi_2Sr_2CaCu_2O_{8+\delta}$

Chapter 1

Introduction

1.1 General Introduction

Muon spin rotation and relaxation has been used in this thesis work to investigate the static and dynamic electronic and magnetic structures of the vortex state of the type II superconductors. The study helps us to better understand the vortex phase diagram and other features of type II superconductors below the critical temperature. The static and dynamic magnetic field behavior of the vortex state structure in highly anisotropic superconductors such as $Bi_2Sr_2Ca_{n-1}Cu_n\ O_{4+2n}$ (BSCCO) is of a nature not usually encountered in the more conventional superconductors. We used an array of well characterized $Bi_2Sr_2CaCu_2O_{8+\delta}$ (Bi2212) single crystal samples in the BSCCO family to continue our study on the exotic vortex behavior in these highly anisotropic systems.

The Bi2212 system has been studied extensively in the past ten years with NMR, STM and ARPES techniques. However the research work on the magnetic field distribution *f(B)* on the *ab* basal planes and the vortex lattice disorder in this highly anisotropic system was sparse for applied external magnetic fields of several Tesla. The muon's ability to occupy interstitial and substitutional sites provides information on the magnetic field distribution

due to the disordered vortex lattice, which is not available to the other techniques listed above.

In chapter 1, we will review briefly muon spin rotation and relaxation technique, which was used in our study. In chapter 2, the general characteristics of the magnetic field distribution in type II superconductors will be discussed. The focus of Chapter 3 is to review some background studies on Bi2212, where the effects of the vortex disorder on the magnetic field distribution will be discussed. In Chapter 4, we will describe the experimental details of this study, present the experimental data and analyze the results. Finally the pancake vortex disorder model will be proposed and used to explain all the major features of the experimental results.

1.2 Muons and the Origin of the Muon Spin Rotation Technique

Muons (positive muons or negative muons) were first discovered in a cosmic-ray experiment in 1937 by Neddermeyer and Anderson and can be produced in various high energy processes via elementary particle decays such as kaon decay or pion decay. In 1956 and 1957, T.D. Lee and C.N. Yang theorized that processes governed by the weak nuclear interaction might not have corresponding mirror image processes of equal probability, i.e., parity might be violated. This parity violation was first observed in beta-decay of Co-60 by C.S. Wu *et al.* Soon after that, experiments were performed at the Nevis cyclotron by R.L. Garwin, L.M. Lederman and M. Weinrich and at the Chicago cyclotron by J.I. Friedman and V.L. Telegdi in 1957, which showed a dramatic parity violating effect in the decay of pions to muons and

the subsequent decay of muons to electrons and neutrinos. The Nevis experiment was the precursor of modern μSR.

The Muon Spin Rotation, Relaxation and Resonance(μSR) technique [Seeger 78, Chappert and Grynszpan 84, Schenck 85, Chappert and Yaouanc 86, Cox 87, Brewer 94, Karlsson 95, Schenck and Gygax 95, Schatz and Weidinger 95, Reotier and Yaouanc 97] uses the muon and its parity violating characteristics to probe various properties of materials and is becoming a valuable tool in atomic, subatomic and other fundamental physics disciplines. μSR requires low energy muons in order to stop the beam in samples of convenient thickness or stopping power, which are available in the required intensities only from the ordinary two-body decay of charged pions. The pions are generated at rest in the surface layer of a primary production target (C or Be), from which the muons emerge (in the rest reference frame of pion) with a momentum of 29.7 MeV/c and a kinetic energy of 4.1 MeV. The lifetime of a free charged pion is 26.03 ns.

From the electro-weak nuclear theory, we know the most remarkable feature of the free positive pion decay is that it maximally violates the parity symmetry, causing the muons to be emitted with perfect spin polarization. This is the greatest advantage of the μSR technique as a magnetic resonance technique, whereas NMR and ESR rely upon a thermal equilibrium spin polarization, usually achieved at very low temperatures in strong magnetic fields. μSR begins with a perfectly polarized probe, regardless of conditions in the medium to be studied. It also implies that muon spin degrees of freedom usually start their evolution as far from thermal equilibrium as conceivable. The property of the muon decay positron to be emitted along the spin of the muons is another consequence of the parity violation in the weak interaction that allows us to read out the information encoded in the

evolution of an initially polarized muon spin ensemble. The information is delivered to the experimenter and scientist in the form of rather high energy (up to 52 MeV, see Appendix A) positrons, which readily penetrate sample holders, cryostats or ovens and the detectors used to establish the time and direction of the muon decay. The decay probability of the muon depends on the energy of the emitted positrons and the angle between the muon spin direction and the direction of the positron's emission. The asymmetry $A(t, E)$ increases monotonically with the positron's energy and is 100% for the maximum energy. In real experiments, low energy positrons do not penetrate materials to trigger the detectors, or are curled up by applied field, so the efficiency for detecting positrons $f(E)$ is energy E dependent, forcing an integration over $A(t, E) \cdot f(E)dE$ to obtain the average asymmetry $A(t)$, where E is also a function of the spanned solid angle.

As a useful microprobe, μSR is extremely sensitive to the magnetic environment; for example, neighboring dipoles as small as 0.001 μ_B can be detected. μSR is also an effective probe for changes in spin arrangement such as spin flip transitions, spin reorientations, or antiferromagnetic transitions etc. In summary, μSR can easily detect small distributions in the field at the muon site and is sensitive to rather subtle distortions in the spin structure or ordered magnets.

1.3 Muon Spin Depolarization Asymmetry

μSR measurements fall into three geometric categories: longitudinal (LF), transverse (TF), and zero (ZF) field, depending on the direction of the applied magnetic field relative to the direction of the initial muon spin polarization. Fig. 1.1 and fig. 1.2 show the schematic

diagram of a TF-μSR setup and an experimental histogram.

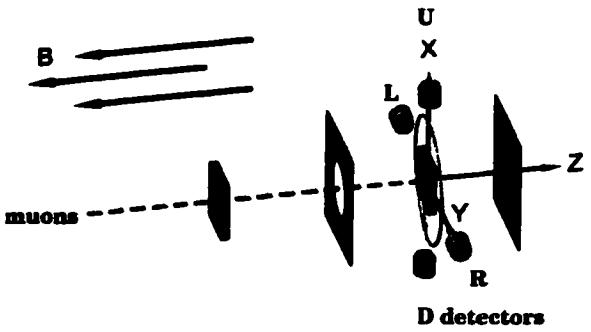

Figure 1.1: A typical TF-μSR experiment setup.

The decay positrons are usually collected and time stamped in the up (U), down (D), left (L) and right (R) detectors. The detection rate in any of these four detectors with direction $\vec{d_i}$ is equal to:

$$D_R(t) = N(t)\ a_i\ (1 + \epsilon_i \vec{P}(t) \cdot \vec{d_i}) \tag{1.1}$$

For transverse field μSR, the equation above can be written as

$$D_R(t) = N_0\ e^{-\frac{t}{\tau}}\ a_i\ [1 + \epsilon_i\ G_T(t) cos(\omega_\mu t + \phi_i)] \tag{1.2}$$

where $N(t) = N_0\ e^{-\frac{t}{\tau}}$ is the muon decay rate in the sample. a_i, ϵ_i and ϕ_i are for the detector efficiency, sensitivity and phase of detector to the muon's polarization, $\vec{P}(t)$, i denotes up, down, left or right detectors. Usually, these four detectors are arranged so that they are $\frac{\pi}{2}$ (1.57) out of phase sequentially. The four positron histograms show that this is always the case in the spectra when the external applied magnetic field is low. For example, the four phases from our 70 G transverse-field calibration run are 2.036(5), 0.454(5), -1.164(3) and -2.699(6) radian in sequence. The muon spin-asymmetry (raw asymmetry) plot can be

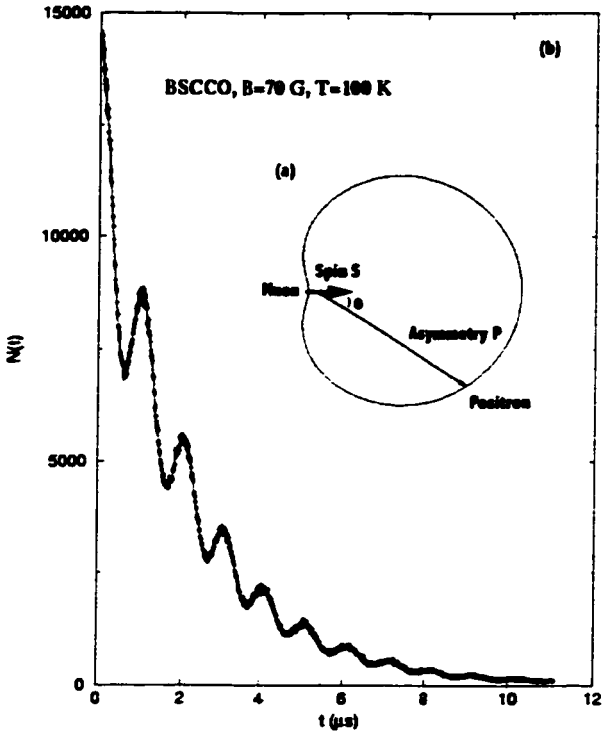

Figure 1.2: Asymmetry of the muon radioactive decay. (a) The polar diagram shows the probability of a decay positron being emitted at an angle θ to the instantaneous spin vector; (b) A μSR histogram, showing the radioactive decay curve modulated by the muon polarization precession.

constructed in the standard way by taking the ratio:

$$A(t) = \frac{U(t) - D(t)}{U(t) + D(t)}. \tag{1.3}$$

where $A(t)$ is the asymmetry of muon spin relaxation, which is directly proportional to the autocorrelation function $\langle \mathbf{S}_\mu(t) \cdot \mathbf{S}_\mu(0) \rangle$, where $\mathbf{S}_\mu$ is the Pauli spin operator and the brackets refer to an average over all possible nuclear states. $U(t)$ and $D(t)$ are the positron count rates in the up and down detectors, which are approximately π out of phase. From the formula of error propagation, we know the error of A, σ_A can be written as (t is implied

in each of the following U and D)

$$\begin{aligned} \sigma_A &= \frac{\sqrt{(2\ U\ \sigma_D)^2 + (2\ D\ \sigma_U)^2}}{(U+D)^2} \\ &= \frac{2\sqrt{U\ D\ (U+D)}}{(U+D)^2}\ (\ \sigma_D^2 \sim D,\ \sigma_U^2 \sim U\ ) \end{aligned} \tag{1.4}$$

Assuming $U(t) = N_0\ \mathrm{e}^{-\lambda t}\ (1 + A(t))$ and $D(t) = N_0\ \mathrm{e}^{-\lambda t}\ (1 - A(t))$, the equation above can be simplified to

$$\sigma_A = \sqrt{\frac{1 - A^2}{2\ N_0\ e^{-\lambda t}}} \tag{1.5}$$

Furthermore, the total counts N_T collected in the two up and down detectors can be derived as

$$\begin{aligned} N_T &= \int_0^\infty (U(t) + D(t))\ dt \\ &= \int_0^\infty [N_0 e^{-\lambda t}(1 + A(t)) + N_0 e^{-\lambda t}(1 - A(t))]\ dt \\ &= \int_0^\infty 2\ N_0 e^{-\lambda t} dt \\ &= \frac{2\ N_0}{\lambda} \end{aligned} \tag{1.6}$$

Then eq. 1.5 can be further written as

$$\begin{aligned} \sigma_A &= \sqrt{\frac{1 - A^2}{\lambda\ N_T\ e^{-\lambda t}}} \\ &\simeq \sqrt{\frac{e^{\lambda t}}{\lambda\ N_T}} \end{aligned} \tag{1.7}$$

A plot of σ_A vs. N_T is shown in fig. 1.3 from which we can understand why we usually set up the appropriate experimental run time so that N_T is about 10^7. More generally, if the

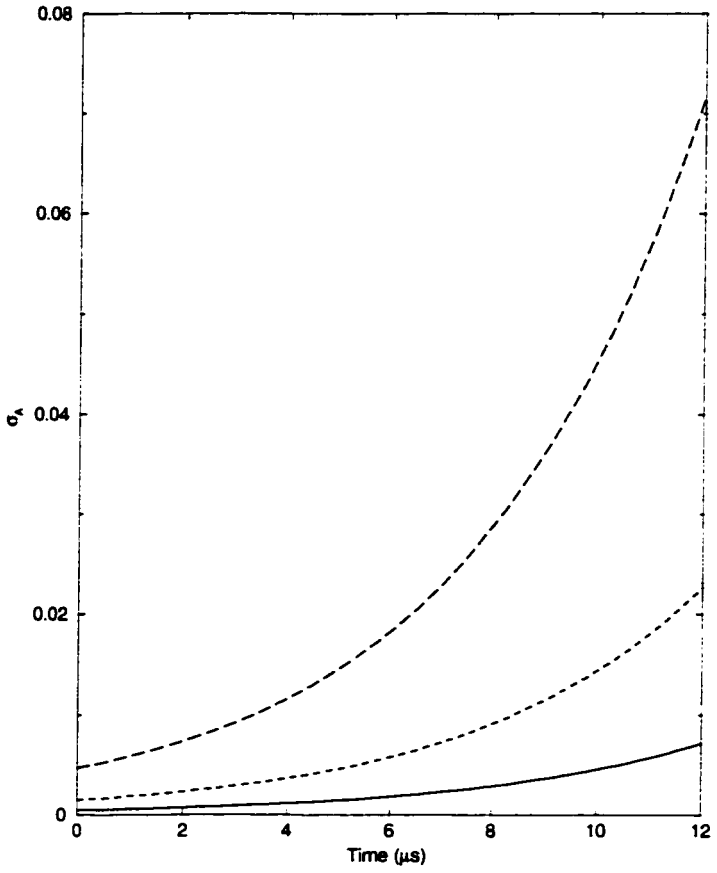

Figure 1.3: The asymmetry error as a function of total experimental counts in paired detectors. Long dashed line: $N_T = 10^5$, dashed line: $N_T = 10^6$, solid line: $N_T = 10^7$.

detectors are not identical and there are background counts in each histogram, we know

$$D_R(t) = N_0\, e^{-\frac{t}{\tau}} a_i\, (1 + \epsilon_i\, \vec{P}(t) \cdot \vec{d}_i) + B_i \tag{1.8}$$

For up and down detectors, the equation above can be written as

$$U_u(t) = N_u\, e^{-\frac{t}{\tau}}\, [1 + \epsilon_u P(t)] + B_u \tag{1.9}$$

$$U_d(t) = N_d\, e^{-\frac{t}{\tau}}\, [1 + \epsilon_d P(t)] + B_d \tag{1.10}$$

The muon spin depolarization function $P(t)$ and its error σ_p can be derived as

$$P(t) = \frac{\alpha U(t) - D(t)}{\alpha\epsilon_d U(t) + \epsilon_u D(t)} \tag{1.11}$$

$$\sigma_p = \frac{\alpha(\epsilon_u + \epsilon_d)\sqrt{[D(t)\sigma_u]^2 + [U(t)\sigma_d]^2}}{[\alpha\epsilon_d U(t) + \epsilon_u D(t)]^2} \tag{1.12}$$

Here $\alpha = \frac{N_d}{N_u}$ and $U(t) = U_u(t) - B_u$, $D(t) = D_d(t) - B_d$. If $\epsilon_u = \epsilon_d$, the equations above can be simplified to the previous case. The corresponding theoretical expression for $P(t)$ in terms of intrinsic local field parameters in anisotropic superconductors was derived by Barford and Gunn [Barford 88].

An alternate way to study the muon spin relaxation behavior is to observe the phase diagram plot i.e. P'(t) vs. P(t), in which the instantaneous muon polarization P(t) and its changing rate (or first derivative) are clearly shown. Pattern recognition techniques may be further used to study this kind of plot.

In a μSR experiment the spin-polarized muons are assumed to stop at random positions within the sample, thermalize rapidly on time scales of 10^{-10} s without losing initial polarization and then precess in the local internal magnetic fields $B(r)$. The precession frequency is $\gamma_\mu B$, where $\gamma_\mu = 135.5\ MHz/T$ is the gyromagnetic ratio of the muon. In almost all known cases, the positive muon stops at interstitial sites due to the electrostatic repulsion by atomic nuclei. In HTSC there is evidence that the muon binds to a negatively charged oxygen ion, which may or may not belong to the CuO_2 plane. [Brewer 90] However, since the vortex lattice spacing in a typical μSR magnetic field is much larger (several hundred times) than the dimensions of the crystallographic unit cell, we still consider that the muon stops randomly inside the sample. [Forgan 97]

In the vortex state of a type-II superconductor, muons experience a spatially varying

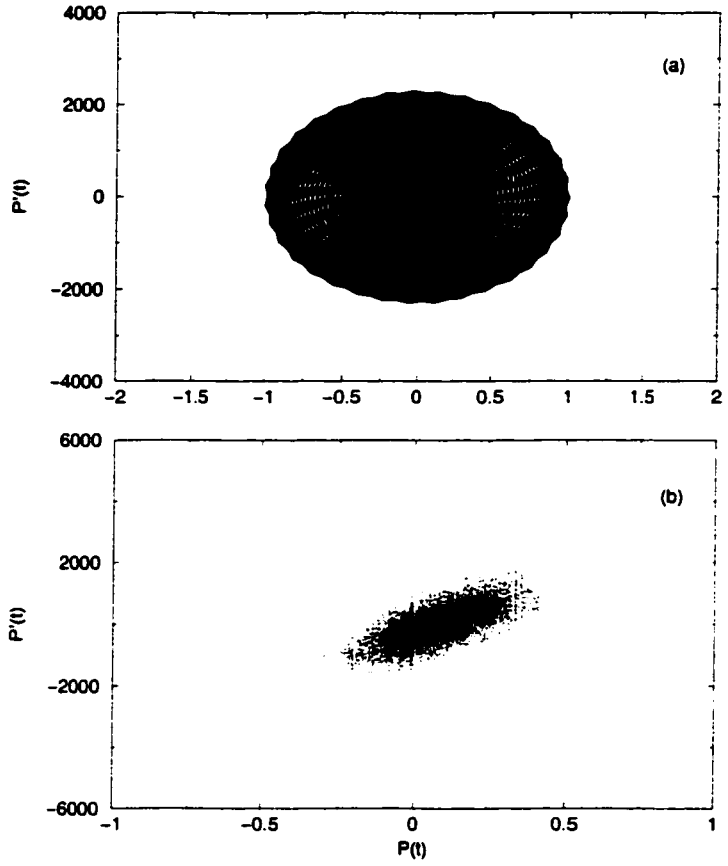

Figure 1.4: (a) The predicted phase plot for a Gaussian Oscillating relaxation function; (b) The experimental phase plot for a Bi2212 sample at T=2 K in an external magnetic field B=2.7 T. The deviation from a simple Gaussian Oscillating relaxation function is clearly seen without fitting the experimental data.

magnetic field due to the periodical arrangement of the vortices. If we assume the field is along the z direction, the time evolution of the x or y components of the total muon polarization is

$$P(t) = \int_0^\infty f(B)\cos(\gamma_\mu Bt + \theta)dB \tag{1.13}$$

where $f(B)$ is the μSR line shape and θ is the initial phase of the muon spin. The envelope of the oscillating muon spin polarization $P(t)$ decays or dephases with increasing time according to the width of $f(B)$.

In the real material, there are perturbations of the periodic vortex lattice caused by the random pinning of the vortices and fluctuations in temperature and the applied magnetic field. All these additional sources of field inhomogeneity can often be accounted for by multiplying the muon polarization function by a factor $G_T(t)$, so that

$$P(t) = G_T(t) \int_0^\infty f(B) \cos(\gamma_\mu B t + \theta) dB \tag{1.14}$$

where $G_T(t)$ can be a simple Gaussian or Exponential function to more complicated functions.

If the local fields that the muons feel are not unique (there is a distribution of magnetic field $f(B)$ or $f(|\mathbf{B}|)$, for the difference between component and magnitude field distribution, see [Wan 99A]), consequently the muons will precess under different frequencies which causes a depolarization of the muons ensemble's spins. The second moment of the field distribution $f(B)$ indicates how fast the muons depolarize and thus it is called the relaxation rate σ. It has been shown theoretically that σ is highly sensitive to the type of disorder of vortex lattice in HTSC. [Brandt 91] For example, randomly positioned stiff parallel flux lines tend to increase σ, whereas vortex-dot fluctuations may decrease σ. There are several ways to extract the relaxation rate σ: we can best guess and assume the depolarization function $P(t)$ to fit the μSR spectra in the time domain and thus extract the relaxation rate parameter in the fitting procedure; the Fourier Transformation of μSR spectra indicates the magnetic field distribution inside the sample, we then calculate the second moment of the field distribution to get the relaxation rate. Note that the calculation of the second moment from the discretized field distribution data depends on the field channel width Δ,

there exists the following relation:

$$\begin{aligned}\sigma^2 &= \frac{\int B^2 f(B)dB}{\int f(B)dB} - \left(\frac{\int Bf(B)dB}{\int f(B)dB}\right)^2 \\ &\approx \frac{\sum B^2 f(B)dB}{\sum f(B)dB} - \left(\frac{\sum Bf(B)dB}{\sum f(B)dB}\right)^2 - \frac{\Delta^2}{12} \\ &= \sigma_{data}^2 - \frac{\Delta^2}{12} \end{aligned} \tag{1.15}$$

Simulation shows that as long as the channel width Δ is smaller or comparable with the second moment (relaxation rate), σ_{data} is a good estimate of σ. For any μSR spectra in a 10 μs time window, the ideal minimum relaxation rate we can extract from data is 0.1 μs^{-1}. If we consider the channel width effect above, the minimum relaxation rate is about 0.29 μs^{-1}.

High Temperature SuperConductor (HTSC) materials are ideally suited to be investigated by μSR, since implanted muons remain static over the temperature range below T_c. It is possible that a muon might modify the superconducting properties over a region ξ around itself, however, this will not appreciably alter the magnetic field at the muon site. Since the magnetic field at any point is determined by supercurrents flowing in a region $\sim \lambda^3$ in size, which is many orders of magnitude larger than ξ, so we think the muons should still be able to obtain an unbiased sample of the magnetic field distribution.

In general, there are three possible factors that contribute to the muon spin relaxation in transverse field below T_c: (1) inhomogeneity of the magnetic field due to the vortex structure and imperfect field penetration in a type II superconductor; (2) static random local fields if the superconductivity is associated with magnetic ordering; (3) dynamic processes due to fluctuating local fields. [Kossler 87]

The local fields **B** can either be intrinsic, as they are for ordered magnets and spin glasses, or induced by an external field, as for the vortex lattice of a type II superconductor. By measuring the distribution of precessing frequencies, in the mixed phase of a type-II superconductor, the probability distribution or the line shape $f(|\mathbf{B}|)$ of the internal field values can be extracted. The field distribution $f(|\mathbf{B}|)$ may be dependent on [Luke 00] the lattice geometry, penetration depth, coherence length, temperature, field, i.e. the flux distribution associated with a single vortex line, as well as the arrangement of the vortex lines in space and time. (Note: for a single 2D pancake vortex, the magnetic field has a component normal to the vortex axis [Clem 91], however, the average transverse component vanishes due to the large amount of contributions from the entire FLL. [Kogan 81]) $f(|\mathbf{B}|)$ is obtained from the time evolution of the muons' spins via a Cosine Fourier Transform (CFT) on $P(t)$. [Lee 93, 95, 97] It is known statistically that the variance (error bar) of $f(|\mathbf{B}|)$ does not change even with the total sampled points N going to infinity, which means the field distribution does not become more accurate as we take more sampled points from $P(t)$ (either by sampling a longer stretch of data at the same sampling rate, or by sampling the same stretch of data with a faster sampling rate although they will affect the frequency resolution).

Assume we have muon spin depolarization data $P(t_k)$ at time intervals $t_k = kT_s$ where T_s is the sampling period and $k = 0...M$. For the simplest case $P(t) = \cos(\omega_0 t)$, it can be proven that the discrete Fourier Transform of $P(t)$ has the following form

$$\begin{aligned} P(\omega) &= \sum_{k=0}^{M} \cos(\omega_0 k T_s)\cos(\omega k T_s) \\ &= \frac{1}{4}[1 + \frac{\sin\frac{(\omega_0-\omega)(2M+1)T_s}{2}}{\sin\frac{(\omega_0-\omega)T_s}{2}}] \end{aligned} \tag{1.16}$$

The factor $\sin\frac{(\omega_0-\omega)(2M+1)T_s}{2}$ in the numerator predicts fast oscillations in the field profile, which is certainly not what we wanted.

In reality, $P(t)$ has a typical time window of width 10 μs (square windowed), and the field profile should be obtained through the convolution of the data's Fourier transform with the window's Fourier transform. Since the square windowing causes large sidelobes in the Fourier transform (FT), usually we use other window functions such as the Gaussian window, Welch window, Hann window etc., which is called apodization, before we do the FT.

A standard treatment of FT on μSR data was introduced as following: (1) Divide the time spectrum by the contents of the first bin so that it only contains values between zero and one; (2) Subtract the mean from this spectrum; (3) Multiply the time spectrum with a window that we just introduced above; (4) Perform the Fourier Transform. [Martoff 81]

To simulate the vortex magnetic field distribution on the ab plane, we assume the extreme 2D case so that the relaxation of the muon's spin ensemble is determined mainly by the inhomogeneity of field on the ab plane. In some specific cases, we may need to consider the wavefunction and the fractal distribution of the muons. In the mixed state of HTSC due to various vortex lattice configurations and vortex-vortex interactions, we generated 20x20 grids and nearest neighbor grids in triangular lattice (for most superconductors) and square lattice (for V_3Si, $RNi_2Bi_2C(R = Er, Lu, Y)$, Sr_2RuO_4 etc.) respectively, and numerical simulations were carried out directly in the vortex lattice space to observe the field distribution $f(B)$. The ratio of the penetration depth λ_{ab} and the vortex lattice constant a is chosen according to the experimental value. The results are shown in fig. 1.5 and fig. 1.6. As we can see, $f(B)$ is more dependent on the particular form of single vortex $B(r)$

(we used three different kinds of $B(r)$ based on the current knowledge about the interaction from the literature [Clem 91, Schneider 95]). It was also found that the penetration depth λ affects the field distribution only weakly as long as λ is much greater than the lattice constant. Also notice the change of the difference between the peak position and the left shoulder in different lattice configurations and single vortex $B(r)$ forms. [Sonier 00A] For general calculation of the magnetic field distribution, see the monograph of Greer and Kossler [Greer 95].

Usually there is no difficulty to do so at low field. However, when the applied magnetic field is so high that the period of muon precession (7.38 ns in a field of 1 T) is comparable to the time resolution of the μSR spectrometer, we need to study the effect of time-shifted $P(t)$ (due to the instabilities of electronics, formation of short-lived Mu atoms or other fast chemistry effects [Brewer 94]) on the interpretation of $f(|\mathbf{B}|)$. Assume $P(t) = G_T(t)\cos(\omega_0 t)$ where $G_T(t)$ is the non-oscillating depolarization function and it can be exponential, stretched exponential, Gaussian or other types. Using the notations

$$P_{\cos}(\omega) = \int G_T(t)\cos(\omega t)\, dt \tag{1.17}$$

$$P_{\sin}(\omega) = \int G_T(t)\sin(\omega t)\, dt \tag{1.18}$$

We can easily derive the FT of the time-shifted $P(t)$ as follows:

$$\begin{aligned} P_{shift\_\cos}(\omega) &= \int G_T(t+\delta t)\cos[\omega_0(t+\delta t)]\cos(\omega t)\, dt \\ &= \frac{\cos(\omega_0\delta t)}{2}P_{\cos}(\omega_0-\omega) - \frac{\sin(\omega_0\delta t)}{2}P_{\sin}(\omega_0-\omega) \end{aligned} \tag{1.19}$$

$$P_{shift\_\sin}(\omega) = -\frac{\sin(\omega_0\delta t)}{2}P_{\cos}(\omega_0-\omega) - \frac{\cos(\omega_0\delta t)}{2}P_{\sin}(\omega_0-\omega) \tag{1.20}$$

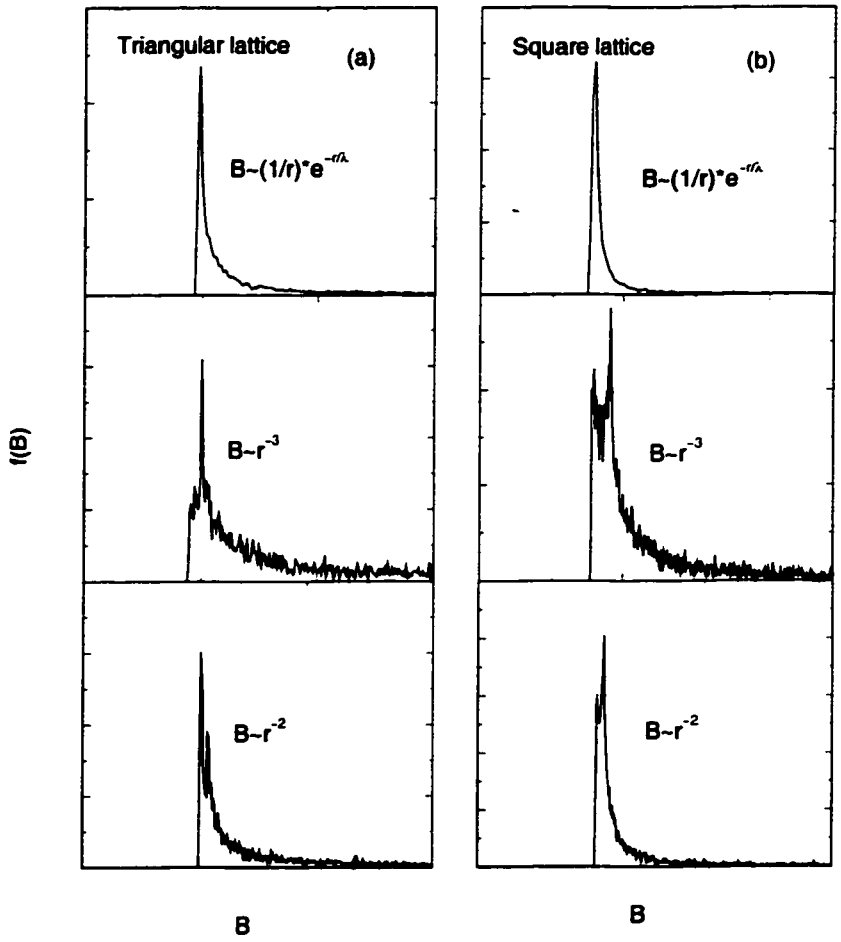

Figure 1.5: Simulated magnetic field distribution inside the vortex of HTSC. Left panel: triangular lattice configuration; right panel: square lattice configuration. The field distribution by the nearest neighbor approximation is still highly related to the 20x20 grid result.

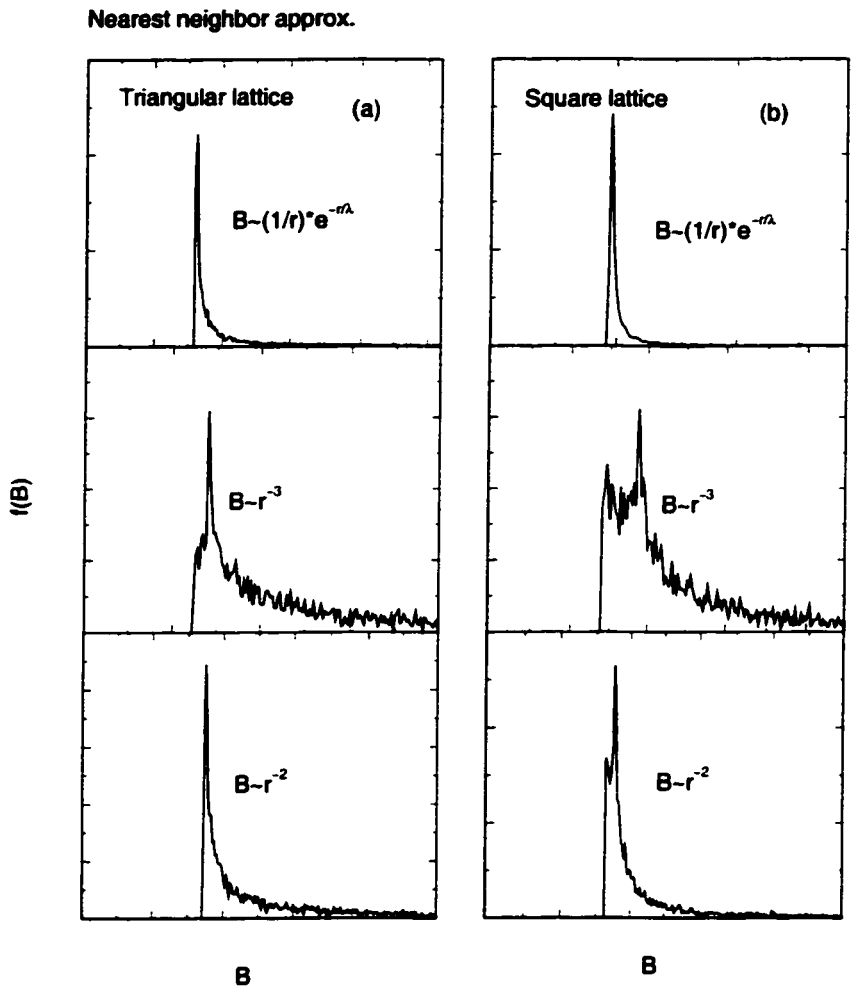

Figure 1.6: Simulated magnetic field distribution inside the vortex of HTSC. Left panel: triangular lattice configuration; right panel: square lattice configuration. The field distribution by the nearest neighbor approximation is still highly related to the 20x20 grid result.

Note in the expression of $P_{shift\_cos}(\omega)$, the 1st term is symmetric about ω_0, however, there is a sign change of the 2nd term when ω goes across ω_0. Just to see this behavior, we let $G_T(t) = e^{-\lambda t}$and use integral table results

$$\int_0^\infty e^{-\lambda t}\cos(\omega t)dt = \frac{\lambda}{\lambda^2+\omega^2} \tag{1.21}$$

$$\int_0^\infty e^{-\lambda t}\sin(\omega t)dt = \frac{\omega}{\lambda^2+\omega^2} \tag{1.22}$$

then

$$P_{shift\_cos}(\omega) = \frac{\cos(\omega_0\delta t)}{2}\frac{\lambda}{\lambda^2+(\omega-\omega_0)^2} - \frac{\sin(\omega_0\delta t)}{2}\frac{\omega-\omega_0}{\lambda^2+(\omega-\omega_0)^2} \tag{1.23}$$

A series of line shapes $P_{shift\_cos}(\omega)$ as a function of $\omega_0\delta t$ is shown in the fig. 1.7. To construct the real field profile $P_{\cos}(\omega_0-\omega)$ from the experimental data $P_{shift\_cos}(\omega)$ and $P_{shift\_sin}(\omega)$, we can do the following transformation

$$P_{shift\_cos}(\omega)\cos(\omega_0\delta t) - P_{shift\_sin}(\omega)\sin(\omega_0\delta t) = \frac{1}{2}P_{\cos}(\omega_0-\omega) \tag{1.24}$$

In the μSR technique, we can obtain the field profiles either from asymmetry plots or from individual histograms. During the data analysis, we often find that the phase factor in the depolarization function changes with temperature for unknown reasons (it may be due to the instability of the electronics). To evaluate the effects of this phase shift ϕ on the second moment and skewness calculations of the field profile, we generate a depolarization function (asymmetry plot) $P(t) = e^{-\frac{\sigma^2t^2}{2}}\cos(\omega t+\phi)$ where $\sigma = 2\ \mu s^{-1}$, $\omega = 20\ Mrad/s$. These parameters are chosen so that there are no evident changes in the field profiles when the phase shift ϕ varies from 0 to 0.5 ($\sim 30^0$). The ϕ dependent second moment (ideally the second moment should be 2 μs^{-1}) and the skewness plots are shown in the fig. 1.9.

We can clearly see that the second moment and skewness are very sensitive to the phase shift ϕ. This result requests us to extract the phase parameter accurately after fitting the μSR asymmetry plot.

To correct this phase-shift effect, we have modified the FT routine to obtain the correct field profiles as introduced in the following procedure, which is also appropriate when we analyze the individual histogram. We will now introduce another origin of the phase shift. We know that the asymmetry $A(t)$ is usually composed of two histograms coming from two oppositely (π out of phase) located detectors. However in reality, especially for high precession frequency data, the two histograms are usually found not exactly π out of phase. To consider this phase deviation ϕ from π, we can do the following analytical analysis. As usual, we assume the phase-shifted histograms are (we assume Gaussian depolarization here, we can also use other depolarization functions instead)

$$N_U(t) = N_0 e^{-\frac{t}{\tau}}[1 + A_0 e^{-\frac{\sigma^2 t^2}{2}} \cos(\omega t)] \tag{1.25}$$

$$N_D(t) = N_0 e^{-\frac{t}{\tau}}[1 - A_0 e^{-\frac{\sigma^2 t^2}{2}} \cos(\omega t + \phi)] \tag{1.26}$$

The asymmetry $A(t)$ can be expressed as

$$\begin{aligned} A(t) &= \frac{N_U - N_D}{N_U + N_D} \\ &= \frac{A_0 e^{-\frac{\sigma^2 t^2}{2}} \cos(\omega t) + A_0 e^{-\frac{\sigma^2 t^2}{2}} \cos(\omega t + \phi)}{2 + A_0 e^{-\frac{\sigma^2 t^2}{2}} \cos(\omega t) - A_0 e^{-\frac{\sigma^2 t^2}{2}} \cos(\omega t + \phi)} \\ &= \frac{A_0 e^{-\frac{\sigma^2 t^2}{2}} \cos(\omega t + \frac{\phi}{2}) \cos(\frac{\phi}{2})}{1 + A_0 e^{-\frac{\sigma^2 t^2}{2}} \sin(\omega t + \frac{\phi}{2}) \sin(\frac{\phi}{2})} \\ &\simeq A_0 e^{-\frac{\sigma^2 t^2}{2}} \cos(\omega t + \frac{\phi}{2}) \cos(\frac{\phi}{2}) - \frac{A_0^2}{4} e^{-\sigma^2 t^2} \sin(2\omega t + \phi) \sin\phi \end{aligned} \tag{1.27}$$

From the result above, we can see that, to the first order, the relaxation function is com-

posed of two depolarized harmonics with frequencies ω and 2ω. The asymmetry amplitude for the ω harmonic is $A_0 \cos(\frac{\phi}{2})$, which is reduced by a factor of $\cos(\frac{\phi}{2})$ from the original amplitude A_0, there is a phase shift $\frac{\phi}{2}$, which causes the changes on the second moment and skewness of the field profile as we have discussed before. Since A_0 is usually less than 0.4, the asymmetry amplitude for the 2ω harmonic $\frac{A_0^2}{4} \sin\phi$ is much less than $A_0 \cos(\frac{\phi}{2})$, which is that of the ω harmonic. All these conclusions have been verified through computer simulation.

When the external applied magnetic field is high, besides the phase-shift effect studied above, there are some other features we need to pay attention to such as: the radius of decay positron orbits shrinks with increasing field which requires small detectors within several centimeters of the sample; usually the time spectrum (histogram) consists of a large number of small time bins which have a rather low number of counts with correspondingly large statistical uncertainties. This circumstance makes the usual lab frame asymmetry plot rather uninformative to the eye and is appropriate to be studied in the frequency space. [Brewer 94]

1.4 The Rotating Reference Frame

In applied high magnetic field, the precession frequency of the muon spin is very high. If we would still prefer to study the asymmetry in the time domain rather than in the frequency domain, we could use the *rotating reference frame* scheme. To do this, we multiply the muon spin polarization function *P(t)* by function $cos(\omega_{RRF}t)$. The rotating-reference-frame frequency ω_{RRF} is chosen so that $\omega_\mu - \omega_{RRF}$ is small enough (usually between 3 and 15 MHz)

to produce a reasonable number of oscillations over the analyzed time interval (ω_μ is the muon spin precession frequency in the laboratory frame). Note that after *P(t)* is multiplied by function $cos(\omega_{RRF}t)$, two frequencies $\omega_\mu - \omega_{RRF}$ and $\omega_\mu + \omega_{RRF}$ will appear in the resulting function. We either filter out the higher frequency through a Fourier Transform or combine several time bin counts to get the lower frequency signal. There are two primary benefits of performing such a transformation. The first is that the quality of the fit can be easily and visually examined. It also allows the data to be packed into fewer bins, which greatly enhances the fitting speed.

The figure 1.10 shows a typical muon spin precession signal in the vortex state of Bi2212 for magnetic fields of 3.0 T and 6.0 T applied parallel to the *c*-axis in our experiment. The signals are displayed in a reference frame rotating at about 10 MHz below the Lamor precession frequency of the muon. Dephasing of the signal arises from an inhomogeneous distribution of magnetic fields associated with the vortex lattice.

1.4.1 Heterodyne Technique

The Heterodyne Technique is an improved variation on the *rotating reference frame* (RRF) technique in which the data from all the detectors are also used. For a given spectrum, the asymmetry is first obtained (subtract background, multiply by $e^{+\frac{t}{\tau}}$, subtract the average value), then a heterodyned asymmetry is produced by multiplying the asymmetries just obtained by $cos(\omega_h t)$, where ω_h is an angular rate near to and usually below the Lamor frequency. Final asymmetry is obtained by summing over a number of channels to get rid of the higher frequency component generated after the multiplication. For fitting purposes, the predicted asymmetry is treated identically to the data. The advantage of this technique

is that the phases in the cosine term of the asymmetry function need not be fixed. In this way, we can make full use of all the experimental data, which is important at high magnetic fields.

1.5 The Purpose of This Research

In this research work, we chose Bi2212 as sample because it is the most anisotropic 2D superconductor discovered so far. We expect that the vortex pancake plays important role on the magnetic field distribution inside the superconductor and we aim to obtain important information on the vortex pancake configuration in the mixed state of Bi2212. High transverse field muon spin rotation and relaxation technique was used to study the sample because in this field range (1.0-7.0 T), very few research was carried out due to the high requirements of electronic resolution, statistics and difficulty during the data analysis process.

In the next chapter, we will review some general properties of magnetic field distribution inside superconductor, then we will present our experimental data and compare them with the results from a proposed pancake vortex disorder model.

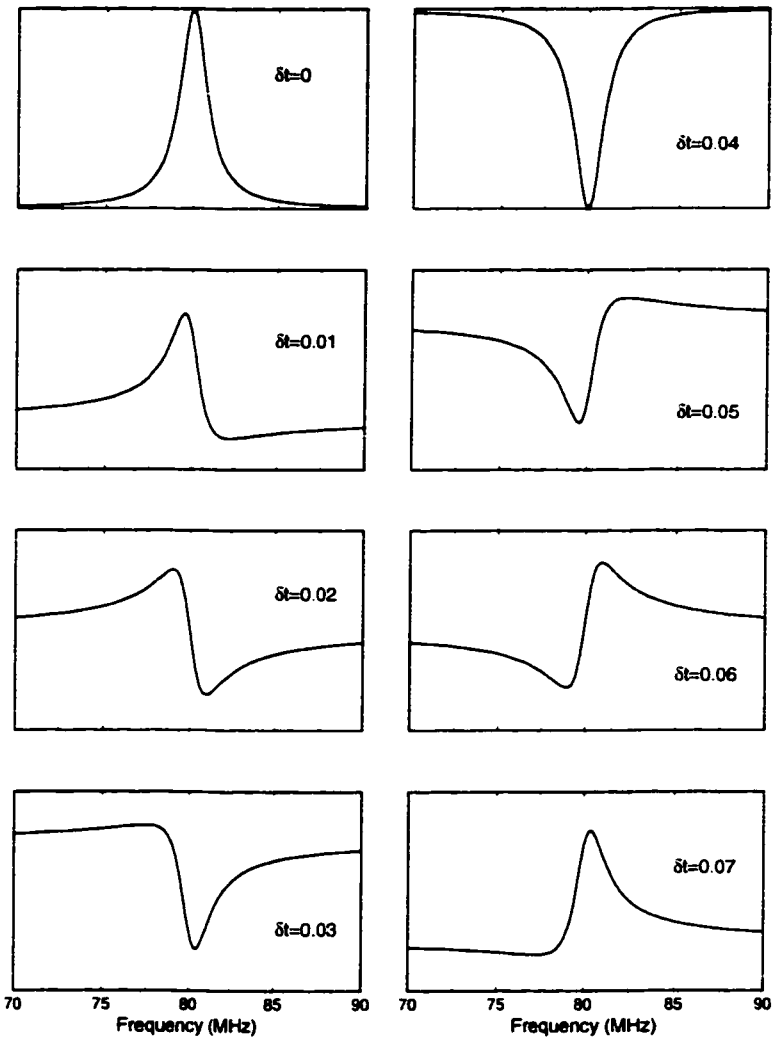

Figure 1.7: Simulated field profiles as functions of the time shift δt (unit:μs) where $\omega_0 = 80$ MHz and $\lambda = 1\mu s^{-1}$.

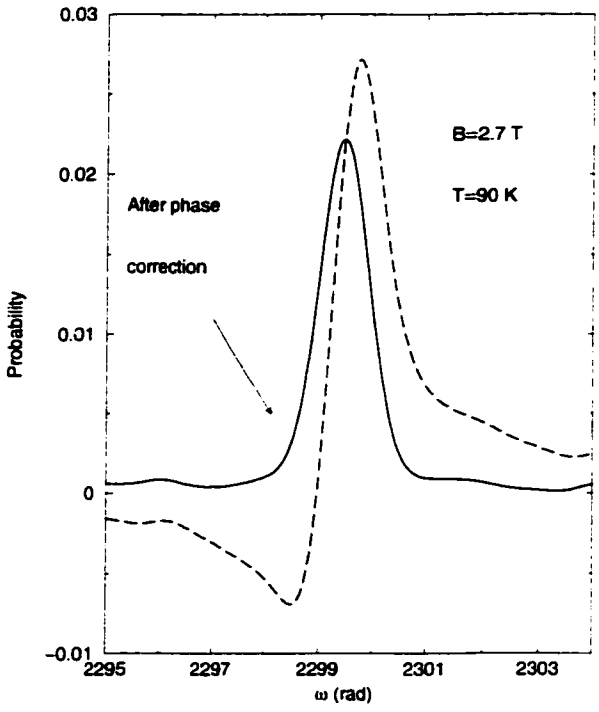

Figure 1.8: The long dashed line is the result of a direct FT on the μSR spectrum ($B = 2.7T$ and $T = 90K$) without phase correction; after correction, it shows the actual field profile (solid line).

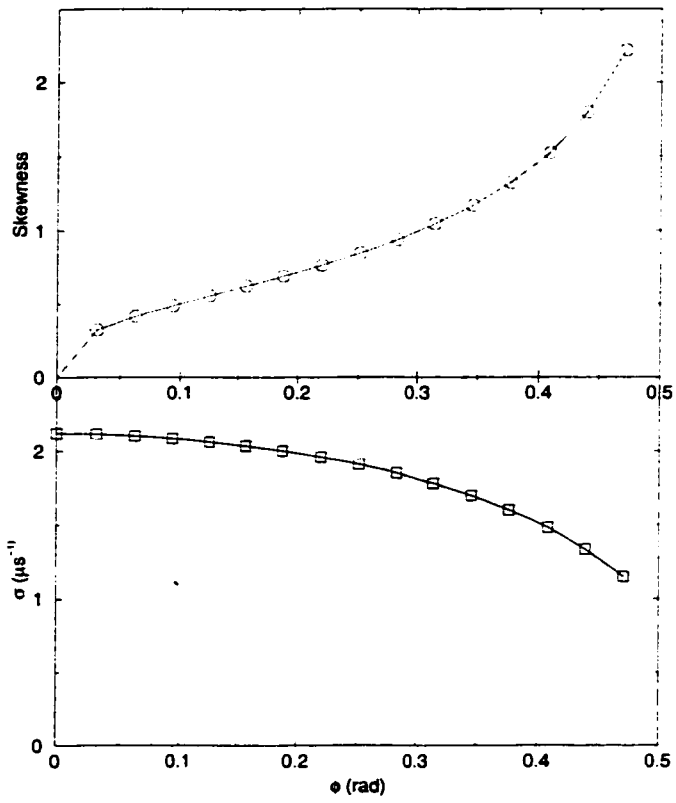

Figure 1.9: The effects of phase shift on the skewness and the second moment of the field profile. The simulation procedure is described in the text.

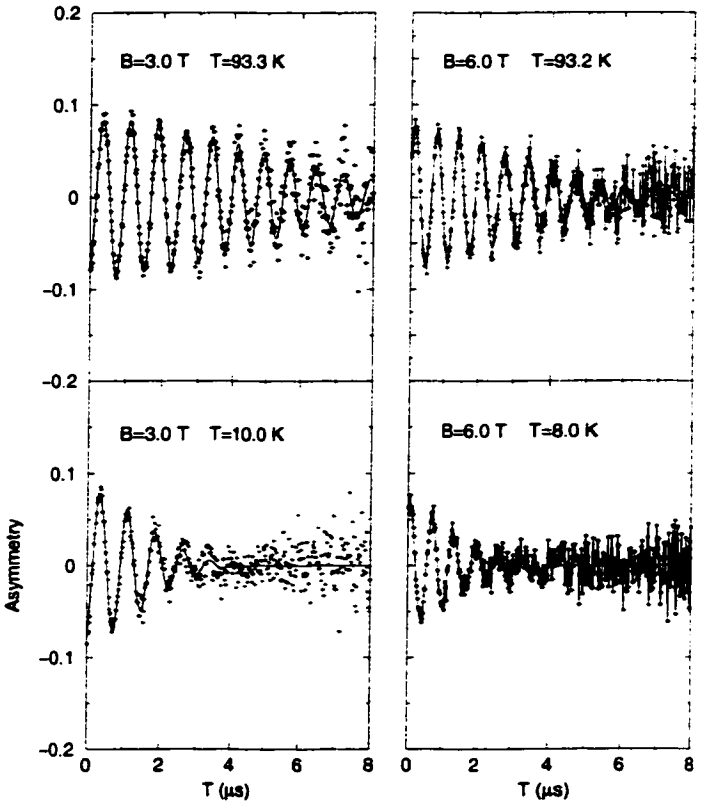

Figure 1.10: The muon spin precession heterodyned asymmetry signals in Bi2212, displayed in a rotating-reference-frame frequency of 10 MHz.

Chapter 2

Magnetic Field Distribution

2.1 Local Magnetic Fields

We know that by determining the Larmor frequency from a transverse field μSR histogram, it is possible to determine the local magnetic field $\mathbf{B}_\mu$. Generally the total magnetic field at the muon site $\mathbf{B}_\mu$ can be expressed as follows: [Schenck 85]

$$\mathbf{B}_\mu = \mathbf{B}_{ext} - \mathbf{B}_{DM} + \mathbf{B}_L + \mathbf{B}_c + \mathbf{B}_{dip} \tag{2.1}$$

where $\mathbf{B}_{ext}$ is the externally applied field (if any) generated by either Helmholtz coils, electromagnets or superconducting coils, $\mathbf{B}_{DM}$ is the demagnetization field due to the finite and particular shape of the sample, $\mathbf{B}_L$ is the Lorentz field produced by magnetic polarizations induced on the interior of a hypothetical spherical cavity around the muon site due to the average bulk magnetization of the medium, $\mathbf{B}_c$ is contact hyperfine field exerted on the muon by its Fermi contact interactions with the net spin density of conduction electrons, and $\mathbf{B}_{dip}$ is the net field from the surrounding microscopic magnetic dipoles within the Lorentz cavity appropriately thermally averaged over magnetically inequivalent sites. Interpretation of these fields requires knowledge of the muon site, including zero-point motion

and any tunneling between nearby sites, and sometimes can be quite difficult. See [Kossler 85, Schenck 85, Brewer 94] for further discussions on this topic. Note that in the theoretical scheme of calculating the field profile, due to the existence of finite field interval Δ, the calculated value $f_c(B)$ deviates from the true value $f_t(B)$ by $\frac{\Delta}{2} f_t'(B)$ i.e. [Wan 99]

$$f_c(B) = f_t(B) + \frac{\Delta}{2} f_t'(B) \tag{2.2}$$

2.2 Lower and Upper Critical Fields B_{c1} and B_{c2}

The underlying physics of the high temperature superconductors (HTSC) has been revealed in part by their internal magnetic fields both in the normal and superconducting states. For a type II superconductor, the Ginsburg-Landau (GL) parameter $\kappa = \frac{\lambda}{\xi_{GL}} \gg \frac{1}{\sqrt{2}}$, and the lower critical field B_{c1} can be expressed as [Abrikosov 57]:

$$B_{c1} = \frac{1}{2\kappa}(\ln \kappa + 0.08)\ B_{cth} \tag{2.3}$$

$$\approx \frac{\ln \kappa}{\sqrt{2}\kappa}\ B_{cth} \text{ (in some literature)} \tag{2.4}$$

where B_{cth} is defined in terms of the differences of the free enthalpies between the normal and superconducting states: [Buckel 91]

$$G_n - G_s = \frac{B_{cth}^2}{2\mu_0} V \tag{2.5}$$

Similarly, with the aid of the GL parameter, the upper critical field B_{c2} is given by the relationship:

$$B_{c2} = \sqrt{2}\ \kappa\ B_{cth} \tag{2.6}$$

In the equations above, we have expressed B_{c1} and B_{c2} in terms of the GL parameter κ and B_{cth}. Sometimes we can also estimate them in terms of λ and ξ as

$$B_{c1} \approx \frac{\phi_0 \ln \kappa}{4\pi\lambda^2} \tag{2.7}$$

$$B_{c2} \approx \frac{\phi_0}{2\pi\xi^2} \tag{2.8}$$

In the equations above, B_{c1}, B_{c2} and B_{cth} are all temperature dependent. We can see that, for type II superconductors, as κ increases, B_{c1} becomes smaller and B_{c2} larger. Recently, in the cuprate superconductors, high magnetic field studies (up to 60 T) have revealed a non-BCS divergent shape of the upper critical field. [Zavaritsky 00]

For anisotropic superconductors, the critical fields (B_{c1} or B_{c2}) perpendicular to the plane of the CuO_2 layers $B_{c1\perp}$ or $B_{c2\perp}$ may be different from those parallel components $B_{c1||}$or $B_{c2||}$. For example, for single crystal $YBa_2Cu_3O_7$, $B_{c2\perp}$ $(T = 0\ K) \simeq 52.5\ T$, $B_{c2||}$ $(T = 0\ K) \simeq 230\ T$ and $B_{c1\perp}$ $(T = 11\ K) \simeq 0.069\ T$, $B_{c1||}$ $(T = 11\ K) \simeq 0.012\ T$ [Umezawa 88, Worthington 88, Bourdillon 94]. For theories on the calculation of the upper critical field, see ref. [Kogan 81, Werthamer 66]. Generally, the upper critical fields depend on both the crystal orientation θ (the angle between c-axis and magnetic field) and temperature T, and can be expressed as the following phenomenological formula which best fits the experimental data:

$$B_{c2}(T,\theta) = B_0(\theta) \left(\frac{T_c - T}{T_c}\right)^{2\gamma(\theta)} (\sin^2\theta + \frac{m_\perp^2}{m_{||}^2}\cos^2\theta)^{-\frac{1}{2}} \tag{2.9}$$

In high T_c cuprates such as Bi2212, B_{c2} is considered to be a crossover field between the normal state and a vortex liquid mixed state [Fisher 91] and SQUID magnetization measurements show that this transition is not sharp. Below B_{c2} there is another characteristic field

B_{2D} across which a transition (melting) happens from a 3D vortex mixed state (Abrikosov lattice) to a 2D vortex liquid mixed state. B_{2D} is estimated to be around 1 T at $T = 30\ K$ [Kes 91]. In our μSR experiments on Bi2212, since the transverse fields are applied along the crystalline c-axis ($\theta = 0$), it is important to study the lower and upper critical fields along this direction so that we can determine whether the sample is in a mixed state before interpreting any data.

Evidently our applied magnetic fields are much greater than the lower critical field $B_{c1\perp}$; here we will only be concerned about the upper critical field in Bi2212. Some reports from the literature are listed as follows: $B_{c2\perp}(T = 0K) = 122T$ [Kogan 81] (this result is too optimistic and does not include the Pauli paramagnetic limiting effect, which will suppress $B_{c2\perp}$ substantially [Pint 89]); $B_{c2\perp}(T = 4.2K) = 20T$ [Guillot 89]; $B_{c2\perp}(T = 0K) = 32T$ [Datta 92]. Based on these experimental data on $B_{c2\perp}$, for external magnetic field $B = 7.0T$, the temperature at which the transition between the mixed and normal states happens is estimated conservatively around 70 K [Wan 99]. For even lower external field, the transition temperature will be even higher. Thus in the experimental field range, below 70 K, we can expect that the Bi2212 is in a mixed state.

2.3 The Penetration Depth λ, Coherence Length ξ and Core Radius ρ_0

When a small magnetic field $H < H_{c1}$ is applied to a type II superconductor, the field is expelled from the interior of the sample; while $H_{c1} < H < H_{c2}$, it becomes energetically favorable for the field to penetrate the sample in the form of quantized lines-vortices. In the

first case (Meissner state), the magnetic field only penetrates into the sample surface with a characteristic length scale λ, which is called the magnetic penetration depth. In the second case (vortex state), the local magnetic field has a maximum in the center of the vortex core and decays outside the core over the length scale λ in the vortex.

The magnetic field penetration depth λ is one of the fundamental scales of a superconductor and is given by the London formula

$$\frac{1}{\lambda^2} = \frac{\mu_0 e^2 n_s}{m^*} \times \frac{1}{1+\xi/l} \tag{2.10}$$

where μ_0 is the vacuum permeability, e is the electron charge, m^* is the effective mass (in general a tensor) of the superconducting carriers and n_s is the superconducting carrier density. The correction factor is related to the coherence length ξ and the mean free path l. In the clean limit ($\xi \ll l$), the correction factor essentially becomes unity. This is indeed the case for high T_c cuprates, organic(BEDT), the HF superconductor UPt_3, and the Chevrel-phase systems. Furthermore, if we assume the effective mass m^* remains constant, the temperature dependence $\lambda(T)$ reflects the quasiparticle density of states due to thermal excitations and therefore probes the nature of the low energy excitations, the superconducting gap structure and the symmetry of the pairing state. Among the various techniques (ac susceptibility, microwave cavity measurement, mutual inductance, far infrared reflectivity, electron holography, inverted microstrip resonator technique etc.) to investigate the vortex lattice, small angle neutron scattering (SANS) and muon spin relaxation (μSR) experiments are unique since they directly probe the bulk of the material. In the non-cubic superconductors, and especially high temperature superconducting materials, penetration depth may be anisotropic and dependent on crystallographic orientations with respect to both magnetic

field and specimen surface. In muon spin relaxation measurements in a wide class of high temperature superconductors, Uemura *et al.* reported a universal linear relation (Uemura Plot) between T_c and n_s/m^* at low carrier doping levels, whereas in heavily doped samples saturation or a slight decrease was observed. [Uemura 89, 91]

The temperature dependence of the penetration depth based on an interpretation of the London electrodynamics of a superconductor (Gorter-Casimir model) is given by [Schrieffer 88]

$$\lambda(T) = \lambda(0)\frac{1}{\sqrt{1-(T/T_c)^4}} \tag{2.11}$$

$\lambda(0)$ is the penetration depth at $T = 0\ K$ and is simply c/ω_p for good bulk superconductors where ω_p is the normal state plasma frequency. A good fit of experimental data to the equation above is usually taken to mean that the pairing in high T_c superconductors is of the conventional s-wave type with no nodal points or lines in the energy gap function. In practice, sometimes the power index 4 in the equation above is generalized as a phenomenological parameter n.

The general *energy gap* model based on the exponential specific heat law gives the expression [Lewis 56]

$$\lambda(T) = \frac{\lambda(0)}{\sqrt{1-\frac{(2\alpha+t)E(\alpha/t)-2te^{-\alpha/t}}{E(\alpha)(1+2\alpha)-2e^{-\alpha}}}} \tag{2.12}$$

where α is a parameter related to specific heat, t is reduced temperature T/T_c, and $E(x)$ is the exponential integral function defined by $E(x) = \int_x^\infty \frac{e^{-\tau}}{\tau}d\tau$. If we assume $\sigma(T) \propto 1/\lambda^2(T)$, we can test the model from the experimental relaxation data. In practice, the comparison may be obscured by extrinsic effects such as T-dependence pinning strength, FLL thermal motion, different defect structures for samples of similar composition, i.e.

heuristic factors affecting the topology of the FLL especially for the bismuth-based family [Ansaldo 91].

A major question in high T_c superconductivity is whether or not there are nodes in the superconducting gap function (pairing state). In fact, recent experimental and theoretical work on the symmetry of the order parameter in HTSC has led to the conclusion that for the majority of the cuprate superconductors the symmetry of the order parameter is dominated by a $d_{x^2-y^2}$-wave component (the gap function has the form $\Delta(k) = \Delta_0[cos(k_x a) - cos(k_y b)]$. [Harlingen 95, Scalapino 95] This is in contrast to the metallic low-temperature superconductors for which the order parameter is dominated by an isotropic s-wave component. The problem of an isolated vortex line in a $d_{x^2-y^2}$-wave superconductor was first seriously considered by Soininen *et al.* using a simple microscopic model for electrons on a lattice in the Bogoliubov-de Gennes formalism. [Soininen 94] They found an s-wave component is induced near the vortex core with opposite winding of phase relative to the $d_{x^2-y^2}$-wave component. Thus in the core region of an isolated vortex, the magnetic field distribution is fourfold symmetric, whereas outside the core region, the field distribution is circular symmetric. In 1996, Xu *et al.* extended the two-component Ginzburg-Landau theory for an orthorhombic crystal structure [Xu 96A], they concluded that for a field applied parallel to the c axis, both s-wave and $d_{x^2-y^2}$-wave order parameters exhibit two-fold symmetry when the anisotropy γ is greater than 1. Based on numerous studies on this topic, we now think the actual order parameter present in hole doped HTSC likely is formed by a mixture of a dominating $d_{x^2-y^2}$-component and other components such as an s- or d_{xy}-component. [Alff 98] Recently, Krishana *et al* discovered an anomalous plateau in the longitudinal thermal conductivity of Bi2212 at high magnetic fields which they attributed to the opening of a

second gap of d_{xy} symmetry. [Krishana 97] There have been numerous experiments devoted to the study of the symmetry of the order parameter in the oxide superconductors, which are divided into two categories: based on probing the quasiparticle excitation spectrum and probing the phase of the order parameter in interferometer experiments. [Alff 98] Extracting the symmetry of the order parameter from the temperature dependence of the magnetic penetration depth belongs to the first category.

In order to establish rigorous constraints on the pairing state from the temperature dependence of the electromagnetic penetration depth, it is necessary to determine the asymptotic behavior at low temperature. [Annett 91] For any pairing state with a finite excitation energy, the change in λ at low temperature is ($\Delta\lambda(T) = \lambda(T) - \lambda(0)$)

$$\Delta\lambda(T) \propto e^{-\frac{\Delta}{k_B T}} \tag{2.13}$$

and Δ in the exponent is the minimum value of the energy gap over the Fermi surface. For pairing states with nodes on the Fermi surface

$$\Delta\lambda(T) \propto T^p \tag{2.14}$$

where $p = 1$ for the simplest form of the gap with d-wave symmetry. In general, powers of T, T^2, T^3, or T^4 are all possible depending on the types of nodes and the orientation of the applied field. [Gross 86, Annett 96] The limiting temperature dependence of $\lambda(T)$ as $T \rightarrow 0$ K decides whether the superconductivity is conventional or unconventional [Shrivastava 96]. Besides these theoretical considerations, there are many effects which may influence the detailed form of the temperature dependence, including strong-coupling corrections, dirt,

the precise shape of the Fermi surface etc.. [Annett 91] Also Roddick and Stroud [Roddick 95] have described a simple model to consider the fluctuation effects and obtained a linear temperature dependence in $\lambda(T)$. A variational calculation shows that this linear T-dependence persists even when quantum effects due to charging and dissipation are included in the model. Furthermore, in orthorhombic or tetragonal crystals, all singlet pairing states other than s-wave would lead to such a linear temperature dependence. [Sigrist 87] Thus a linear temperature dependence $\lambda(T)$ may not be sufficient to be the signature of a superconductor with the nodes at the Fermi surface.

At the same time, detailed μSR investigations of HTSC have demonstrated that λ can be obtained from the muon spin depolarization rate $\sigma(T) \sim 1/\lambda^2(T)$ [Keller 94, Pümpin 90]. For an isotropic extreme type-II superconductor with a perfect triangular vortex lattice, the depolarization rate $\sigma(T)$ is directly related to the penetration depth via [Brandt 88A]

$$\sigma(T) \sim \sqrt{\langle \Delta B^2 \rangle} = 0.0609 \frac{\Phi_0}{\lambda^2(T)} \tag{2.15}$$

where Φ_0 is the magnetic flux quantum. This equation is only valid for high magnetic fields ($B_{ext} > 2\mu_0 H_{c1}$) where the second moment $\langle \Delta B^2 \rangle$ is field independent [Brandt 88A] and the vortices are static without any thermal fluctuations and disordering [Harshman 91]. The distinctive increase in this depolarization rate parameter below T_c is common to all reported results for the oxide superconductors.

To accurately determine λ for a specific FLL involves detailed modeling of the field distribution. One such model relies on an approximate low-field solution of the Ginzburg-Landau theory [Clem 75], which has been extended to higher fields later on [Hao 91] and further simplified [Yaouanc 97].

Generally, the relaxation rate σ depends on both temperature T and magnetic field induction H. Based on phenomenological Ginzburg-Landau (GL) theory, for superconductors with GL parameter $\kappa = \lambda/\xi \gg 1$, we know [Yaouanc 97]

$$\begin{aligned}
\sigma^2(T,H) &= \int_{-\infty}^{+\infty} f(B)(B-B_0)^2 dB \\
&= \int_{-\infty}^{+\infty} \frac{1}{V}\int_V \delta(B-B(\mathbf{r}))d\mathbf{r}(B-B_0)^2 dB \\
&= \frac{1}{V}\int_V (B(\mathbf{r})-B_0)^2 dB \\
&= \frac{1}{V}\int_V (\sum_{\mathbf{G}} B(\mathbf{G})e^{i\mathbf{G}\cdot\mathbf{r}} - B_0)^2 dB \\
&= \sum_{\mathbf{G}} |B(\mathbf{G})|^2 - {B_0}^2 \\
&= \sum_{\mathbf{G}\neq 0} |B_z(\mathbf{G})|^2 \\
&\simeq \left(\frac{\Phi_0}{S}\right)^2 \sum_{\mathbf{G}\neq 0} \left|\frac{R(\xi\,|\mathbf{G}|)}{1+\lambda^2(T,H)G^2}\right|^2
\end{aligned} \tag{2.16}$$

where $R(\xi\,|\mathbf{G}|)$ is the vortex core cut-off function. Usually, the penetration depth $\lambda(T,H)$ is much greater than the vortex lattice constant i.e. $\lambda^2(T,H)G^2 \gg 1$, so the equation above can be further simplified as

$$\begin{aligned}
\sigma^2(T,H) &\simeq \frac{1}{\lambda^4(T,H)}\left(\frac{\Phi_0}{S}\right)^2 \sum_{\mathbf{G}\neq 0}\left|\frac{R(\xi\,|\mathbf{G}|)}{G^2}\right|^2 \\
&= \frac{1}{\lambda^4(T,H)}\left(\frac{\Phi_0}{S}\right)^2 f_s(\xi,\mathbf{G})
\end{aligned} \tag{2.17}$$

where $f_s(\xi,\mathbf{G})$ is the vortex structure factor and also depends on field induction H through the implied dependence of $\mathbf{G}(H)$.

Further, the field dependence of the penetration depth λ can be the consequence of interesting non-linear and non-local effects. Franz, Affleck and Amin have developed a

means to calculate the field distributions assuming a regular vortex lattice and incorporating the non-local effects enhanced by the presence of the nodes and also including non-linear effects. [Franz 97] In the simplest case, assuming $\lambda(T,H)$ and $f_s(\xi,\mathbf{G})$ are H independent and $\lambda(T)=\lambda(0)\frac{1}{\sqrt{1-(T/T_c)^4}}$ [Gorter 34], $\sigma(T)\propto 1-(T/T_c)^4$.

A weak temperature dependence of σ for $T \ll T_c$ suggests there is an energy gap in the spectrum of excitations [Aeppli 87, Harshman 87, Pümpin 90], as expected for conventional s-wave pairing; a linear temperature dependence in σ suggests a pairing state with nodes in the gap [Scalapino 95], as found in $YBa_2Cu_3O_{6.95}$ [Hardy 93, Sonier 94] and $Bi_2Sr_2CaCu_2O_8$ [Jacobs 95, Lee 96]. However, it was shown [Roddick 95] that the phase fluctuations of the superconducting order parameter, as proposed by Emery and Kivelson [Emery 95], can also lead to such a linear T dependence. Further, predicting the behavior of λ and σ in the vortex state may need to include the nonlinear and nonlocal effects. [Amin 00] The behavior of the temperature dependence of the penetration depth will be explained further later in the Experiments, Results and Analysis section.

To explain numerous experimental results which deviated from the predictions of the London theory, Pippard proposed the concept of coherence length. [Pippard 53] The coherence length ξ is a measurement of the nonlocal response of the superconductor to the applied magnetic field in the sense that the value of the supercurrent **J** measured at a point **r** depends on the value of the vector potential **A** throughout a volume of radius ξ surrounding the point **r**.

The high T_c materials differ remarkably from conventional superconductors in that they have much smaller coherence lengths. Consequently, these materials are in the extreme type II and clean limit. Furthermore, fluctuation, boundary effects and anisotropy are all much

stronger in these short ξ superconductors. We now also know the coherence length ξ is the length scale for spatial variations in the superconducting order parameter or density of the superconducting carriers. Compared with the penetration length λ, there is less known about ξ. In fact there have been very few measurements of ξ deep in the superconducting state of a high-T_c superconductor. Estimates of ξ can be obtained from the contribution of fluctuations to measured quantities such as the specific heat, susceptibility or conductivity. Scanning tunneling microscopy (STM) can be used to measure the vortex- core radius at the sample surface, which provides an estimate of ξ. For a type-II superconductor for H near H_{c2}, the magnitude of ξ may be estimated from the measurements of the upper critical field H_{c2} using Ginzburg-Landau (GL) theory. At this field the vortices begin to overlap and the superconductor undergoes a first order phase transition into the normal state. Since the radius of a normal vortex core is about the size of the coherence length, then at H_{c2} there is a direct relationship with ξ. From GL theory,

$$\xi(T) = \sqrt{\frac{\Phi_0}{2\pi H_{c2}(T)}} \tag{2.18}$$

However, reliable measurements of ξ in this way are difficult due to the difficulties in the accurate measurement of $H_{c2}(T)$. In high T_c materials, H_{c2} is very large (several hundred Tesla) at $T = 0$ and is therefore difficult to measure accurately. Measurements are generally limited to temperatures near T_c where H_{c2} is considerably smaller. However, near T_c thermal fluctuations of the vortex lines can depin or melt the solid 3D vortex lattice into a vortex liquid phase. Furthermore, the equation above may not be valid for an unconventional superconductor. Thus it is desirable to have direct measurements of the coherence length, which in the vortex state is related to the size of the vortex cores, i.e. $\xi \sim \rho_0$, where ρ_0 is the

vortex core radius [Caroli 64]. The vortex core structure was studied intensively in the past. In principle both STM [Hartmann 93] and μSR [Sonier 97] can be used to characterize the vortex structure factor $f_s(\xi, \mathbf{G})$ or the size of vortex cores and thereby determine ξ. In a μSR experiment, ρ_0 is related to the high-field cutoff of the measured internal field distribution. It was found in $NbSe_2$ [Sonier 97] that ρ_0 decreases with increasing H, as a result of the increased interaction between vortices. In $YBa_2Cu_3O_{6.95}$, the temperature dependence of $\xi(T)$ was determined [Riseman 95] and no clear signal from the vortex cores was visible below 3 T [Sonier 94, 97A].

As described by Uemura [Uemura 91], the effective Fermi temperature T_F in superconductors can be derived from a combination of the Fermi velocity $v_F \propto n_s^{1/3}/m^*$ and the relaxation rate $\sigma \propto n_s/m^*$, following the relationship for a non-interacting electron gas:

$$k_B T_F \propto \sigma^{1/2} v_F^{1/2} \tag{2.19}$$

The Fermi velocity was estimated using the proportionality to the coherence length $\xi = \hbar v_F/(\Delta\pi)$. The energy gap Δ is calculated from a formula for s-wave superconductors in the clean limit: $\Delta = 1.76 k_B T_c$.

2.4 Skewness Factor α

The measurement of the magnetic field distribution in the vortex of type II HTSC via μSR allows an investigation of the details of the flux structure [Lee 93], such as the effects of random pinning [Brandt 88] and the dimensionality of the vortex structure [Brandt 91]. To quantify the shape of the field distribution, a skewness factor α, the variation of which

reflects the underlying changes in the vortex structure [Lee 93, 95, 97, Aegerter 98], is defined from the 3rd and 2nd moments of the field line shape. The parameter α is very sensitive to structural changes of the vortex state which occurs as a function of temperature and magnetic field. A value of $\alpha \sim 1.2$ is typical for a static triangular FLL, whereas $1 > \alpha > 0$ either indicates a disordered static vortex structure or vortex dynamics in excess of the typical μSR time scale (μs). [Blasius 00] Notice that in real data analysis, this skewness may be an artifact by the fast depolarization and apodization of the time-shifted μSR spectra [Wan 99].

$$\alpha = \frac{\langle (B-\overline{B})^3 \rangle^{\frac{1}{3}}}{\langle (B-\overline{B})^2 \rangle^{\frac{1}{2}}} \tag{2.20}$$

$$= \frac{(M_3 - 3M_1M_2 + 2M_1^3)^{\frac{1}{3}}}{(M_2 - M_1^2)^{\frac{1}{2}}} \tag{2.21}$$

where $M_n = \int B^n f(B) dB$.

Table 2.1 Theoretical skewnesses for several commonly seen field profiles.

$f(B)$	$\alpha(x)$
Back-to-back Exponential $f_E(B)$	$\alpha_E(x) = \frac{[2(x-1)(x^2+x+1)]^{\frac{1}{3}}}{(1+x^2)^{\frac{1}{2}}}$, where $x = \frac{\lambda_L}{\lambda_R}$
Back-to-back Gaussian $f_G(B)$	$\alpha_G(x) = \frac{[\sqrt{\frac{2}{\pi}}(x-1)(3x-x^2-1)+\frac{4}{\pi}\sqrt{\frac{2}{\pi}}(x-1)^3]^{\frac{1}{3}}}{[(1-\frac{2}{\pi})(1-x)^2+x]^{\frac{1}{2}}}$, where $x = \frac{\sigma_R}{\sigma_L}$
Back-to-back Line $f_L(B)$	$\alpha_L(x) = \frac{[(x-1)(\frac{x^2}{135}+\frac{x}{54}+\frac{1}{135})]^{\frac{1}{3}}}{[\frac{1}{18}(1+x+x^2)]^{\frac{1}{2}}}$, where $x = -\frac{k_L}{k_R}$

The definitions for *Back-to-back Exponential* $f_E(B)$, *Back-to-back Gaussian* $f_G(B)$ and *Back-to-back Line* $f_L(B)$ functions are as follows: (the skewness doesn't depend on the

normalization factor which we have chosen as 1)

$$f_E(B) = \begin{cases} e^{-\lambda_L(B_0-B)}, & \text{for } B < B_0 \\ e^{-\lambda_R(B-B_0)}, & \text{for } B \geq B_0 \end{cases} \tag{2.22}$$

$$f_G(B) = \begin{cases} e^{-\frac{(B-B_0)^2}{2\sigma_L^2}}, & \text{for } B < B_0 \\ e^{-\frac{(B-B_0)^2}{2\sigma_R^2}}, & \text{for } B \geq B_0 \end{cases} \tag{2.23}$$

$$f_L(B) = \begin{cases} k_L(B-B_0)+1, & \text{for } B < B_0 \\ k_R(B-B_0)+1, & \text{for } B \geq B_0 \end{cases} \tag{2.24}$$

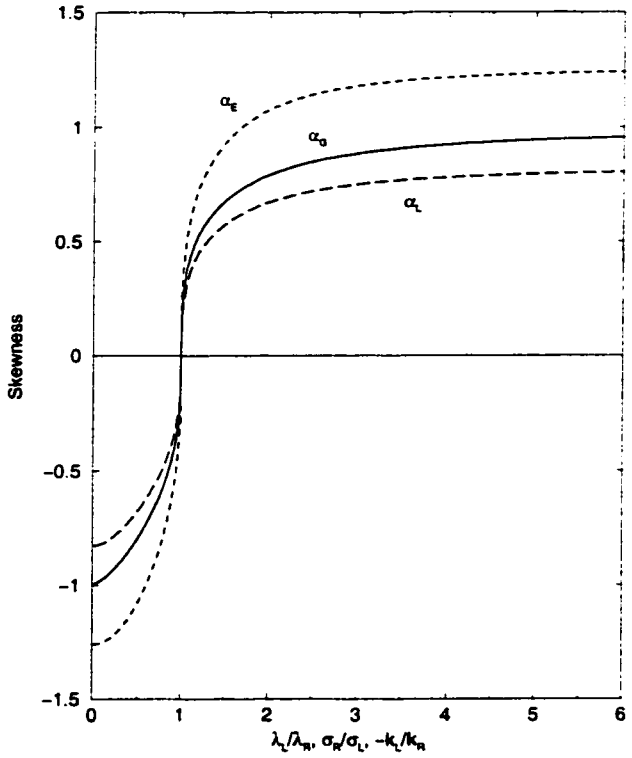

Figure 2.1: Theoretical skewness plots for α_E, α_G and α_L.

Chapter 3

BSCCO Family and Bi2212 System

3.1 Introduction to type-II superconductors

When the external magnetic field applied on a superconductor is between the lower critical field H_{c1} and the upper critical field H_{c2} for that specific superconductor, we say that the superconductor is in a vortex state in which quantized flux lines or flux pancakes are formed inside the superconductor. Numerous theoretical and experimental studies have revealed new information that is essential to better understand the microscopic mechanism of type-II superconductor. However, there is still no comprehensive theory of the high temperature superconductors (HTSC). The symmetry of the order parameter is still being debated, the mechanism and its relation to magnetic order is unknown, and there continue to be surprises in the properties of flux vortices.

3.2 Introduction to BSCCO

We will only concentrate on the BSCCO family and Bi2212 superconducting systems here. For a historical review of superconductivity from mercury to the ceramic oxides, see ref. [Dahl 92]. In 1987, the ability of bismuth to form lamellar oxides was recognized, the

single-layer Bi-Sr-Cu-O compound was discovered to have critical superconducting temperature ranging from 9 to 22 K [Michel 87]. Superconducting bismuth cuprates were later reported to form a family of layer-structure phases with ideal formulas $Bi_2Sr_2Ca_{n-1}Cu_n O_{4+2n}$ (BSCCO) with n=1 (Bi2201, $T_c(B=0) = 10K$), 2 (Bi2212, $T_c(B=0) = 80K$), and 3 (Bi2223, $T_c(B=0) = 110K$), depending on the number of $(CuO_2)_n$ layers. (Note the critical temperature T_c is magnetic field and doping dependent.) $Bi_2Sr_2Ca_{n-1}Cu_nO_{4+2n}$ (BSCCO) is even another subset of the $A_2B_2Ca_{n-1}Cu_nO_{4+2n}$ family where A=Bi or Tl, B=Sr or Ba. The BSCCO system (Bi2223) was found to show promising superconducting and other properties that are appropriate for wire and tape applications using the powder-in-tube (PIT) techniques [Zhou 95]. In $Bi_2Sr_2CaCu_2O_8$ (BSCCO(n=2) or Bi2212, space group: A2aa, Pearson code: oS60, $T_c = 92\ K$ [Poole 00], lattice parameters are $a = 0.5333$ nm, $b = 0.5485$ nm, and $c = 3.076$ nm, very stable in vacuum [Zakharov 00]), the upper critical magnetic fields $H_{c2}(T,\theta)$ are so large (for example $H_{c2}(0,0) = 31\ T$ [Naughton 88] or quite different estimation result $H_{c2} \approx 100\ T$ [Pint 89]) that the standard anisotropic Ginzburg-Landau (GL) theory yields c-axis coherence lengths ξ_c of the order of 1 Å [Naughton 88] . This is much less than the c-axis lattice spacing 30.6 Å (30.86 Å [Poole 00]) and the Cu-O layer spacing 12 Å [Naughton 88] or 15 Å [Sunshine 88].

We consider the configuration in which **B** is along the **c** axis, perpendicular to the ab planes in Bi2212, so that each vortex line can be thought of as a string of pancake vortices in the planes through which it passes. The vortex system is considered to be three dimensional if the (x,y) positions of the pancake vortices in successive planes are strongly correlated so as to define a continuous vortex line, or it can be two dimensional if the pancake vortices in successive planes move essentially independently. Since the interplane Josephson force

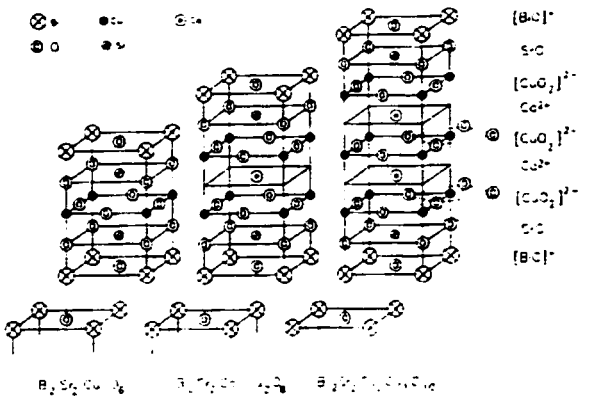

Figure 3.1: Crystal structures of $Bi_2Sr_2Ca_{n-1}Cu_n$ with n=0, 1 and 2.

constant is independent of B while the intraplane force constant is proportional to B, these force constants will be equal at some characteristic crossover field B_{cr} [Fisher 91]. When the applied field B is greater than B_{cr}, the interaction between adjacent pancake vortices in the same layer is stronger than the interaction between those in adjacent layers. This causes the thermal fluctuations to have a quasi-two-dimensional character in the high-field regime.

The interplane coupling in Bi2212 is very weak, therefore the Lawrence-Doniach picture would be more appropriate [Appel90], i.e., BSCCO should be described as a set of discrete superconducting layers whose order parameters are coupled by Josephson interaction [Kleiner 92]. BSCCO is also the most anisotropic HTSC discovered so far exhibiting pronounced anisotropy in its thermodynamic and transport properties [Junod 94]; in the simplest case, it is described by the effective mass or penetration depth ratio γ (γ goes to infinity represents the 2D limit) perpendicular and parallel to the CuO_2 layers.

Currently scientific community believe that in BSCCO, in the extreme case (at higher

fields or temperatures), vortex "pancakes" are formed with circulating currents confined to the CuO_2 planes where the vortex cores threading the superconducting layers may be thought of as wiggly lines. [Schneider 95] The pancakes interact with each other via a pair-wise potential [Feigel'man 90] and via interlayer electromagnetic and Josephson coupling [Daemen 93, 93A, Koshelev 96, Blatter 96]. This dimensional crossover from 3D to 2D (vortex structure or magnetization-temperature m-T plane) is temperature and external magnetic field (including both the magnitude and the direction) dependent. [Schneider 99] Recent studies [Aegerter 96, Lee 97] have shown that in BSCCO, the electromagnetic interaction between the layers dominates over the Josephson coupling if the temperature is lower than about $0.8T_c(0)$. Furthermore, a technique was developed for studying the directionality of internal fields and research shows that for a Bi2212 sample, even at 2 K, any applied field component perpendicular to the **c** axis penetrates freely, as though the material is transparent to applied magnetic fields in the **ab** planes. [Kossler 98] It was also found that the ease of flux lattice melting in BSCCO is related to the weak interlayer coupling. At low fields, the currents parallel to the **c** axis are vanishingly small and therefore the Josephson coupling is very small too and the ordering is dominated by magnetic coupling over a wide region of the B, T phase diagram. [Kossler 98] The pancake-vortex lattice in the anisotropic or layered superconductors defines a tunable soft matter system with astonishing properties. [Blatter 94] The interaction of 2D pancakes and the vortex lattice structure for various magnetic field directions were studied previously. [Clem 91, Bulaevskii 92]

3.3 Vortex Lattice (VL) Phases

In the mean-field limit the phase diagram of type II superconductors has three states: the normal state (usually a metallic phase) at high fields, the mixed state (Shubnikov phase) at intermediate fields in which the lines of magnetic flux are arranged in a triangular Abrikosov lattice and the superconducting state (Meissner-Ochsenfeld phase) at low fields. Furthermore, in the mixed state as the temperature increases, thermal fluctuations destroy the flux lattice near the mean-field transition line and a flux liquid phase enters the (H, T) phase diagram through a first-order vortex lattice melting transition. [Nelson 88, Houghton 89, Zeldov 95] Vice versa, as the temperature is reduced, the vortex liquid undergoes also a first order phase transition to the flux lattice state. [Ruggeri 76] This first order melting transition has been studied by resistivity measurements, observation of a jump in the magnetization, renormalization group, elastic theory, density functional theory and numerical simulations. [Davoudi 01] The FLL in very anisotropic and extreme type II superconductors such as BSCCO are intrinsically soft due to both the quasi-two-dimensionality of these compounds and the long range of vortex-vortex interactions. [Hetzel 92] It is now clear that the response of the FLL to nonuniform perturbations with $k \neq 0$ such as thermal fluctuations (with dominant Fourier modes at the boundary of the Brillouin zone of the reciprocal lattice), softens rapidly with increasing anisotropy. The melting transition (see fig. 3.2) is expected to be first-order according to the standard symmetry considerations [Landau 37] and confirmed through theoretical calculation [Blatter 94], and the experimental observation of a jump in the magnetization measurement in Bi2212 [Pastoriza 94, Zeldov 95] or by μSR [Lee 93] and SANS [Cubitt 93] experiments in $Bi_{2.15}Sr_{1.85}CaCu_2O_{8+\delta}$ and Monte

Carlo simulations of the frustrated XY model [Li 91, Hetzel 92]. The possibility of a first order phase transition being due to decoupling of the different layers has been investigated. [Glazman 91] Note that this first order melting line in the temperature-magnetic field plane is considered to be unrelated to the depinning line $T = T_{dp}(H)$ where the flux lattice depins itself and become more perfect through thermal excitations, which correspondingly gives an increased neutron diffraction signal. [Cho 94, Forgan 97, Fuchs 98] We now know that in the HTSC there exist several exotic vortex lattice (VL) phases owing to the weak coupling between the superconducting CuO_2 layers (which gives rise to various flexible vortices), short coherence length (which enhances their susceptibility to pinning) and high values of T_c (which allows the thermal effect to play a role in the vortex state).

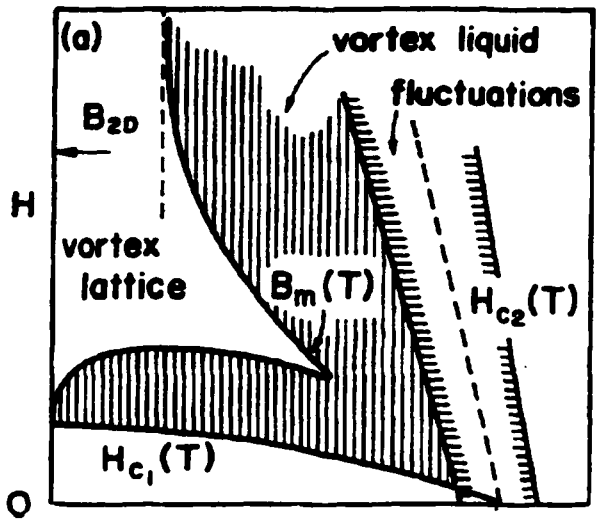

Figure 3.2: Bi2212 vortex phase diagram. [Blatter 94]

Experiments that probe the vortex state of HTSC can be divided into three categories [Sonier 00A], those that measure (i) thermal and transport properties, (ii) electronic structure, and (iii) the inhomogeneous magnetic field. Thermal conductivity, resistivity, and

specific heat measurements belong to (i) and (ii), STM belongs to (ii), and SANS and magnetic imaging with SQUIDs belong to (iii). NMR and μSR probe both (ii) and (iii). μSR measurement of the magnetic field in the VL phase is the main focus of this thesis.

The μSR technique has proven to be a powerful tool for studying the VL phase. [Lee 93, Riseman 95, Sonier 97] To date much attention has been paid to the VL melting and pinning effects in BSCCO and YBCO. [Sonier 00] We know that a characteristic structural feature in Bi2212 is the presence of CuO_2 planes and high anisotropy γ, suggesting strongly two-dimensional (2D) physical properties (for a beautiful experimental demonstration of the 2D character see [Busch 92, Safar 92]). Normal-state resistivity [Martin 88, Jihong 88], upper critical fields [Palstra 88, Murata 87, Naughton 88] and transport critical current [Martin 89] measurements indicate that the superconducting sheets (CuO_2 planes) are weakly coupled and spaced 15 Å apart along the c axis [Sunshine 88]. This coupling between sheets or layers may be treated as a spacial symmetry-breaking perturbation, as discussed theoretically by several groups [Hikami 80, Ito 81] or more recently a combination of tunnelling Josephson currents and electromagnetic interactions [Dalmas 97]. When increasing the magnetic field or the temperature, one expects to observe changes in the typical 3D flux-line-lattice field distribution due to either disordering or motion of the vortices [Harshman 91, Inui 93], a reduction of its dimensionality [Brandt 91, Harshman 93] or its melting to a glass phase or vortex liquid phase [Duran 91, Blatter 94, 97, Brandt 95, Ryu 96, Gingras 96, Lee 97]. Actually, it has been recognized that the magnetic phase diagram of many superconductors contains a vortex liquid regime, in which the magnetization behavior is fully reversible and the transport data show flux flow. [Hao 91]

Generally, at low temperature and for an external field less than the crossover field

B_{cr} [Aegerter 98] ($B_{cr} \approx 1T$ for Bi2212; for a general review of magnetic field induced dimensional crossover phenomena in cuprate superconductors, see [Schneider 99]), a stable lattice of extended flux lines is observed due to an attractive electromagnetic interaction between pancake vortices in different layers which is sufficient to align the vortex cores along the c direction, and its μSR signature is a typical strongly asymmetric field distribution (Monte Carlo simulation shows that this asymmetry depends on the specific form of $\mathbf{B}(\mathbf{r})$ [Wan 99]) with a pronounced tail towards high fields, showing that some of the muon spins precess in the local field produced by flux cores, which is supported by the occurrence of Bragg peaks in the neutron diffraction experiments [Cubitt 93]. Note that although a dimensional crossover is a very possible interpretation, there are other explanations for the observed changes of μSR line shape in Bi2212 as the applied field is increased across B_{cr}. For example, it has been proposed that the Abrikosov lattice transforms to a phase of entangled vortices at high field; this is a pinning-induced transition from a weakly disordered Bragg glass phase to a strongly disordered vortex glass (or pinned fluid) phase. [Sonier 00A and references therein] Studies on the vortex lattice with n-fold symmetry show that generally the field distribution $f(B)$ is located between B_L (B_L is the magnetic field at the center of the lattice cell, which is farthest away from the vortex cores) and B_H (B_H is the highest field inside the vortex core, without which, there will be no high field cut-off B_H and the field distribution extends to infinity) with *only one* maximum at B_{max} (contributed by those points with n-fold symmetry). In numerical simulations, the finite jumps of $f(B)$ at B_L and B_H are caused by the finite field histogram sampling interval ΔB, the probability peak found around B_L is caused for the same reason. If the sampling interval ΔB is reduced, $f(B_L)$ and $f(B_H)$ becomes closer to zero, and the false peak around

B_L will disappear. [Wan 99] Changing the magnetic field tunes the relative importance of the attractive interlayer interaction and the long-range repulsion between vortices in the same layer. Drastic changes occur when B_{ex} exceeds B_{cr} or the temperature exceeds the melting temperature T_m. [Caillol 82] In this case, the energy required for short-range tilt deformations of flux lines becomes smaller than that for shear deformations within the planes, so that the layers of pancakes may move with respect to one another and the core positions in nearby layers no longer coincide. [Lee 95] The field distribution becomes more symmetric, and simultaneously the neutron Bragg peaks disappear indicating the long-range coherence of the flux lattice is destroyed. The change of the shape of the field distribution is quantized by the skewness factor α as we discussed before, which was used by S. Lee et al. [Lee 97] to explore the low field (B,T) phase diagram of BSCCO. They found that there is vortex disorder over wide regions of B and T. Certainly above 20 K or so the flux lattice should be melted for fields even much less than 2.7 T. The melting line can be determined with a Lindemann criterion [Houghton 89, 90, Blatter 96] by comparing the free energy of the 3D VL to the free energy of a collection of 2D liquids [Caillol 82]. In this picture the vortex lattice is expected to melt when the root-mean-square (RMS) thermal average of the vortex displacements from their equilibrium position $< u^2 >^{1/2}$ exceeds some small fraction c_L of the intervortex spacing L. Typically the Lindemann number c_L is of the order 0.1. In an earlier measurement on a BSCCO sample, evidence was also found that the flux lattice melts at high field and low temperature, [Kossler 00] which leads into the higher field measurements, i.e. this thesis work.

Note that the first-order vortex lattice melting transition happens not only in BSCCO but also in YBCO, in which the thermodynamics features of the transition were studied

in detail. [Dodgson 98] In a high external magnetic field, the Bi-2212 system consists of an array of pancake vortices that are uncorrelated in the c direction but may order two dimensionally within each stack of CuO_2 planes. This interpretation is supported by the numerical results [Schneider 95] and experiments [Vinokur 90, Glazman 91, Bernhard 95]. The B_{cr} is on the order of ϕ_0/λ_{ab}^2 where $\phi_0 = 2.07 \times 10^{-15} Tm^2$ is the quantum of flux [Aegerter 96]. B_{cr} is about 2000 G for λ_{ab}=1000 Å . There are also reports that B_{cr} is about 650 G, which is determined by the field at which the pinning energy for a pancake vortex is comparable to the energetic cost of deforming the vortex-line lattice. [Lee 93, Cubitt 93, Aegerter 98]

Recent μSR [Blasius 99] and transport [Hellerqvist 94, Fuchs 98] experiments on under-to-overdoped Bi2212 crystals have also been interpreted as evidence for a two-stage VL (or vortex matter) transition: first the intralayer coupling of the pancake vortices is overcome by thermal fluctuations, then the interlayer coupling is lost. These two processes occur independently at different temperatures. There is also theoretical study on the instabilities of VLL in BSCCO, which predicts the *chain* state, the equilibrium lattice that is similar to the Abrikosov lattice at large fields but crosses over smoothly to a pinstripe structure at low fields. All the features mentioned above happen not only in Bi2212 but also other anisotropic HTSCs.

There are many other important applications of μSR to the study of superconductivity that do not involve measurements in the vortex state, such as studies of the antiferromagnetic and spin-glass phases, measurement of relaxation rates associated with phase transitions and detection of spontaneous internal magnetic fields in heavy-fermion and unconventional superconductors. [Sonier 00A]

3.4 Vortex Dynamics

In Bi2212, the small coherence length and quasi-two-dimensionality determine that the vortex or flux dynamics (flux pinning and flux motion which includes flux flow FF, flux creep FC, flux jump FJ etc.) plays an important role in its electronic and magnetic properties [Tsuneto 98]. The properties of viscous flux flow, flux creep and pinning in anisotropic superconductors have been under intensive investigation. In particular, the anisotropy of the flux-flow conductivity was investigated within the time-dependent Ginzburg-Landau (GL) theory with the anisotropic mass tensor. [Ivlev 91]

We know that in the mixed state of ideal (homogeneous, supercurrent $\mathbf{J}_s(\mathbf{r}) \equiv 0$) or nonideal (inhomogeneous, supercurrent $\mathbf{J}_s(\mathbf{r}) \neq 0$) type II superconductors, at lower temperatures, the magnetic environment (ME) is static and determined by the London equations indirectly, which is the result of solving Maxwell equations or minimizing Gibbs free energy, We also consider appropriate vortex core cut-off to avoid the logarithmically divergent $\mathbf{B}(\mathbf{r})$ at the vortex core (behavior of Bessel function $K_0(r = 0)$), the inhomogeneities of the internal magnetic field cause a line broadening in the magnetic resonance experiments (ESR and NMR) or an enhanced spin-relaxation rate in μSR. At higher temperatures, ME is closely related to the vortex or flux dynamics. We now know, in Bi2212, that the energies required to misalign the 2D pancake vortices are very small and so that as temperature approaches T_c, thermal energies can strongly disrupt the alignment and break up the pancake stack. [Clem 91] Remarkably, the condition for this thermally induced breakup is exactly the same as that for the Kosterlitz-Thouless transition. [Kosterlitz 73, Clem 91] For a complete description of vortex dynamics and recent experiments, see [Huebener 79, Wu 00].

Since the Lorentz force per unit volume of the flux-line lattice (FLL) $\mathbf{f}_L \propto \mathbf{J}_s \times \mathbf{B}$, a flux line can be in a static equilibrium only if the total supercurrent arising from all other sources is zero at that position, which is fulfilled in a uniform or undistorted lattice array. The Lorentz force tends to drive the vortices down the flux density gradient. The flux line can be also in equilibrium if there is pinning force $\mathbf{f}_p$ (proved to be associated with defects experimentally) to balance with it. In the dynamic case, the individual flux line is subject to three additional forces: the Magnus force $\mathbf{f}_m$ [De Gennes 66], the frictional or damping force $\mathbf{f}_\eta$ and the elastic restoring force $\mathbf{f}_{el}$ [Ketterson 99]. Equilibrium and non-equilibrium problems involving elastic lattices and disordered media, such as the dynamics of driven lattices, appear in a variety of systems. Vortex motion through thermal activation is responsible for a number of non-linear phenomena within the class of anisotropic HTSC materials. The energy barrier U, over which vortices jump from one state to a neighboring state via the thermal activation, was measured recently [Wu 00] to study the vortex diffusion and phase diagram in a Bi2212 single crystal. A consequence of the flux motion is a finite electrical field $\mathbf{E} = \mathbf{v} \times \mathbf{B}$ which causes dissipation or voltage noise in the superconductor. To recover the desired property of dissipation-free current flow, the FLs need to be pinned by defects such as vacancies, precipitates, dislocation loops, stacking faults, grain boundaries etc.. The mechanism of flux pinning and vortex motion in type II superconductors was reviewed recently by Wördenweber. [Wördenweber 99]

If the FLL deviates from its ideal configuration (a perfect triangular array) due to dislocations, microscopic disorder, variations in the macroscopic average field, *etc.*, the theoretical μSR lineshape will lose its sharp features at the minimum, cusp and maximum fields. This suggests that the experimental field lineshape can't be adequately fitted by the

theoretical lineshape for the ideal FLL alone. In this case, it was found that μSR data can still be fit to the theoretical lineshape convoluted with a distribution of fields [Herlach 90]

$$n_{smeared}(B) = \int \frac{1}{\sqrt{2\pi}\sigma} e^{-\frac{(B-B')^2}{2\sigma^2}} n(B')dB' \tag{3.1}$$

Brandt [Brandt 88] showed that this convolution is consistent with how random disorder and distortions in the FLL due to flux pinning modify the lineshape from the ideal case.

We assume the vortex displacement is given by

$$\mathbf{s}_v(z) = \mathbf{r}_v(z) - \mathbf{r}_v^0 \tag{3.2}$$

where $\mathbf{r}_v^0$ is the location of the v^{th} flux line in the ideal FLL, then it was estimated that the root mean square of the vortices' displacement has the following value [Riseman 94]

$$\sqrt{\langle s^2 \rangle} = \frac{\sqrt{2}\sigma}{B_0} \left(\sum_{\mathbf{k} \in \mathbf{k}_{BZ}} \frac{k_x^2 + k_y^2}{(1 + k^2/k_h^2)^2} \right)^{-\frac{1}{2}} \tag{3.3}$$

It was shown that a second moment of field $\sigma = 16$ Gauss corresponds to disorder in the FLL of $\sqrt{\langle s^2 \rangle} \approx 6\%$. [Riseman 94]

The vortex dynamics in single crystal Bi2212 at lower fields 3 and 4 kG [Harshman 91] indicates motional narrowing effects associated with vortex motion. A field-dependent localization transition is observed around 30 K. Analysis of data shows that most of the vortices are potentially mobile. The results are found to be consistent with a thermally activated depinning picture.

Chapter 4

Experiments, Results and Analysis

4.1 Experimental Methods

4.1.1 Bi2212 Sample Description

The Bi2212 sample (the exact cation stoichiometry is $Bi_{2.1}Sr_{1.94}Ca_{0.88}Cu_{2.07}O_{8+\delta}$ with $T_c \approx 90K$ and 0.03 stoichiometric error) we used in this study was made from multiple (about fifty in total) high purity single crystals, each with approximate dimensions 3x3x0.1 mm^3. The crystals were assembled into a flat mosaic sample with their c axis aligned, and mounted on a pure aluminum plate. The aluminum plate sample support is used because of its very slow relaxing background μSR signal. The same sample has been used in previous studies. [Kossler 87, 98, Harshman 87, 89, 91] Growing BSCCO single crystals by using the directional solidification method is also being developed in the department here, some Bi2212 samples with size 2X4 mm^2 have been produced in the lab, and the X-Ray Fluorescence (XRF) method was used to characterize the stoichiometry of the samples.

4.1.2 Experimental Setup

Transverse Field μSR (TF-μSR) measurements in external magnetic fields 1.0, 2.7, 3.0, 4.5, 5.5, 6.0 and 7.0 T along the Bi2212 crystalline c-axis were made on the M20 beamline at the Tri-University Meson Facility (TRIUMF) in Vancouver, Canada. Off c-axis low field experiments were also carried out on these samples and data were analyzed by the *Positive Wavelet Transform* technique [Wan 99], however these low field data are not the focus of this thesis. This thesis mainly studies the high field data on Bi2212 which have rarely been studied by μSR researchers.

On the M20 beamline, we denote the upstream beam axis by $\mathbf{z}$, the up vertical by $\mathbf{y}$ and use $\mathbf{x} = \mathbf{y} \times \mathbf{z}$. The muon's polarization was rotated from roughly along the beam to approximately vertical using a crossed-field separator upstream of the sample. The decay positrons emitted from the implanted positive muons are collected and time stamped in the up (U), down (D), left (L) and right (R) detectors. Four histograms containing around 30 million events were aquired with time resolution 0.3125 ns. (These parameters are used in computer model simulations later in this thesis) Sample temperature was controlled between 2 K and 100 K in a He-flow cryostat.

4.1.3 Relaxation Function and Fitting

The four muon spin precession histograms were fitted all at once by the heterodyned technique introduced in chapter 1 combined with a nonlinear least-squares minimization Fortran routine. A summation of one Back-to-back Gaussian signal and one pure Gaussian background signal was used to fit the experimental data. The relaxation function used in the

fitting procedure is as following:

$$P(t) = \sum_{i=1}^{4} \left\{ a_i \sum_{\omega} \cdot b.b.g. \cdot \cos(\omega t + \phi_i) + b_i e^{-\frac{\lambda^2 t^2}{2}} \cos(\omega_0 t + \phi_i) \right\} \tag{4.1}$$

where the b.b.g. function in the equation is

$$b.b.g. \;=\; \begin{cases} e^{-\frac{(\omega-\omega_0)^2}{2\omega_L^2}}, & \text{for } \omega < \omega_0 \\ e^{-\frac{(\omega-\omega_0)^2}{2\omega_R^2}}, & \text{for } \omega \geq \omega_0 \end{cases} \tag{4.2}$$

In the depolarization equation 4.1, there are a total of 16 independent parameters. The Back-to-back Gaussian field profile doesn't have an explicit analytical form of depolarization function $P(t)$ in the time domain; the Fortran fitting program was developed to carry out this fitting task.

Because the field distribution $f(B)$ can't be described by a simple function, instead of using the second moment of $f(B)$ as the relaxation rate σ of the muons, we used a derived parameter $\omega_{ave} = (\omega_L + \omega_R)/2$ as σ. Further, we used $\omega_{diff} = \omega_R - \omega_L$ as indicator of the asymmetry of the field profile. [Kossler 00] A positive ω_{diff} suggests a field distribution with a tail on the right, a negative ω_{diff} suggests a field distribution with a tail on the left. We assumed the asymmetric distribution of the lineshape in the Back-to-back Gaussian function. In this general way, the final fitting results will give us information on the asymmetries of the field distribution $f(B)$.

4.1.4 The Asymmetry/Skewness of $f(B)$

To obtain the skewness ω_{diff} of $f(B)$ at each temperature, we first used the fitting results from the previous run as the current input initial guess values of the 16 parameters; we

then let the program fit on ω_{diff}. For all data, it is very interesting and surprising that the fitting program terminated with an excellent χ^2 (most of them are around 1.05) and gave small ω_{diff} values (around 0.1) with comparable corresponding errors. Thus we suspect that the field profile $f(B)$ may be symmetric at all temperatures. To confirm this, we then fixed the ω_{diff} value at 0 and obtained the fits to experimental data again, which shows excellent χ^2 and the same fitting values statistically for the remaining 15 parameters. By doing so, we concluded that the field distributions $f(B)$ are symmetric at all temperatures and in all fields studied.

It was found that one oscillating signal with asymmetry amplitude about 0.08 comes from muons stopped inside the vortex of the sample; the other slow relaxing oscillating signal with asymmetry amplitude about 0.006 comes from muons stopped in the sample holder, i.e. background. The signal with amplitude 0.08 is symmetric at all fields and temperatures, which is the most interesting and important feature obtained from our experimental data. Data analysis also showed that the background signal amplitude gets smaller at higher fields. In any case, the background signal is 10 times less than the vortex signal.

4.2 Field Profiles and Relaxation Rates

4.2.1 Typical μSR Spectrum and Field Profile

Due to the high precession frequency, a modified Cosine Fourier Transform was used to obtain the field profiles at different temperatures and fields. The final field profile is the average of the four histogram results (experimental data show that the differences between the field profiles extracted from different detectors are negligible and are consistent with

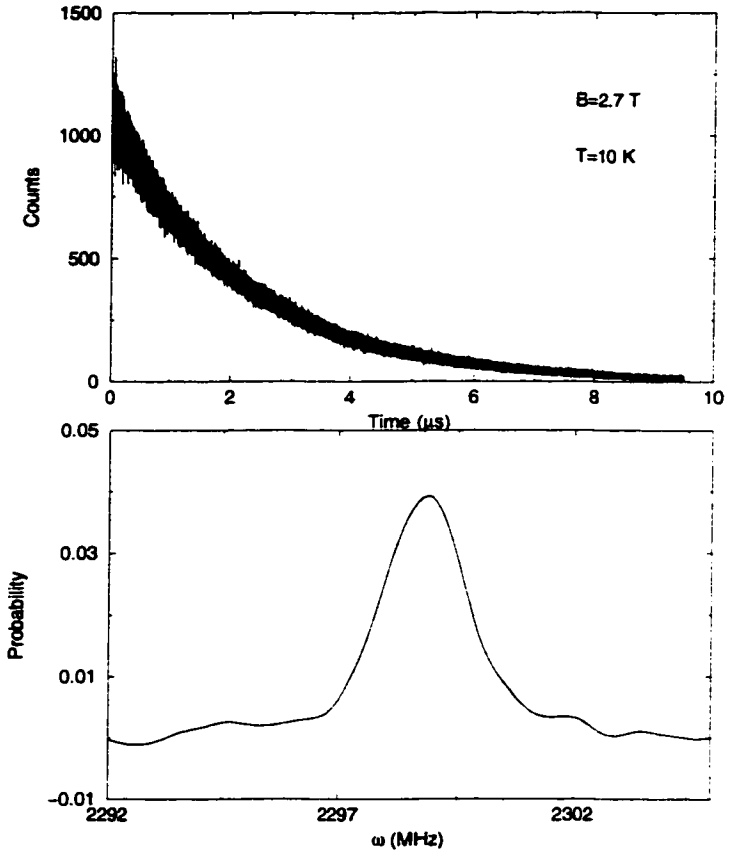

Figure 4.1: μSR spectrum and the corresponding field profile (B=2.7 T, T=10 K).

each other). A typical μSR spectrum and the corresponding field profile on the *ab* basal plane are shown in fig. 4.1.

It is not evident from fig. 4.1 how the signal behaves, because the precession frequency is too high in the time window. To visualize the relaxing precession signal, we showed the asymmetries both above and below the superconducting transition temperature T_c in a *rotating reference frame*. From fig. 4.2, it is clear that the relaxation rates are higher at lower temperatures.

Typical field profiles at different temperatures in external field B=2.7 T are shown in fig. 4.3.

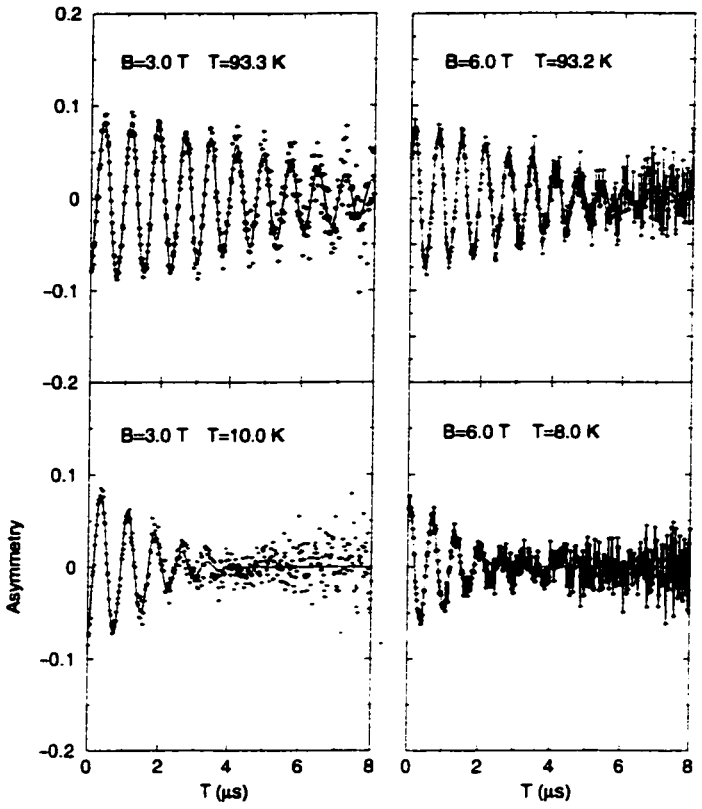

Figure 4.2: Typical muon spin relaxation signals and corresponding fitting results above and below T_c in a *rotating reference frame*. Only 1 out of 4 histograms was shown here.

4.2.2 Review of Previous Study

Before we discuss our experimental results of field profiles, relaxation rates and asymmetry/skewness of $f(B)$ on Bi2212, we review here some relevant studies on Bi2212. The internal field distribution of the same sample in external fields 3, 4 and 15 kG was measured before by Harshman *et al.* [Harshman 91], where a rather narrow and symmetric distribution was observed at temperatures higher than 30 K. At lower temperatures, the line shape becomes broadened and asymmetric. Further analysis suggests a motional narrowing of the internal field distribution arising from the constrained vortex motion, which freezes

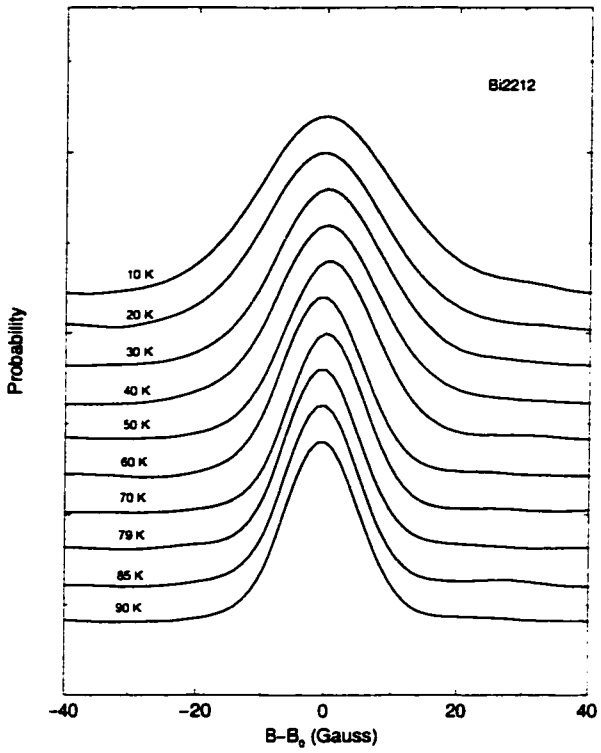

Figure 4.3: Typical field profiles (average FT of 4 histograms) on the ab plane in $B_{ex} = 2.7T$, the horizontal axis was calibrated to the average field B_0.

out with decreasing temperature at these fields. Further, the narrowing of the distribution could be due to one or more of several causes: motion of straight flux lines, curvature of flux lines or breaking-up of flux lines into pancakes. [Forgan 97] In the case of flux entanglement [Nelson 88] or the disordered vortex disks of the Lawrence-Doniach (LD) model [Lawrence 70], the measured line shape would be narrower. It was predicted that in high fields, due to the inter-vortex interactions, the vortex disordering becomes increasingly more important than the motional narrowing and vortex correlation effects. In any cases, the narrowing of the field profiles is associated with the dynamics of the pancakes. It's interesting to notice

that a back-to-back cutoff exponential function [Harshman 89] was used to analyze the field profiles in the lower fields.

Another BSCCO sample ($Bi_{2.15}Sr_{1.85}CaCu_2O_{8+\delta}$) was studied by the TF-$\mu$SR technique in several low fields 100, 200, 300 and 450 G. [Lee 95] It was found that the temperature and strong field dependences of the relaxation rate can be described by a 2D pancake model [Clem 91] after considering the thermal fluctuations of the vortices about their average positions and vortex lattice melting transition at a critical or crossover field B_{cr}. Lee's sample was also used by Aegerter to probe the angular dependence of the disorder crossover field by TF-μSR (up to 2000 G) and torque magnetometry techniques [Aegerter 98] where the crossover field was found to scale only with the field component in the c direction.

Most recently, underdoped Bi2212 was studied by Blasius *et al.* and evidence was found for a partial restoration of the vortex lines at higher fields (up to 1 T), which is suggested to be related to the increase of vortex-vortex interaction and the subsequent change from single-vortex pinning to collective pinning. [Blasius 00]

4.2.3 Our Results and Explanations

Our high transverse field (1.0, 2.7, 3.0, 4.5, 5.5, 6.0 and 7.0 T) μSR experiments (the upper critical field for this sample is estimated as 44 T [Harshman 91] so that the sample is assumed in a mixed state) shows that, in a unique external magnetic field, the precession frequency of the muons almost remains constant at all temperatures. It suggests that the external magnetic field is very stable during the whole experimental period.

The experimental muon relaxation rates as functions of temperature and field are shown in fig. 4.4. In this plot, the ω_{ave} values are the total relaxation rates, which include the con-

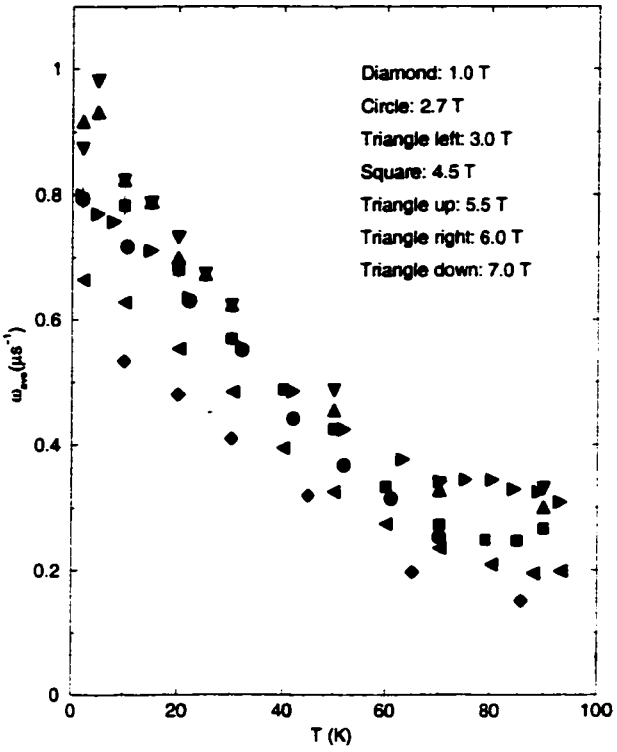

Figure 4.4: Total muon spin relaxation rates in 1.0, 2.7, 3.0, 4.5, 5.5, 6.0 and 7.0 T external magnetic fields. The relaxation rates increase from 0.2-0.3 μs^{-1} above transition temperature to 0.6-1.0 μs^{-1} at lowest temperature and increase only slightly at higher magnetic fields(less field dependence).

tributions from various sources: vortex, nuclear dipole, instrument broadening, background etc..

In order to study the vortex state solely, we need to filter out all effects except the vortex lattice on ω_{ave}. The nuclear dipole, instrumental broadening, magnetic field gradient and background contributions to the relaxation rate ω_n were subtracted from the total relaxation rate ω_{ave} according to formula $\omega_{sc} = \sqrt{\omega_{ave}^2 - \omega_n^2}$, where ω_n is determined from data above the superconducting transition temperature T_c because above T_c, no vortex is formed inside

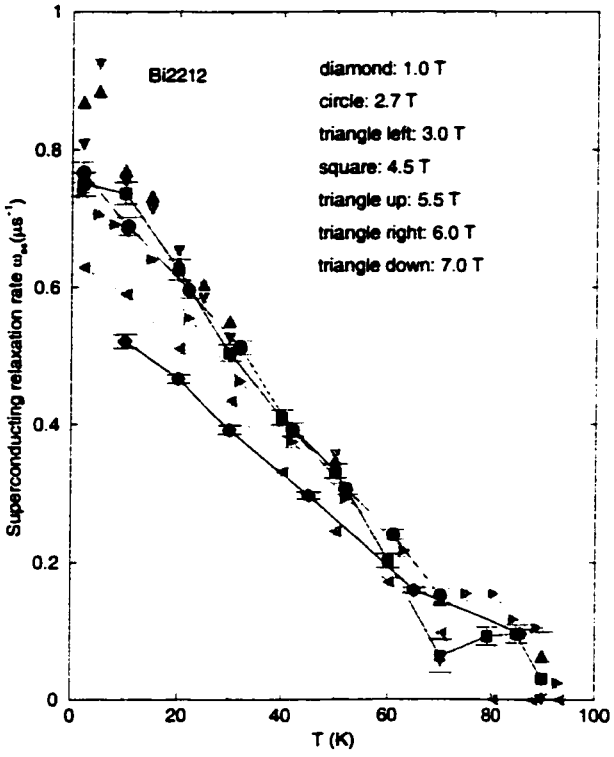

Figure 4.5: Superconducting muon spin relaxation rates in 1.0, 2.7, 3.0, 4.5, 5.5, 6.0 and 7.0 T external magnetic fields. The general behavior of the relaxation rates is consistent with the direct observations of the field profiles and the μSR spectra in the *rotating reference frame*.

the samples. Thus the pure superconducting relaxation rates ω_{sc} are obtained (fig. 4.5).

We can see from the plot, in the temperature range studied, $\omega_{sc}(T)$ demonstrates *linear* temperature dependence behavior. At lowest temperature, the superconducting relaxation rate $\omega_{sc}(0)$ at all fields is about 0.8 μs^{-1}. ω_{sc} are also found to be almost field independent for early data sets at 2.7, 4.5, 5.5 and 7.0 T and increase only slightly with increasing fields for another set of data at fields 1.0, 3.0 and 6.0 T.

For comparison purpose, in fig. 4.6 we have shown ω_{ave}, ω_{diff} vs. T in superconducting YBCO in magnetic fields 1.0, 3.0 and 6.0 T. It is clearly seen that ω_{ave} vs. T in YBCO has

the similar behavior as that in Bi2212, however, ω_{diff} vs. T shows that the field distribution $f(B)$ develops asymmetry between 0.5 and 1.5 μs^{-1} below the transition temperature T_c and maintains it down to the lowest temperature in the experiment. Furthermore, from fig. 4.6, we can see that the higher the magnetic field, the lower the transition temperature T_c; T_c drops from around 88 K at 1.0 T to 81 K at 6.0 T, which is consistent with the general knowledge about the superconductors.

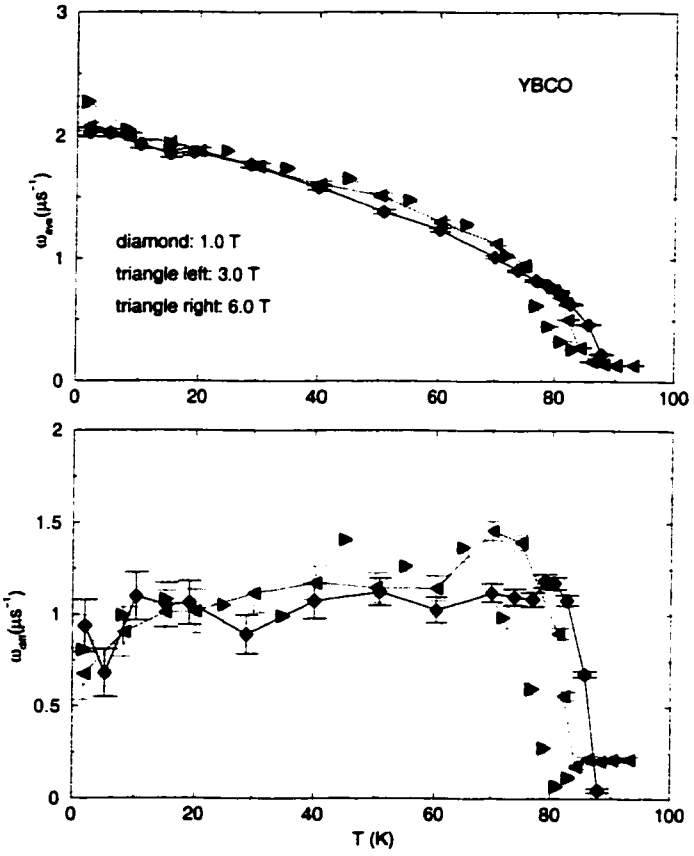

Figure 4.6: ω_{ave} and ω_{diff} obtained on superconducting YBCO in magnetic fields B=1.0, 3.0 and 6.0 T using the same analysis procedure introduced in the text. ω_{ave} vs. T in YBCO shows similar behavior to that in Bi2212, however, ω_{diff} vs. T shows that the field distribution $f(B)$ develops asymmetry between 0.5 and 1.5 below the transition temperature T_c and maintains it down to the lowest temperature in the experiment.

Overall, the field dependence of $\omega_{sc}(T)$ in Bi2212 is weak and small, which can be

explained excellently by a recently proposed dynamic pancake disorder model, which we will study later in detail. [Kossler 02]

In this model, disorder is introduced by randomly displacing the pancake layers, and the magnetic field probability distributions are calculated for a range of applied fields, degrees of disorder and other parameters. Computer simulation shows that the field distribution $f(B)$ narrows and loses asymmetries rapidly with increasing disorder. In fact, it was observed although not in such high field that Bi2212 single crystals display considerable lower values of the relaxation rates due to random pinning. [Ansaldo 91, Lee 93, Aegerter 96, Sonier00] By contrast, in optimally doped YBCO, local pinning broadens the μSR line shape thus increasing the relaxation rate due to the random displacements of 3D vortex lines. [Brandt 91]

We know that a weak temperature dependence of relaxation rate for $T \ll T_c$ suggests there is an energy gap in the spectrum of excitations [Aeppli 87, Harshman 87, Pümpin 90] as expected for conventional s-wave pairing ("conventional" means the gap function of superconducting pairing state has the full crystal point group symmetry), which is certainly not the case in our data. Our relaxation data at low temperatures show a linear temperature dependence, which may suggest a pairing state with nodes in the gap [Scalapino 95] of $Bi_2Sr_2CaCu_2O_8$ [Jacobs 95, Lee 96] since it was also shown [Roddick 95] that the phase fluctuations of the superconducting order parameter, as proposed by Emery and Kivelson [Emery 95], can also lead to such a linear T dependence.

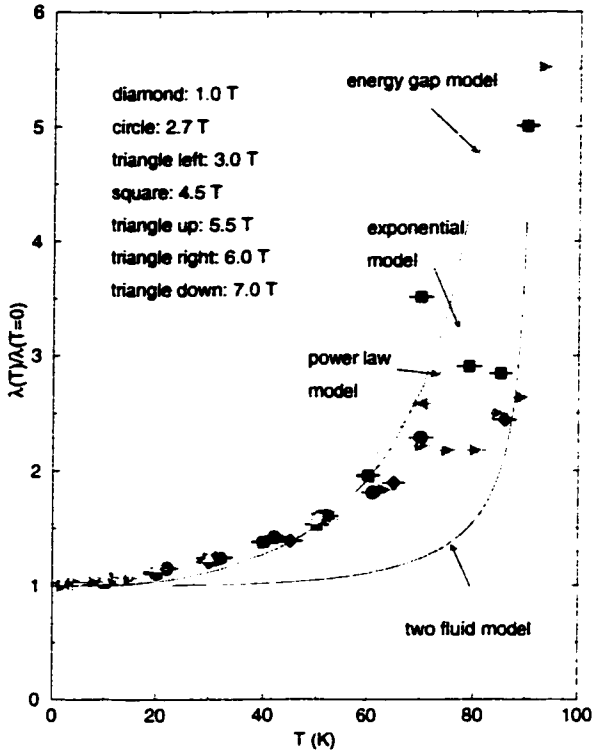

Figure 4.7: Normalized experimental penetration depths and several theoretical predictions.

4.3 Penetration Depths

Experimentally, the penetration depth can be studied through various complementary techniques such as μSR, dc magnetization, torque magnetometry, rf-resonance method etc.. μSR is especially suited to measuring the penetration depth λ because it does not require special-purpose samples such as thin films or spheres of controlled dimensions. The penetration depth $\lambda_{ab}(T)$ of Bi2212 (estimated between 400 and 500 nm from the literature) was studied before by Waldmann *et al.* up to 14 Tesla through the reversible magnetization measurement by torque magnetometry. [Waldmann 96] A linear temperature dependence of $\lambda_{ab}(T)$

at low temperatures was observed in a sample with high maximum T_c. Samples with significantly reduced T_c showed a quadratic temperature dependence. The results were shown to be consistent with a $d_{x^2-y^2}$-wave model with resonant impurity scattering.

A superconductor with s-wave pairing exhibits a finite excitation energy with a minimum energy gap Δ_{min}. Therefore for clean superconductors $\lambda(T)$ at low temperatures varies as $\lambda(T) - \lambda(0) \propto exp(-\Delta_{min}/k_BT)$ (exponential model). [Mühlschlegel 59, Tinkham 75] This model seems to be able to fit our data at the lower temperature end, however it fails at intermediate and high temperatures. Thus our data do not support a pure s-wave pairing with a constant gap.

The penetration depth calculation by the simple anisotropic extension of the BCS theory shows a power law of temperature behavior $\lambda(T) - \lambda(0) \propto (T/\Delta_0)^\alpha$ at low temperatures [Gross 86] where $\alpha = 1$ is an indication of line nodes in a 3D system (or point nodes in a 2D system) in the $d_{x^2-y^2}$ state. It is believed that the $d_{x^2-y^2}$ symmetry is very probable in HTSC through the results of phase-sensitive experiments. [Harlingen 95] In fact, all of the possible non-s-wave spin singlet pairing states of a superconductor with tetragonal or orthorhombic symmetry and a spherical or cylindrical Fermi surface have line nodes in the gap leading to a linear temperature dependence [Gross 86, Annett 91], $\lambda(T) - \lambda(0) \propto T$, in the clean limit. We know that to the first order, the Taylor expansion of any temperature dependent function at $T = 0$ will have this linear temperature dependence, thus we need to be very careful during the data analysis. Strong impurity scattering may change the behavior to $\lambda(T) - \lambda(0) \propto T$ for both s- and d-wave models. [Arberg 93] It was also found that for a d-wave superconductor with resonant scattering even a small impurity concentration may give rise to a quadratic temperature dependence below a crossover temperature T^*. Above

T^* the linear term is conserved. [Hirschfeld 93] The study of the penetration depth at low temperature is a comprehensive issue, which includes contributions from extrinsic origins such as the demagnetization effect, weak link effect, and crystalline effect, and intrinsic origin such as the superconducting gap structure and the symmetry of pairing mechanisms. [Maeda 92] Unconventional pairing mechanisms in different classes of superconductors were given in a recent review article [Annett 99] where the bismuthates, fullerenes and $LiTi_2O_4$ are clearly s-wave, Sr_2RuO_4 is almost certainly p-wave, while for other systems, such as the borocarbides, organics and the C15 Laves phases, the various experiments can be contradictory and so it is not possible to draw a definitive conclusion at this stage.

From our result in fig. 4.7, we can see that, at low temperatures (less than 20 K), data are not significant statistically to tell the differences between the linear and square power law models. At higher temperatures, that the power law predictions deviate from the experimental data suggests excitations from some other pairing mechanism, very possibly an s-wave component induced near the vortex core. [Berlinsky 95, Franz 96, Xu 95, 96] From the standpoint of the spontaneous symmetry breaking, in a bulk sample with perfect crystal symmetry, the order parameter transforms according to an irreducible representation of the crystallographic point group. [Sigrist 91] For example, in a crystal of tetragonal D_4 symmetry, only $d_{x^2-y^2}$ symmetry is allowed. However, near interfaces, surfaces or impurities, which may be affected by the external magnetic field, the $d_{x^2-y^2}$-wave order parameter fluctuates spatially and hence induces components of other symmetry. [Choi 97] Recent angle-resolved tunneling, angle-resolved scattering and torque measurements performed on Bi2212 and other hole-doped cuprates support a two order parameter (OP) scenario: the one responsible for pairing has $d_{x^2-y^2}$ and the other responsible for phase

coherence, has an anisotropic s-wave symmetry. [Mourachkine 99]

4.4 Field Profile: Skewness Discussion

From the plots of skewness $\alpha_G(x)$ (see fig. 2.1)

$$\alpha_G(x) = \frac{[\sqrt{\frac{2}{\pi}}(x-1)(3x-x^2-1)+\frac{4}{\pi}\sqrt{\frac{2}{\pi}}(x-1)^3]^{\frac{1}{3}}}{[(1-\frac{2}{\pi})(1-x)^2+x]^{\frac{1}{2}}} \tag{4.3}$$

of the Back-to-back Gaussian function (where $x = \frac{\sigma_R}{\sigma_L}$) and the skewnesses of other functions, it can be seen that skewness always changes sign sharply when the field profile is close to but not symmetric. [Wan 99] Further, the skewness definition based on the second and third moments of the field profiles (eq. 2.20) is not sensitive to the asymmetry of the field profiles at all when $x = \frac{\sigma_R}{\sigma_L}$ is much greater than 1. Considering the accuracy of the field profiles obtained from Fourier Transforms, we need to have a better way to identify the asymmetry or the skewness of the field profiles. As recommended by Kossler, [Kossler 00] parameter $(\sigma_R - \sigma_L)$ or $(\sigma_R - \sigma_L)/(\sigma_R + \sigma_L)$ was used to denote the skewness of the field profiles.

4.4.1 Back-to-back Gaussian and Back-to-back Exponential Field Profiles

We assumed the asymmetric Back-to-back Gaussian field profiles during the fitting procedure. First we obtained excellent fits (χ^2) with the parameter ω_{diff} fixed at zero, which leads us to suspect that the field profiles are indeed symmetric. We then let the parameter ω_{diff} go and allow the fitting program to give a fitting result; the final fitting results still give us a value around zero with comparable error bar. In this way, we drew the conclusion

that the field distribution is symmetric in all experimental fields and at all experimental temperatures. This suggests that in such high fields (far beyond the critical field B_{cr}), *ab* planes totally lost registry and correlation with other layers and no phase transition was observed as reported in refs. [Lee 93, Bernhard 95, Aegerter 96, Lee 97, Blasius 99] As far as we know, there are no similar high field results obtained on Bi2212, which makes this thesis work more interesting.

To check the behavior of the skewness of the field profiles and the muon spin relaxation rate as functions of temperature which we have obtained from the μSR data, we used a similar method but another fitting function to analyze the same data. It can be proven that the $P(t)$ of a Back-to-back Exponential field profile has the following analytical form

$$\begin{aligned} P(t) &= \Re(e^{i(\omega_0 t+\phi)} \frac{\frac{1}{\frac{1}{\lambda_L}-it} + \frac{1}{\frac{1}{\lambda_R}+it}}{\lambda_L+\lambda_R}) \\ &= \frac{\cos(\omega_0 t+\phi)(1+\lambda_L\lambda_R t^2) + \sin(\omega_0 t+\phi)(\lambda_R t - \lambda_L t)}{(1+\lambda_L^2 t^2)(1+\lambda_R^2 t^2)} \end{aligned} \tag{4.4}$$

where ω_0, λ_L, λ_R and ϕ are four parameters characterizing the shape of the field profile and also determining the uniqueness of $P(t)$. This function was implemented in the Fortran data analysis program to fit all 4 histograms of U, D, L and R detectors in the time domain. In this straightforward way, the results tell us the general features of μSR data and field profiles. For each run, a 19-parameter fit was obtained, from which the values of λ_L and λ_R were extracted. $\frac{\lambda_R-\lambda_L}{\lambda_R+\lambda_L}$, an indicator of the skewness of the field profile, as a function of temperature, is plotted in the following figure. The second moment of the Back-to-back Exponential field profile or the relaxation rate of the muon spin, $\lambda = \sqrt{\lambda_R^2+\lambda_L^2}$, as a function of temperature, is also plotted in the same figure. From the figure we can see that the relaxation rate is almost field independent, which is the same conclusion we drew from

the Back-to-back Gaussian function analysis; the skewness is between 0 and 0.1, which is very small (see fig. 2.1), indicating the field profiles are very symmetric. It is also interesting to note that at low temperatures, $\lambda_R - \lambda_L$ is slightly negative, which suggests a small tail to the left side of the field profile. This interesting feature is successfully simulated in our pancake vortex disorder modelling later.

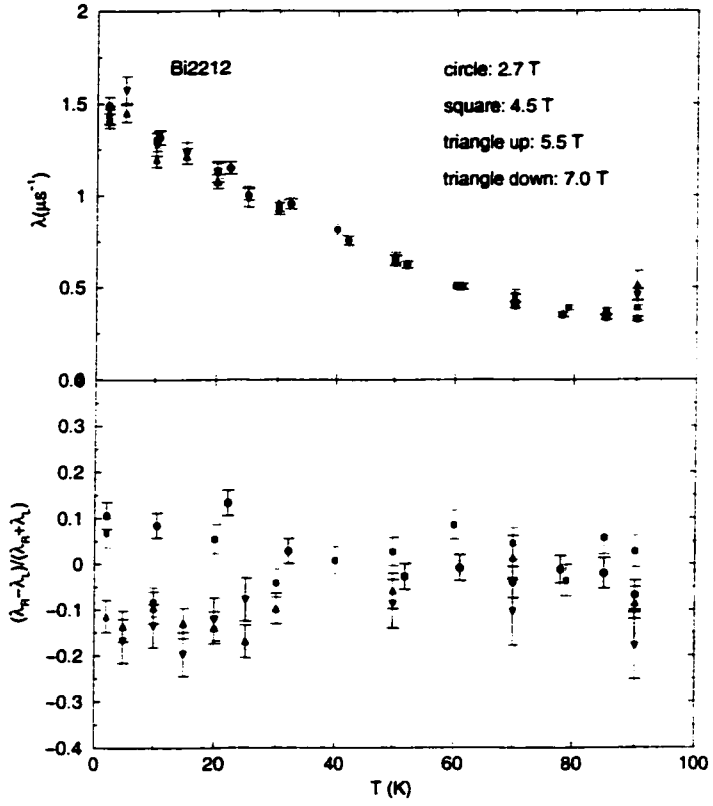

Figure 4.8: Muon spin relaxation rate λ and $\frac{\lambda_R - \lambda_L}{\lambda_R + \lambda_L}$, an indicator of the skewness of the field profile, as functions of temperature in external magnetic field B=2.7, 4.5, 5.5 and 7.0 T are obtained from the Back-to-back Exponential fittings as described in the text.

4.5 Pancake Vortex Disorder Theory

4.5.1 Vortex and Vortex Disorder

When a type II superconductor's temperature is within the characteristic T_{c1}-T_{c2} range and an external magnetic field is applied, the material is in a mixed state. In this state some magnetic field enters the material. This infiltration occurs at pinning sites called vortices, where it is energetically favorable for the magnetic field to enter the sample. These vortices form a so-called Flux Line Lattice (FLL). Experiment has shown that in most cases the energetically favorable form of the FLL is a triangular grid.

Generally, an FLL entering a sample can be modelled as spaghetti strands. However, a spaghetti strand is a continuous line that is well ordered, which may not mirror the reality of a flux line within BSCCO. In fact, many macroscopic properties of HTSC besides BSCCO carry the signature of a layered structure. It is well known that the copper plane to copper plane coupling in BSCCO is quite weak. This led J. Clem to posit pancake vortices, vortices referred to only one plane, as the building blocks of vortex lattices in BSCCO, i.e. the stacked pancake model. [Clem 91] This model better describes the disorder that occurs in a flux line as it penetrates a superconducting material. As more pancakes/layers are added, the stack becomes unstable and shifts until the point is reached where the position of the top of the stack has little correlation with the position of the bottom, and disorder is complete. This corresponds well with what occurs in reality. As the temperature of a superconductor is increased, the disorder of the flux lines within the sample increases.

4.5.2 Magnetic Field Calculation

J. Clem has provided a solution for the magnetic field arising from one pancake vortex and shown that a regular lattice built from such pancakes produces the field distributions expected for the usual London solution vortices. [Clem 91] The stacks of pancake vortices would be easily longitudinally disordered as a consequence of the very weak interlayer coupling. In order to model our μSR data on Bi2212, a means to calculate fields from disordered stacks of pancake vortices has been developed. It is the effect of this disorder of vortices on the magnetic field distribution $f(B)$ in which this thesis is particularly interested.

To calculate the fields from the vortices, we first calculate the fields for a regular array. For these regular array fields, we assume that the field is parallel to the **c** axis and then use two different approaches, first, the reciprocal lattice approach, and second the direct sum of the fields from individual vortices. These will then be used with the field calculations for a disordered array of individual pancake vortices to determine the field distributions for the overall disordered system. The schematic diagram for a disordered pancake vortex system is shown in fig. 4.9.

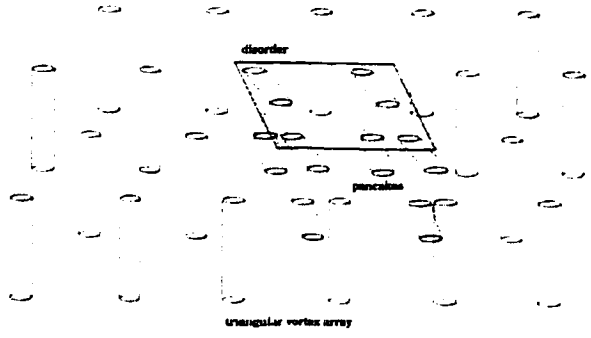

Figure 4.9: The general disorder vortex picture used in our process of magnetic field calculation.

4.5.2.1 Reciprocal Lattice Calculation of $\mathbf{B}_{RL}(\mathbf{r})$

Since we assume the field is parallel to the c axis these calculations become identical to those of the isotropic case with $\lambda = \lambda_{ab}$. Thus:

$$\mathbf{b}(\mathbf{r}) = \sum_{\mathbf{G}} \mathbf{b}(\mathbf{G}) e^{i\mathbf{G}\cdot\mathbf{r}}$$

$$\mathbf{b}(\mathbf{G}) = \frac{B}{\Phi_0} \int \mathbf{b}(\mathbf{r}) e^{-i\mathbf{G}\cdot\mathbf{r}} d^3\mathbf{r}$$

$$\mathbf{b}(\mathbf{G}) = \frac{e^{-\xi^2 G^2/2}}{1 + \lambda^2 G^2} \tag{4.5}$$

The G's are the reciprocal lattice vectors, and B is the average field strength over the FLL unit cell. The exponential term with ξ is used to approximate the results of a finite vortex core. For the present calculation ξ was taken to be small and constant. Thus the effects seen in the line shape which might be interpreted as being associated with core size effects are, in our calculations, arising only from disorder.

4.5.2.2 Single Vortice Field $\mathbf{B}_{SV}(\mathbf{r})$

In the isotropic case, the magnetic field from a single, three-dimensional vortex is:

$$\mathbf{b} = \frac{\Phi_0}{2\pi\lambda^2} K_0(\frac{\rho}{\lambda})\hat{z} \tag{4.6}$$

where K_0 is the zero order Bessel function of imaginary argument and $\hat{z}$ is a unit vector in the z direction. [De Gennes 89] The overall field distribution can then be obtained by summing the fields from an array of such vortices. It has been found that the sum must be taken over a very large array if the average field is to be accurately reproduced.

4.5.2.3 Pancake Fields $\mathbf{B}_P(\mathbf{r})$

The field distribution for a pancake vortex associated with a single layer has been found by Clem. [Clem 91] This field distribution is:

$$\mathbf{b} = \hat{\rho} b_\rho(\rho, z) + \hat{z} b_z(\rho, z) \tag{4.7}$$

where $\hat{\rho}$ and $\hat{z}$ are the unit vectors in cylindrical coordinates ($\hat{\rho} = \hat{x}\cos\phi + \hat{y}\sin\phi$) . The field components for such a vortex in an infinite stack of superconducting layers is:

$$b_z(\rho, z) = \frac{\Phi_0}{2\pi\Lambda r} e^{-r/\lambda_{||}} \tag{4.8}$$

$$b_\rho(\rho, z) = \frac{\Phi_0}{2\pi\Lambda\rho}\left(\frac{z}{|z|}e^{-|z|/\lambda_{||}} - \frac{z}{r}e^{-r/\lambda_{||}}\right) \tag{4.9}$$

where Φ_0 is the magnetic flux quantum, Λ is the thin-film screening length, $\lambda_{||}$ is the effective penetration depth ($\lambda_{||} = (s\Lambda/2)^{1/2}$, s is the spacing between sheets), and $r = (\rho^2 + z^2)^{1/2}$. These fields are summed to produce the magnetic field from a lattice of pancake vortices.

4.5.2.4 Obtaining the Magnetic Field Probability Distribution $f(B)$

The final spatial magnetic field in the sample is determined by

$$\mathbf{B}(\mathbf{r}) = \mathbf{B}_{RL}(\mathbf{r}) - \mathbf{B}_{SV}(\mathbf{r}) + \mathbf{B}_P(\mathbf{r}) \tag{4.10}$$

Once the spatial field values are found we determine in the usual way the probability distribution $f(B)$ of the values contained in the data.

$$f(B) = \int_A \delta((B(x,y) - B)dA \tag{4.11}$$

Here A is the area associated with one flux quantum.

4.5.3 Calculation: Including Disorder

First we compared the fields calculated with a regular array of pancakes to those obtained for a regular array of single vortices. Excellent agreement was found.

To calculate the fields including disorder we first calculated the fields in the reciprocal vortex lattice space for a regular lattice (assumed to be triangular) and the corresponding fields in real space, then subtracted the fields for nearby regularly arranged single three-dimensional vortices. Finally we added the fields from a disordered array of pancake vortices corresponding to the 3 dimensional vortices that we had subtracted.

The pancake disorder was generated by considering the pancakes in a given layer to be regularly arranged, but to allow this two dimensional lattice to wander from a central plane position in a random walk. Thus if $r_x(i)$ is the x component of the position to which the i^{th} central pancake has wandered, then

$$r_x(i+1) = r_x(i) + sc \cdot \delta_x \tag{4.12}$$

where sc is a scale factor in kÅand δ_x is a random number chosen from a gaussian distribution of unit σ. The y component and the values for layers below the central plane (negative i) are chosen similarly.

A further complication was that since the wandering after many layers could become larger than a vortex lattice spacing it was necessary to map the wandered position of the central pancake back to within the direct lattice 2 dimensional Wigner-Seitz cell centered on the central-plane pancake array origin.

We determined the z component of the magnetic field in the central plane and then determined the magnetic field distribution $f(B)$ from this. We found that with large sc the

average field dropped off slightly. This is a consequence of the loss of central density even with the remapping described above.

There are 6 parameters we can vary in the modelling process: the average magnetic field B_0, the penetration depth λ, the scale factor *sc*, the total pancake layers *nsh*, the number of vortices subtracted and added *npanxy* and the number of averaging *nave*. We will systematically study the effects of all these parameters on the characteristics, especially the average relaxation rates and the asymmetry of the field profiles.

4.5.4 Other Theories

The influence of different kinds of lattice deformation on $f(B)$ was studied by Brandt. [Brandt 88A, 91] A qualitative theory was given by Koshelev [Koshelev 96] to explain this phenomenon, where the high field tail or the excess magnetic field δB in the vicinity of a wandering vortex line is determined by pancakes belonging to this line at distances smaller than vortex lattice constant a from the given point, i.e.

$$\delta B = B_\lambda s \sum_{r_N < a} \frac{1}{r_n}, \; r_n = \sqrt{z_n^2 + [u(z_n)]^2} \tag{4.13}$$

Here r_n is the distance of the pancake in the nth layer from the chosen pancake in the zeroth layer. s is the interlayer distance. Based on these assumptions, it was found when the random wandering distance is at the cut-off value $z_{cut} = a$, the high field tail disappears and correspondingly the field distribution $f(B)$ becomes symmetric.

4.5.5 Modelling Results

4.5.5.1 Smearing Factor *smear*

From fig. 4.10, we can see that the field distribution $f(B)$ calculated from the model generally has sharp peaks and edges, which is rarely observed in experiments due to various broadening effects in the sample or instruments. To get the modelling results close to the observed field distribution, we add appropriate smearing to $f(B)$ similar to the technique introduced in eq. 3.1 in chapter 3. The appropriate smearing will make the field distribution $f(B)$ smoother but still maintain the general shape of $f(B)$. After some trials, we chose the smearing factor *smear*=9 gauss. The smearing effect can be seen in fig. 4.11. The same smearing factor was used in all the calculations later.

4.5.5.2 Effect of Parameter *npanxy* on $f(B)$

In the previous section, we decided to use the smearing parameter *smear*=9 gauss. There are still 6 parameters that need to be decided, B, λ, *sc*, *nsh*, *npanxy* and *nave*, where B is the average magnetic field in the sample, λ is the penetration depth, *sc* is the scale factor, *nsh* is the total number of layers we are considering, *npanxy* is a parameter indicating how many disordered vortex lines we are modelling, and *nave* is the number of times we repeat the same model calculation.

Let's first look at the parameter *npanxy* and study the rest of the parameters systematically later. We calculated the field distribution $f(B)$ in four cases *nave*=2, 4, 8, 16 (with the rest of the parameters fixed). The results are shown in fig. 4.12, which indicates that our model is almost independent of this parameter. Macroscopically this means that the

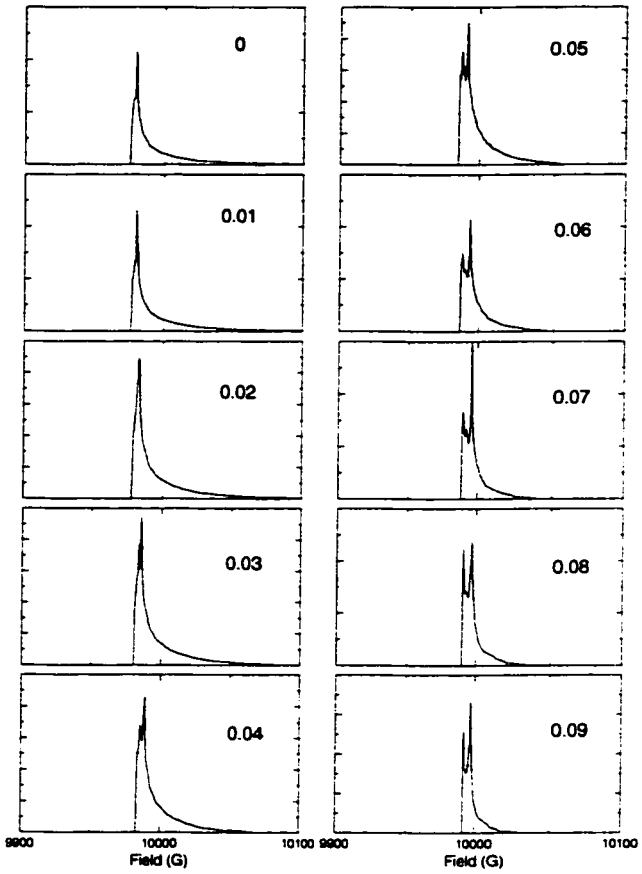

Figure 4.10: A serial plot of magnetic field distributions showing the effect of the pancake disorder scale factor *sc*. It can be seen clearly from these plots, as *sc* increases, the field distribution becomes more narrowed and symmetric and having a complicated multi-peak structure. Due to the broadening of the field profile, the multi-peak structure is hardly discernable in experiments.

field distribution $f(B)$ does not depend on the beam size or sample size, which is reasonable.

We chose $npanxy$=4 in all the following modelling process.

4.5.5.3 General Effects of Scale Factor *sc*

From the previous section, we know that *sc* is an important parameter indicating the amplitude of randomness of pancakes relative to the vortex lattice spacing a. In fig. 4.10, we showed the general effect of *sc* on the field distribution $f(B)$ without any smearing. By increasing the amplitude of *sc* (for comparison, the vortex lattice constant is 0.3 k$\mathring{A}$ in this

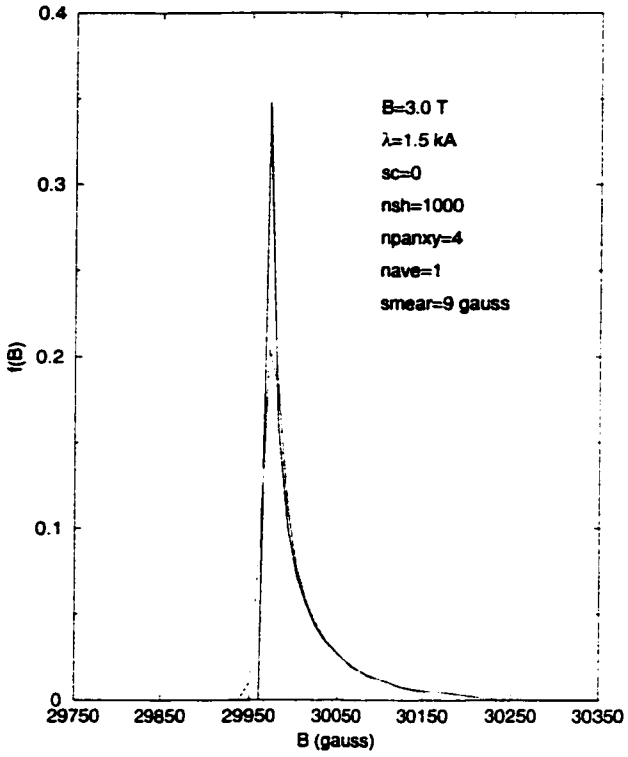

Figure 4.11: This plot shows that an appropriate smearing factor will both smoothen and maintain the field lineshape.

case), we observed the changing of the symmetry and shape of the field distribution. The result is what we expect statistically according to the Central Limit Theorem. Naturally if we assume the sample temperature T is monotonically related to *sc*, it is not difficult to understand why the relaxation rate (second moment) and asymmetry of the field distribution are functions of temperature T.

In some previous research work, each pancake vortex is assumed to be under the influence of an effective potential well $U(\rho)$. It was shown [Clem 91] that at very low temperature, where $K_B T \ll \phi_0^2/16\pi^2\lambda$ (λ is the 2D screening length), the root-mean-square displacement

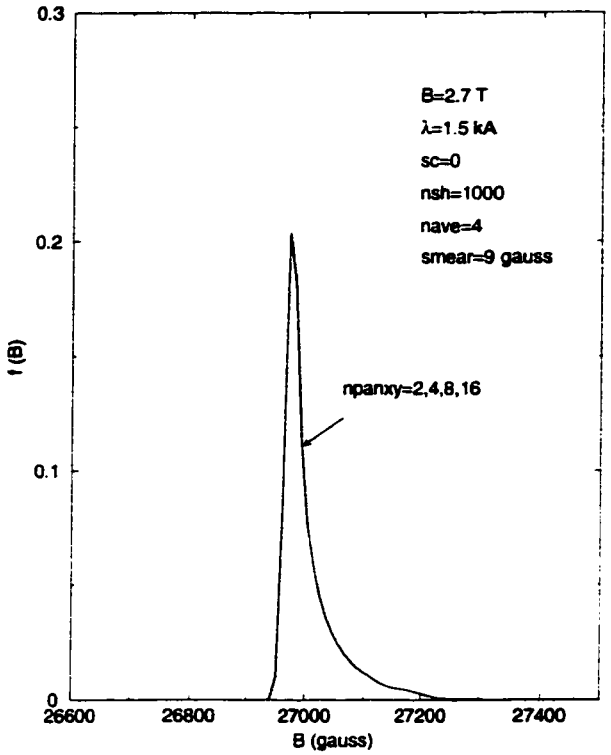

Figure 4.12: This plot shows that in our model the field distribution $f(B)$ is almost independent of parameter *npanxy*. Macroscopically this means that $f(B)$ does not depend on the beam size or sample size.

ρ_{rms} of a 2D pancake vortice is small, the stack of 2D pancake vortices thus withstands thermal agitation, holds itself together and produces a field distribution similar to that of a straight 3D vortex, which is certainly our case when sc is much smaller than the vortex lattice constant a. However as the temperature increases, sc increases, ρ_{rms}^2 will initially be approximately proportional to K_BT, then a divergence of ρ_{rms} occurs at a temperature $T_b = \phi_0^2/16\pi^2 K_B\lambda$, where the thermal energies required to misalign the 2D pancake vortices are $K_BT_b = \phi_0^2/16\pi^2\lambda$, which can strongly disrupt the alignment and break up a straight stack. It is remarkable that this condition for the thermally induced breakup of an isolated stack

of 2D pancake vortices is exactly the same as that for the Kosterlitz-Thouless transition of an isolated superconducting thin film of screening length λ. [Beasley 79] Furthermore, the gradual change of the field profile $f(B)$ as a function of temperature T suggests that there is no phase transition existing in such high magnetic field and this temperature range, which is consistent with the previous conclusion that there is no phase transition above the crossover field B_{cr}.

To see how the fitting program works on our Bi2212 data, we showed one of the results in fig. 4.13. The μSR data we picked here were taken in B=2.7 T and at T= 2 K. From the plot, we can see that the fitting is quite satisfactory, which shows the correctness of our whole fitting scheme. At such low temperature, the model also gives us the rapid relaxation of muon spins, as we expected.

Fig. 4.14 shows the scale factor *sc* dependence of the field lineshape $f(B)$. For a typical field B=2.7 T, the vortex lattice constant is about a=0.3 kÅ. When *sc* is very small, the field profile $f(B)$ is asymmetric and almost independent of *sc*. When *sc* increases to about 0.10 (1/3 of the vortex lattice constant a=0.3 kÅ), the symmetry of $f(B)$ changes suddenly with the disappearance of the high field tail. The corresponding numerical results are shown in fig. 4.17. The same feature appears in different fields, see fig. 4.16 and 4.18.

4.5.5.4 ω_{ave}, ω_{diff} vs. B

To investigate the dependence of ω_{ave} and ω_{diff} on the magnetic field B in our model, we chose a typical set of parameters λ=1.5 kÅ, *sc*=0.2, *nsh*=1000, *npanxy*=4, *nave*=4 and the results ω_{ave}, ω_{diff} vs. B are shown in fig. 4.19. From the plot, ω_{ave} and ω_{diff} seem to have less dependence on B than on the scale factor *sc*. This result excellently explains our

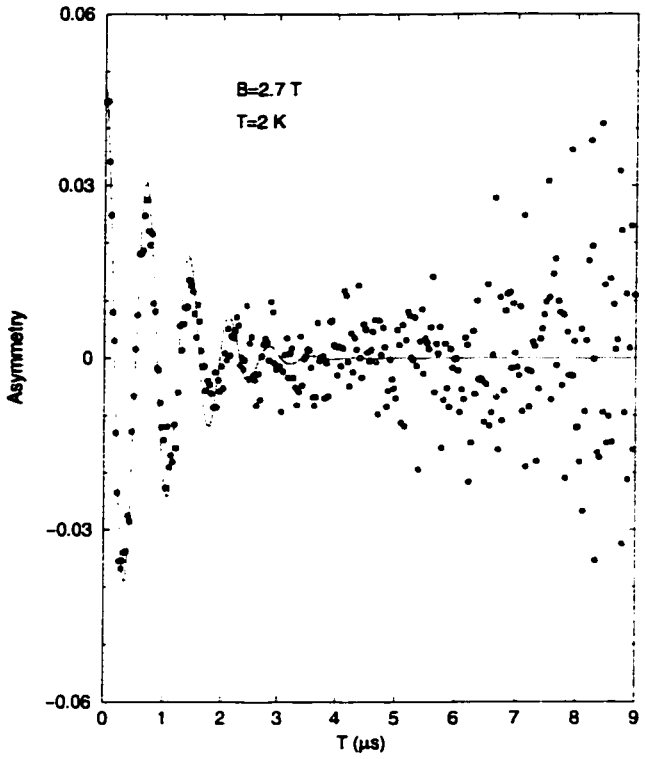

Figure 4.13: A comparison between the model calculation (*sc*=0, *nave*=3, *smear*=9 gauss) and the b.b.g. fit for the experimental data at B=2.7 T and T=2 K.

experimental data on Bi2212 that the muon spin depolarization rates are almost independent of magnetic field B, see fig. 4.5. It is also interesting to note that ω_{ave} does not have a monotonic dependence on B in this model, which explains the behavior of ω_{ave} vs. B in fig. 4.5. In addition, ω_{diff} vs. B shows that for a quite large range of B, ω_{diff} is very small and less than 0.3. This is also consistent with our experimental data.

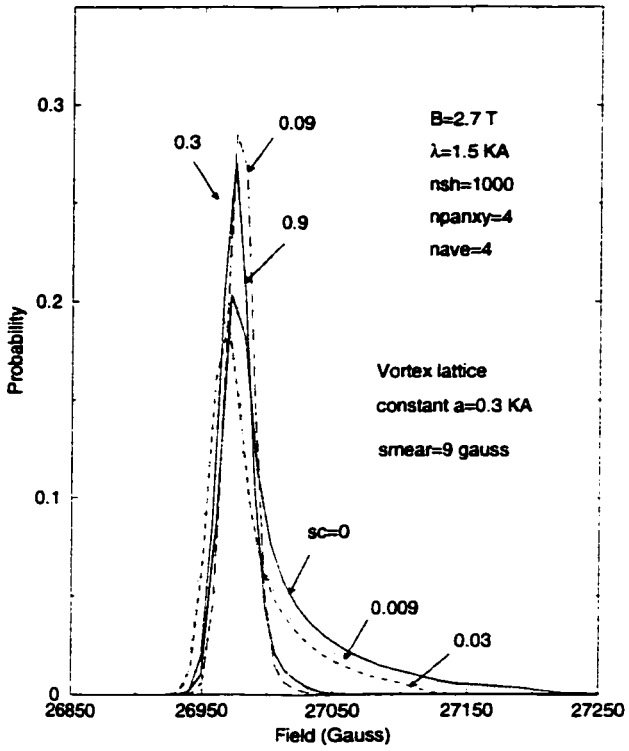

Figure 4.14: Random walk scale factor *sc* dependence of the simulated field profiles.

4.5.5.5 ω_{ave}, ω_{diff} vs. λ

In this section, we are going to see how ω_{ave} and ω_{diff} behave as functions of penetration depth λ. As we know from the fundamental theory in the second chapter, without any vortex disorder the relaxation rate ω_{ave} is approximately proportional to $\frac{1}{\lambda^2}$, so we expect ω_{ave} to decrease with increasing λ. We calculated ω_{ave}, ω_{diff} vs. λ in our model. The results are shown in fig. 4.20. From the figure, we can see that indeed ω_{ave} has a smaller value at bigger penetration depth λ. At fixed λ, ω_{ave} at sc=0 is bigger than at sc=0.2, which is consistent with the results presented in fig. 4.17.

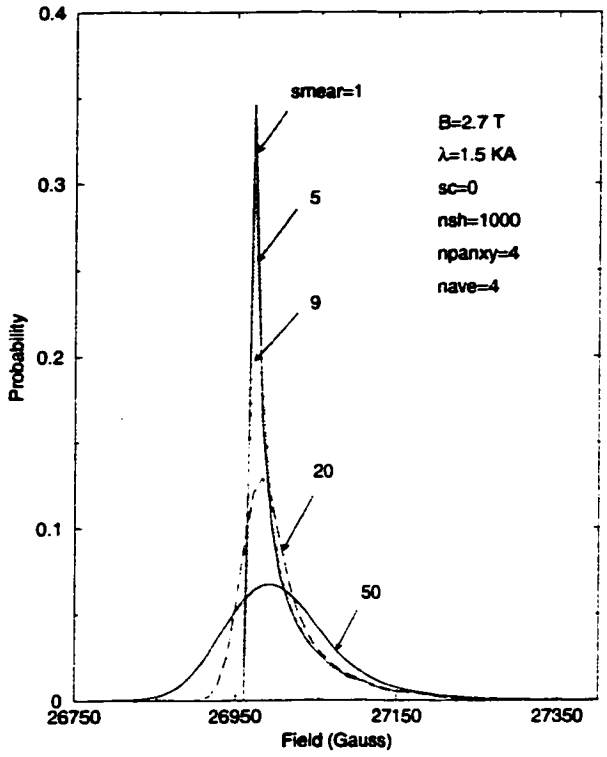

Figure 4.15: Smearing factor (unit: gauss) dependence of the simulated field profiles.

While we increase the values of penetration depth λ, it was found that, with higher disorder, the field lineshape goes from very asymmetric at sc=0 to steadily symmetric at sc=0.2 with a slight tail on the right side of $f(B)$. However at very small penetration depth such as λ=1.0 kÅ, the field profile even appears to have a slight tail on the left side of $f(B)$ (negative ω_{diff}) as modelling results tell us, see fig. 4.20 and fig. 4.21.

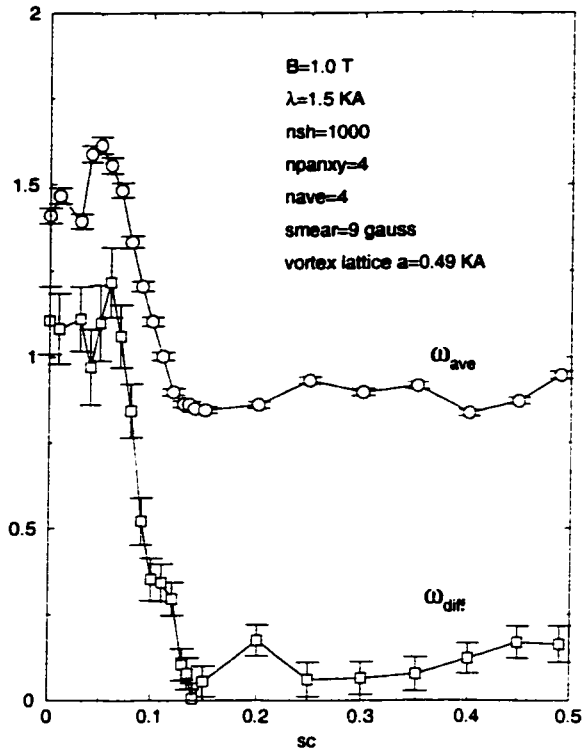

Figure 4.16: Plots of ω_{ave} and ω_{diff} as functions of the pancake disorder scaling factor sc. (B=1.0 T)

4.6 Conclusion

The comparison between our pancake vortex disorder model with the transverse field muon spin relaxation (TF-μSR) data in external magnetic fields 1.0, 2.7, 3.0, 4.5, 5.5, 6.0 and 7.0 T shows excellent agreement. The model recovers all the important features discovered in the experiment. For the first time, a heterodyned fitting analysis technique shows that the field profiles on the *ab* basal planes of single crystal Bi2212 are symmetric in all experimental fields 1.0-7.0 T and at all experimental temperatures 2.0-90.0 K. The muon spin relaxation rates due to the mixed state of Bi2212 were found to increase linearly from 0 μs^{-1} at

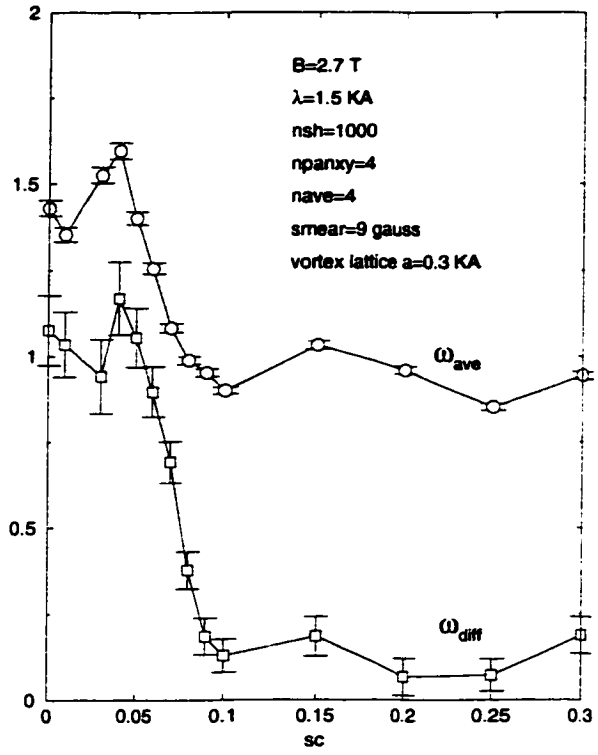

Figure 4.17: Plots of ω_{ave} and ω_{diff} as functions of the pancake disorder scaling factor sc. (B=2.7 T)

transition temperature 90.0 K to about 1.0 μs^{-1} at the lowest temperature 2.0 K. The relaxation rates have much less field dependence than the temperature dependence and the field dependence of the relaxation rate is of opposite sign to that seen for YBCO, which is undoubtedly due to vortex lattice disorder caused by the weak coupling between the CuO planes. The scaled magnetic field penetration depths $\frac{\lambda}{\lambda(0)}$ were found to be independent of magnetic field B at temperature range 0-50.0 K. Fitting $\frac{\lambda}{\lambda(0)}$ by currently available models was attempted. The proposed pancake vortex disorder model strongly suggests pancake disordering at all temperatures including 2.0 K, the lowest temperature reached in

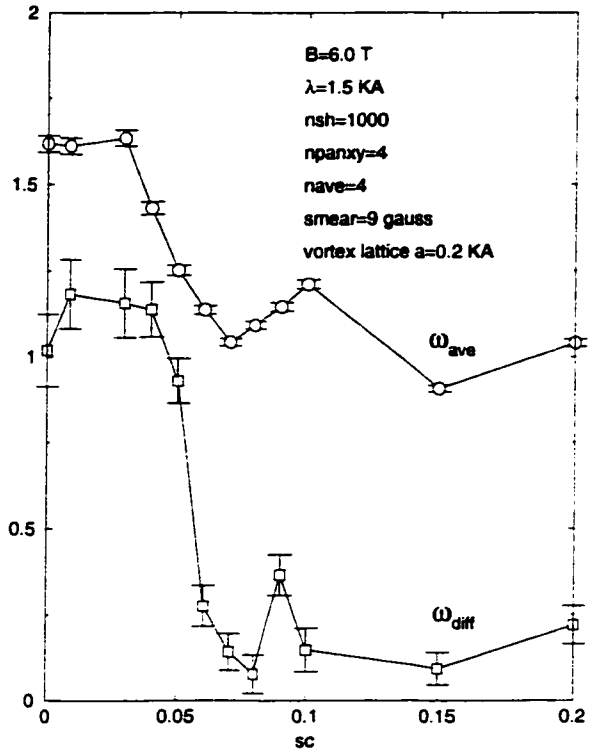

Figure 4.18: Plots of ω_{ave} and ω_{diff} as functions of the pancake disorder scaling factor sc. (B=6.0 T)

our experiment. Our experiments and the computer simulation from the pancake vortex disorder model showed that μSR data at this temperature and field range are attributed to the 2-D anisotropic vortex characteristics of Bi2212.

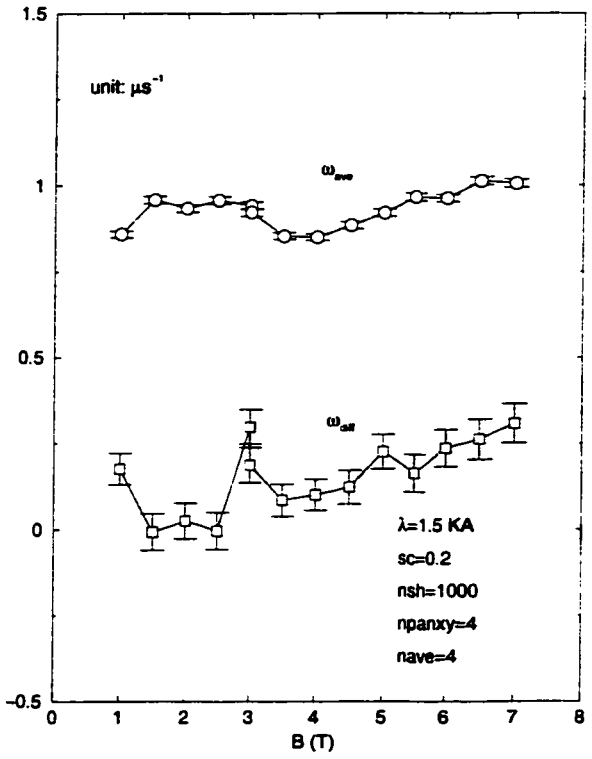

Figure 4.19: Plots of ω_{ave} and ω_{diff} as functions of applied fields.

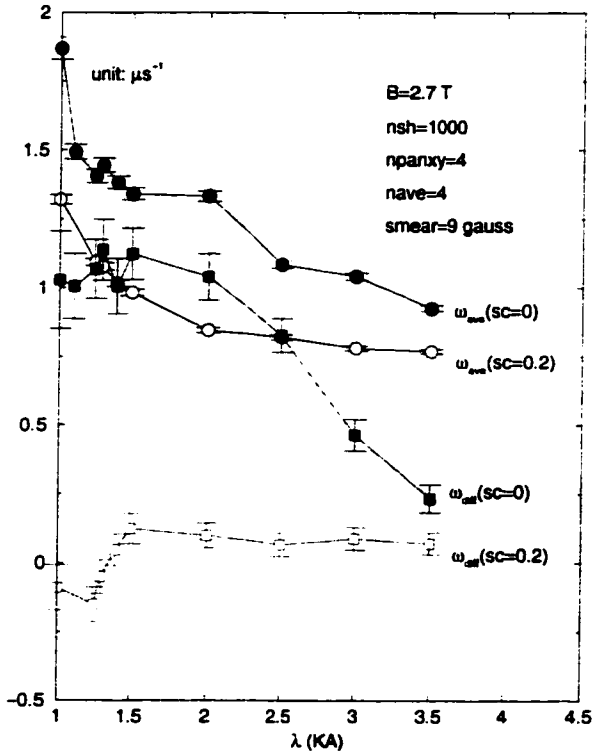

Figure 4.20: Plots of ω_{ave} and ω_{diff} as functions of penetration length λ.

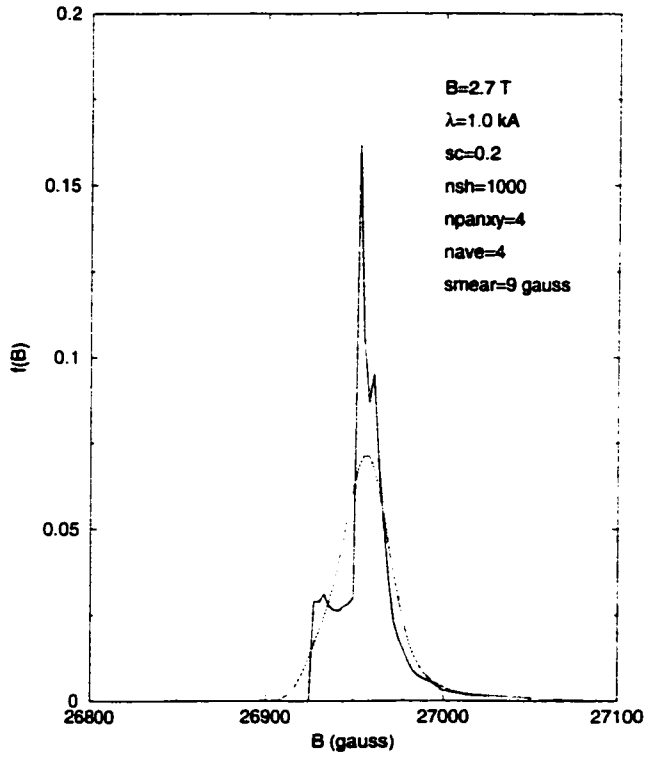

Figure 4.21: In our Bi2212 data, some of the field profiles appear to have a slight tail on the left (low field) side. Our model shows that with the appropriate choice of parameters in our model, the field profile can have a tail on the left, which was considered to be unphysical before.

Appendix A

Pion and Muon Decays

Derivation of linear momentum 29.7 MeV/c and kinetic energy 4.1 MeV of μ^+ from free π^+ decay process:

$$\pi^+ \rightarrow \mu^+ + \nu_\mu \tag{A.1}$$

According to the laws of conservation of energy and linear momentum, we have

$$m_\pi\ c^2 = m_\mu\ c^2 + \frac{p^2}{2m_\mu} + pc \tag{A.2}$$

where p is the linear momentum of muon or muon neutrino. Plug in $m_\pi\ c^2 = 139.5673$ MeV and $m_\mu\ c^2 = 105.67$ MeV into the equation above, we can solve $p = 29.7$ MeV/c and $E_k = \frac{p^2}{2m_\mu} = 4.1$ MeV.

Derivation of the maximum positron kinetic energy 52.325 MeV from surface muon process: (Notice that there are other possible muon decay channels, i. e., $\mu^+ \rightarrow e^+ + \overline{\nu}_\mu + \nu_e + \gamma$ with branching ratio ~ 0.014 and $\mu^+ \rightarrow e^+ + \overline{\nu}_\mu + \nu_e + e^+ + e^-$ with branching ratio $\sim 3 \times 10^{-5}$)

$$\mu^+ \rightarrow e^+ + \nu_e + \overline{\nu}_\mu \tag{A.3}$$

The positive muon decay is a three-body decay. The kinetic energy of the emerging positron may therefore vary continuously between zero and the maximum kinetic energy $E_{k-\max}$.

The total energy is conserved, so we have

$$m_\mu\, c^2 = m_e\, c^2 + E_{k-\max} + E_{\nu_e} + E_{\overline{\nu}_\mu} \tag{A.4}$$

For relativistic positron, we have

$$E_T^2 = (m_e\, c^2 + E_{k-\max})^2 = p^2c^2 + (m_e\, c^2)^2 \tag{A.5}$$

which can be simplified to

$$2\, E_{k-\max}\, m_e\, c^2 + E_{k-\max}^2 = p^2c^2 \tag{A.6}$$

According to the conservation of linear momentum, the positron's momentum p can be written as:

$$p = \frac{E_{\nu_e} + E_{\overline{\nu}_\mu}}{c} \tag{A.7}$$

With all these equations in mind, we know

$$\begin{aligned} m_\mu\, c^2 &= m_e\, c^2 + E_{k-\max} + E_{\nu_e} + E_{\overline{\nu}_\mu} \\ &= m_e\, c^2 + E_{k-\max} + pc \\ &= m_e\, c^2 + E_{k-\max} + \sqrt{2\, E_{k-\max}\, m_e\, c^2 + E_{k-\max}^2} \end{aligned} \tag{A.8}$$

Solving this equation for $E_{k-\max}$, we can get

$$\begin{aligned} E_{k-\max} &= \frac{(m_\mu\, c^2 - m_e\, c^2)^2}{2\, m_\mu\, c^2} \\ &= 52.325 \text{ MeV} \end{aligned} \tag{A.9}$$

$$(m_\mu\, c^2 = 105.67 \text{ MeV},\ m_e\, c^2 = 0.51100 \text{ MeV})$$

Appendix B

Kubo-Toyabe Relaxation Functions

Derivation of the Gaussian static zero-field Kubo-Toyabe relaxation function

$$G_G(t) = \frac{1}{3} + \frac{2}{3}\,(1 - \Delta^2 t^2)\, e^{-\frac{\Delta^2 t^2}{2}} \tag{B.1}$$

from the known formula

$$G_G(t) = \frac{1}{3} + \frac{2}{3} \int_0^\infty P(|\mathbf{B}|) \cos(\gamma_\mu |\mathbf{B}| t)\; d|\mathbf{B}| \tag{B.2}$$

where $P(|\mathbf{B}|) = \sqrt{\frac{2}{\pi}} \frac{|\mathbf{B}|^2}{\Gamma^3}\, e^{-\frac{|\mathbf{B}|^2}{2\,\Gamma^2}}$.

$$\begin{aligned} G_G(t) &= \frac{1}{3} + \frac{2}{3} \int_0^\infty \sqrt{\frac{2}{\pi}} \frac{|\mathbf{B}|^2}{\Gamma^3} e^{-\frac{|\mathbf{B}|^2}{2\,\Gamma^2}} \cos(\gamma_\mu |\mathbf{B}| t)\; d|\mathbf{B}| \\ &= \frac{1}{3} + \frac{8}{3\sqrt{\pi}} \int_0^\infty x^2 e^{-x^2} \cos(\sqrt{2}\gamma_\mu \Gamma t x)\; dx \;\left(\text{ let } x = \frac{|\mathbf{B}|}{\sqrt{2}\Gamma}\right) \\ &= \frac{1}{3} + \frac{8}{3\sqrt{\pi}} \int_0^\infty x^2 e^{-x^2} \cos(bx)\; dx \;(\text{ let } b = \sqrt{2}\gamma_\mu \Gamma t\,) \end{aligned} \tag{B.3}$$

Integrating by parts,

$$\int_0^\infty x^2 e^{-x^2} \cos(bx)\; dx = (\frac{1}{2} - \frac{b^2}{4}) \int_0^\infty e^{-x^2} \cos(bx)\; dx \tag{B.4}$$

Furthermore,

$$\int_0^\infty e^{-x^2} \cos(bx)\; dx = \Re(\frac{1}{2} \int_{-\infty}^\infty e^{-x^2 + ibx}\; dx) \tag{B.5}$$

Note the function e^{-x^2+ibx} is analytic, so we can do a contour integral in the upper half complex plane to solve this integral, and the result is

$$\begin{aligned} \Re\left(\frac{1}{2}\int_{-\infty}^{\infty} e^{-x^2+ibx}\,dx\right) &= \frac{1}{2}\,e^{-\frac{b^2}{4}}\int_{-\infty}^{\infty} e^{-x^2}dx \\ &= \frac{\sqrt{\pi}}{2}\,e^{-\frac{b^2}{4}} \end{aligned} \tag{B.6}$$

Plugging these results back in sequence, finally we get

$$G_G(t) = \frac{1}{3} + \frac{2}{3}\,(1-\Delta^2 t^2)\,e^{-\frac{\Delta^2 t^2}{2}} \;(\text{ where } \Delta = \gamma_\mu \Gamma\;). \tag{B.7}$$

Derivation of the Lorentzian static zero-field Kubo-Toyabe relaxation function

$$G_L(t) = \frac{1}{3} + \frac{2}{3}(1-\lambda t)e^{-\lambda t} \tag{B.8}$$

based on the magnetic field magnitude distribution

$$P(|\mathbf{B}|) = \frac{4}{\pi}\frac{\Gamma\,|\mathbf{B}|^2}{(\Gamma^2+|\mathbf{B}|^2)^2}. \tag{B.9}$$

We know that the following relation between $G_z(t)$ and $P(|\mathbf{B}|)$ exists:

$$\begin{aligned} G_L(t) &= \frac{1}{3} + \frac{2}{3}\int_0^{\infty} P(|\mathbf{B}|)\cos(\gamma_\mu\,|\mathbf{B}|\,t)\;d\,|\mathbf{B}| \qquad (B.10)\\ &= \frac{1}{3} + \frac{8}{3\pi}\int_0^{\infty}\frac{x^2}{(1+x^2)^2}\cos(bx)\;dx \;\left(\text{assume } x = \frac{|\mathbf{B}|}{\Gamma} \text{ and } b = \gamma_\mu \Gamma t\right)\\ &= \frac{1}{3} + \frac{8}{3\pi}\cdot\frac{1}{2}\int_{-\infty}^{\infty}\frac{x^2}{(1+x^2)^2}\cos(bx)\;dx\\ &= \frac{1}{3} + \frac{8}{3\pi}\cdot\frac{1}{2}\int_{-\infty}^{\infty}\frac{x^2}{(1+x^2)^2}[\cos(bx)+i\sin(bx)]\;dx\\ &= \frac{1}{3} + \frac{8}{3\pi}\cdot\frac{1}{2}\oint_c\frac{z^2}{(1+z^2)^2}\,e^{ibz}\;dz \;(c \text{ is a half circle contour in the upper plane})\\ &= \frac{1}{3} + \frac{8}{3\pi}\cdot\frac{\pi}{4}(e^{-b}-be^{-b}) \;(\text{using } \textit{the Residue Theorem})\\ &= \frac{1}{3} + \frac{2}{3}(1-\lambda t)e^{-\lambda t} \;(\text{where } \lambda = \gamma_\mu\Gamma) \end{aligned}$$

It is interesting to note that another way to derive the Lorentzian static zero-field Kubo-Toyabe relaxation function is to convolute the Gaussian static zero-field Kubo-Toyabe relaxation function with "class" of muon site distribution $\rho(\Delta) = \sqrt{\frac{2}{\pi}}\frac{\lambda}{\Delta^2}\, e^{-\frac{\lambda^2}{2\Delta^2}}$, i.e.

$$\begin{aligned} G_L(t) &= \int_0^\infty \rho(\Delta)\, G_G(t) d\Delta & \text{(B.11)} \\ &= \int_0^\infty \sqrt{\frac{2}{\pi}}\frac{\lambda}{\Delta^2} e^{-\frac{\lambda^2}{2\Delta^2}} [\frac{1}{3} + \frac{2}{3}(1-\Delta^2 t^2)\, e^{-\frac{\Delta^2 t^2}{2}}] d\Delta & \text{(B.12)} \\ &= \frac{1}{3} + \frac{2}{3}(1-\lambda t)\, e^{-\lambda t} & \text{(B.13)} \end{aligned}$$

Now we do the integrations in the equation above separately,

$$\begin{aligned} I &= \int_0^\infty \sqrt{\frac{2}{\pi}}\frac{\lambda}{\Delta^2} e^{-\frac{\lambda^2}{2\Delta^2}} \frac{1}{3} d\Delta \text{ (let } x = \frac{1}{\Delta}) \\ &= \int_0^\infty \frac{\lambda}{3}\sqrt{\frac{2}{\pi}} e^{-\frac{\lambda^2 x^2}{2}} dx \\ &= \frac{1}{3} & \text{(B.14)} \end{aligned}$$

$$\begin{aligned} II &= \int_0^\infty \sqrt{\frac{2}{\pi}}\frac{\lambda}{\Delta^2} e^{-\frac{\lambda^2}{2\Delta^2}} \frac{2}{3} e^{-\frac{\Delta^2 t^2}{2}} d\Delta \\ &= \frac{2\lambda}{3}\sqrt{\frac{2}{\pi}} \int_0^\infty e^{-\frac{\lambda^2 x^2}{2} - \frac{t^2}{2x^2}} dx \text{ (let } x = \frac{1}{\Delta}) \\ &= \frac{2}{3}\, e^{-\lambda t} \text{ (integral table: } \int_0^\infty e^{-ax^2 - \frac{b}{x^2}} dx = \frac{1}{2}\sqrt{\frac{\pi}{a}} e^{-2\sqrt{ab}} (a>0, b>0)) & \text{(B.15)} \end{aligned}$$

$$\begin{aligned} III &= \int_0^\infty \sqrt{\frac{2}{\pi}}\frac{\lambda}{\Delta^2} e^{-\frac{\lambda^2}{2\Delta^2}} (-\frac{2}{3}\Delta^2 t^2) e^{-\frac{\Delta^2 t^2}{2}} d\Delta \\ &= -\frac{2\lambda t^2}{3}\sqrt{\frac{2}{\pi}} \int_0^\infty e^{-\frac{\lambda^2}{2\Delta^2} - \frac{\Delta^2 t^2}{2}} d\Delta \text{ (use the same integral table again!)} \\ &= -\frac{2\lambda t}{3} e^{-\lambda t} & \text{(B.16)} \end{aligned}$$

Finally, adding up I, II, III, **we get**

$$\begin{aligned} G_L(t) &= I + II + III \\ &= \frac{1}{3} + \frac{2}{3}(1 - \lambda t)\, e^{-\lambda t}. \end{aligned} \tag{B.17}$$

Appendix C

Review of Research on Bi-2212

Chemical compositions	Comments	References
Layered superconductors	Lawrence-Doniach (LD) model and its basic features	[Lawrence 70, Klemm 75]
Isotropic SC (ISC)	Analytical GL expression for magnetic field distribution	[Clem 75]
HTSC	Theoretical magnetic field distribution	[Barford 88]
Bi2212	Rutherford Backscattering (RBS) studies	[Liu 88]
Anisotropic SC (ASC)	Measurements of anisotropy γ	[Farrell 88, Welp 89, Dolan 89]
BSCCO	NQR and NMR characterization	[Guid 89]
Bi2212	Production method of Bi2212 powder	[Bunker 88, Balachandran 89]
Bi2212	STM measurement	[Ramos 89]
Bi2212	Low field DC magnetization	[Shaw 89]
$Bi_2Sr_{1.25}Ca_{1.75}Cu_2O_x$	Magnetic penetration depth	[Ansaldo 89A]
Uniaxially ASC	Magnetic field **B** and anisotropic mass ratio M_z/M dependent distorted triangular lattice	[Campbell 88, Petzinger 90]
Bi2212	Studies of Fermi surface	[Massida 88, Krakauer 88, Ding 96A, 97, Saini 97]
HTSC	Vortex pinning	[Brandt 88, 88A, 91]
Bi2212	Magnetization $M(T, H)$ measurement	[Kes 91]
$Bi_{2.1}Sr_{1.9}Ca_{0.9}Cu_2O_x$	Study of VL by the high-Q mechanical-oscillator technique	[Duran 91]
$Bi_2Sr_2CaCu_2O_x$	Penetration depth measurement by the rf-resonance method	[Maeda 92]
ASC	Proposing quasi-2D vortices ("pancake" vortices)	[Clem 91]
HTSC	Field distribution of triangular flux-line lattice (FLL) with disorder and anisotropy effects	[Brandt 88A, Pümpin 90, Riseman 95]
Bi2212	Travelling solvent floating zone method growing single crystal	[Motohira 89, Gu 93, Li 94]
BSCCO	Thin film fabricated by the pulsed laser deposition (PLD) method	[Ranno 93]
BSCCO	Growth of single crystal	[Yang 93A]
Bi2212	Studies of Bi2212 crystal structure	[Kan 90, 92, Petricek 90, Gao 93, Yang 93, 96]
Layered HTSC	Phase diagram of extremely type-II layered superconductors	[Hetzel 92, Li 93, Koshelev 96, Rodriguez 97]
Uniaxially ASC	Interpenetrating flux-line lattices	[Sudbø 93]
Bi2212	Growth of Bi2212 single crystals using self-flux method	[Davydov 93]
Bi2212(thin film)	(H, T) phase diagram	[Harada 93, Zeldov 95]

$Bi_2Sr_2CaCu_2O_{8+\delta}$	Mixed s- and d-wave ($s + e^{i\theta}d$) symmetry is applicable	[Chaudhari 94]
Bi2212	Extremely type-II layered superconductor	[Tinkham 94]
Bi2212	Vortex decoupling crossover	[Hellerqvist 94]
BSCCO	Phase diagram	[Blatter 94, Idemoto 94]
Bi2212	Specific heat up to 14 T and magnetization	[Junod 94]
BSCCO	BSCCO is intrinsically a stack of Josephson junctions	[Kleiner 94]
Doped Bi2212	Chain state was found to be embedded in the lattice by Bitter pattern experiment	[Bolle 91, Grigorieva 95]
HTSC	Glassy or liquid states of vortex	[Blatter 94, Brandt 95]
Bi2212	Finite and highly anisotropic superconducting gap on the whole Fermi surface	[Ichimura 95]
$Bi_{2.15}Sr_{1.85}CaCu_2O_{8+\delta}$	Transition from continuous 3D vortex lines to 2D vortex pancakes	[Lee 95]
HTSC	Complicated lattice structure with extended and/or mixed symmetry of the order parameter	[Scalapino 95, Ding 96, Levi 96]
Bi2212	Linear temperature dependence in σ suggests nodes in the superconducting gap	[Jacobs 95, Lee 96]
HTSC	The role of crystal structure symmetry upon the OP components	[Annett 96]
Bi2212	Observing the vortex structure at low field with the aid of the decoration technique	[Vinnikov 96]
Bi2212	Temperature and doping dependence of λ	[Waldmann 96]
Bi2212	Study of the quasiparticle c-axis transport supports the d-wave pairing scenario	[Tanabe 96]
BSCCO	Density-functional theory of flux-line lattice melting	[Menon 96]
$Bi_2Sr_2CaCu_2O_{8+\delta}$	Anisotropy of the superconducting gap	[Kendziora 95, 96, Kelley 96]
$Bi_2Sr_2CaCu_2O_{8+\delta}$	Pseudogap behavior studied by ARPES	[Ding 96, Loeser 96, Harris 96]
ASC	Theoretical studies of instabilities in the flux-line lattice	[Thompson 97]
HTSC	Effect of vortex core on the magnetic field distribution	[Yaouanc 97A]
BSCCO	Thin film synthesized by co-sputtering-deposition technique	[Ota 97]
Bi2212	Small s-wave Order Parameter (OP) component at low T through c-axis Josephson tunneling	[Kleiner 97]
Bi2212	Field dependent thermal conductivity $\kappa(H)$ in the mixed state of Bi2212	[Krishana 97, Aubin 98]
HTSC	Estimation of penetration length λ from the second moment of field distribution ΔB	[Hao 1991, Sonier 94, Yaouanc 97]
Bi2212	$I(V)$ and $dI/dV(V)$ tunneling characteristics	[Tao 97, Renner 98, DeWide 98]
$Bi_2Sr_2CaCu_2O_{8+\delta}$	Weak temperature dependence of the superconducting gap	[Misochko 98]
$Bi_2Sr_2CaCu_2O_{8+\delta}$	Spin correlation and pseudogap behavior probed by Cu NMR	[Ishida 96, 98]

HTSC	"Vortex matter" phases due to thermal fluctuation, dimensional crossover and pinning	[Fuchs 98]
$Bi_{2.15}Sr_{1.85}CaCu_2O_{8+\delta}$	Angular dependence of disorder crossover	[Aegerter 98]
Doped Bi2212	Effects of doping on phonon Raman scattering	[Chen 98]
$Bi_2Sr_2CaCu_2O_{8+\delta}$	Imaging of atomic planes by high resolution STM	[Pan 98]
BSCCO	Large vortex contribution to the complex conductivity in the regime of high H and low T	[Mallozzi 98]
Bi2212	Pseudogap is observed	[Corson 99, Castellani 99]
Bi2212	Pseudogap is observed by SIN and SIS tunneling techniques	[Matsuda 99, Ekino 99]
$Bi_2Sr_2CaCu_2O_{8+\delta}$	Two-stage melting transition	[Blasius 99]
BSCCO	Order-parameter(OP) symmetry	[Shen 93, Kirtley 96, Tsui 97, Klemm 00]
$Bi_2Sr_2CaCu_2O_{8+\delta}$	Quasiparticles in the SC state by ARPES	[Kaminski 00]
Bi2212	Electronlike Fermi surface by ARPES	[Zakharov 00]
Bi2212	Low temperature vortex structure of the mixed state	[Blasius 00]
Bi2212	Intrinsic Tunneling Spectroscopy Studies of SC Gap and Pseudogap	[Krasnov 01, 02]
Bi2212	Growth of Bi2212 single-crystal whiskers	[Nagao 01]
Bi2212	Flux Dynamics of Paramagnetic Meissner State	[Papadopoulou 02]

Bibliography

[Abrikosov 57] Abrikosov A A, Sov. Phys. JETP **10** (1957) 1174.

[Aegerter 96, 98] Aegerter C M *et al.*, Phys. Rev. B **54** (1996) R15661; Phys. Rev. B **57** (1998) 1253.

[Aeppli 87] Aeppli G *et al.*, Phys. Rev. B **35** (1987) 7129.

[Alff 98] Alff L *et al.*, cond-mat/9806150.

[Amin 00] Amin M H S *et al.*, Phys. Rev. Lett. **84** (2000) 5864.

[Annett 91, 96, 99] Annett J *et al.*, Phys. Rev. B **43** (1991) 2778; Annett J, Goldenfeld N, and Leggett A J, in Ginsberg D M (ed.), *Physical Properties of High Temperature Superconductors V* (World Scientific, Singapore, 1996), p.375-461; Physica C **317-318** (1999) 1.

[Ansaldo 89, 89A, 91] Ansaldo E J *et al.*, Physica C **162-164** (1989) 2317; Physica C **162-164** (1989) 259; *Workshop on Electronic Structure and Mechanisms for High Temperature Superconductivity, University of Miami* (3-9 January 1991).

[Appel 90] Appel J and Fay D, Phys. Rev. B **41** (1990) 873.

[Arberg 93] Arberg P *et al.*, Solid State Commun. **86** (1993) 671.

[Aubin 98] Aubin H *et al.*, Science **280** (1998) 9a.

[Balachandran 89] Balachandran U *et al.*, Materials Lett. (1989) 454.

[Barford 88] Barford W and Gunn J M F, Physica C **156** (1988) 515.

[Beasley 79] [Beasley 79] Beasley M R *et al.*, Phys. Rev. Lett. **42** (1979) 1165.

[Berlinsky 95] Berlinsky A J *et al.*, Phys. Rev. Lett. **75** (1995) 2200.

[Bernhard 95] Bernhard C *et al.*, Phys. Rev. B **52** (1995) 10488 and R7050.

[Blasius 99, 00] Blasius T *et al.*, Phys. Rev. Lett. **82** (1999) 4926; Physica B **289-290** (2000) 365.

[Blatter 94, 96, 97] Blatter G *et al.*, Rev. Mod. Phys. **66** (1994) 1125; Phys. Rev. B **54** (1996) 72; Physica C **282-287** (1997) 19.

[Bolle 91] Bolle C A *et al.*, Phys. Rev. Lett. **66** (1991) 112.

[Bourdillon 94] Bourdillon A and Bourdillon N X Tan, *High Temperature Superconductors: Processing and Science* (Academic Press, London, 1994) p. 21.

[Brandt 88, 88A, 91, 95] Brandt E H, J. Low Temp. Phys. **73** (1988) 355; Phys. Rev. B **37** (1988) 2349; Phys. Rev. Lett. **66** (1991) 3213; Rep. Prog. Phys. **58** (1995) 1465.

[Brewer 90, 94] Brewer J H *et al.*, Hyp. Int. **63** (1990) 177; *Encyclopedia of Applied Physics*, v. 11 (VCH Publishers, 1994), p. 23.

[Buckel 91] Buckel W, *Superconductivity: Fundamentals and Applications* (VCH, Germany, 1991).

[Bulaevskii 92] Bulaevskii L N *et al.*, Phys. Rev. B **46** (1992) 366, 11807.

[Bunker 88] Bunker B C *et al.*, *High Temp. Superconducting Materials: Preparation, Properties and Processing*, Ed. Hatfield W E, Miller J H, Marcel Dekker, Inc. NY (1988).

[Busch 92] Busch R *et al.*, Phys. Rev. Lett. **69** (1992) 522.

[Caillol 82] Caillol J M *et al.*, J. Stat. Phys. **28** (1982) 325.

[Campbell 88] Campbell L J *et al.*, Phys. Rev. B **38** (1988) 2439.

[Caroli 64] Caroli C *et al.*, Phys. Lett. **9** (1964) 307.

[Castellani 99] Castellani C and Castro C Di, Physica A **263** (1999) 197.

[Chappert and Grynszpan 84] Chappert J and Grynszpan R I, *Muon and Pions in Materials Research* (Amsterdam: North-Holland, 1984).

[Chappert and Yaouanc 86] Chappert J and Yaouanc A, *Microscopic Methods in Metals (Springer Topics in Current Physics 40)* (Berlin: Springer), p. 297.

[Chaudhari 94] Chaudhari P and Lin S Y, Phys. Rev. Lett. **72** (1994) 1084.

[Chen 98] Chen X H *et al.*, Phys. Rev. B **58** (1998) 5868.

[Cho 94] Cho J H *et al.*, Phys. Rev. B **50** (1994) 6493.

[Choi 97] Choi M S and Lee S I, J. Phys.: Condens. Matter **9** (1997) 211 and references therein.

[Clem 75, 91] Clem J R, J. Low Temp. Phys. **18** (1975) 427; Phys. Rev. B **43** (1991) 7837.

[Corson 99] Corson J *et al.*, Nature **398** (1999) 221.

[Cox 87] Cox S F J, J. Phys. C: Solid State Phys. **20** (1987) 3187.

[Cubitt 93] Cubitt R *et al.*, Nature **365** (1993) 407.

[Daemen 93, 93A] Daemen L L *et al.*, Phys. Rev. Lett. **70** (1993) 1167; Phys. Rev. B **47** (1993) 11291.

[Dahl 92] Dahl P F, *Superconductivity: Its Historical Roots and Development from Mercury to the Ceramic Oxides* (AIP, 1992).

[Dalmas 97] Dalmas P and Yaouanc A, J. Phys.: Condens. Matter **9** (1997) 9113.

[Datta 92] Datta T, *Concise Encyclopedia of Magnetic and Superconducting Materials*, ed. J. Evetts (Pergamon, Oxford, 1992) p.408.

[Davoudi 01] Davoudi B. *et al.*, Physica C **351** (2001) 169.

[Davydov 93] Davydov D N *et al.*, Solid State Commun. **86** (1993) 267.

[De Gennes 66, 89] De Gennes P G, *Superconductivity of Metals and Alloys* (Benjamin W A, New York 1966; Addison Wesley, New York 1989).

[DeWide 98] DeWide Y *et al.*, Phys. Rev. Lett. **80** (1998) 153.

[Ding 96, 96A, 97] Ding H, Nature **382** (1996) 51; Phys. Rev. Lett. **76** (1996) 1533; Phys. Rev. Lett. **78** (1997) 2628.

[Dodgson 98] Dodgson M J W *et al.*, Phys. Rev. B **57** (1998) 14498.

[Dolan 89] Dolan G J *et al.*, Phys. Rev. Lett. **32** (1989) 2184.

[Duran 91] Duran C *et al.*, Phys. Rev. B **44** (1991) 7737.

[Ekino 99] Ekino T *et al.*, Phys. Rev. B **60** (1999) 6916.

[Emery 95] Emery V J and Kivelson S, Nature (London) **374** (1995) 434.

[Farrell 88, 89] Farrell D E *et al.*, Phys. Rev. Lett. **61** (1988) 2805; **63** (1989) 782.

[Feigel'man 90] Feigel'man M V *et al.*, Physica C **167** (1990) 177.

[Fisher 91] Fisher D S *et al.*, Phys. Rev. B **43** (1991) 130.

[Forgan 97] Forgan E M *et al.*, Hyp. Int. **105** (1997) 61.

[Franz 96, 97] Franz M *et al.*, Phys. Rev. B **53** (1996) 5795; Phys. Rev. Lett. **79** (1997) 1555.

[Fuchs 98] Fuchs D T *et al.*, Phys. Rev. Lett. **80** (1998) 4971.

[Gao 93] Gao Y *et al.*, Acta Cryst. A **49** (1993) 141.

[Gingras 96] Gingras M J P and Huse D A, Phys. Rev. B **53** (1996) 15193.

[Glazman 91] Glazman L I and Koshelev A E, Phys. Rev. B **43** (1991) 2835.

[Gorter 34] Gorter C J and Casimir H B G, Physica **1** (1934) 306; Phys. Z. **35** (1934) 963.

[Greer 95] Greer A J and Kossler W J, *Low Magnetic Fields in Anisotropic Superconductors, Lecture Notes in Physics* (Springer, Berlin, 1995)

[Grigorieva 95] Grigorieva I V *et al.*, Phys. Rev. B **51** (1995) 3765.

[Gross 86] Gross F *et al.*, Z. Phys. B: Condens. Matter **64** (1986) 175.

[Gu 93] Gu G D *et al.*, J. Cryst. Growth **130** (1993) 325.

[Guid 89] Guid G *et al.*, Physica C **162-164** (1989) 189.

[Guillot 89] Guillot M *et al.*, Physica C **162-164** (1989) 361.

[Hao 91] Hao Z. *et al.*, Phys. Rev. B **43** (1991) 2844.

[Harada 93] Harada K *et al.*, Phys. Rev. Lett. **71** (1993) 3371.

[Hardy 93] Hardy W N *et al.*, Phys. Rev. Lett. **70** (1993) 3999.

[Harlingen 95] Harlingen V D J, Rev. Mod. Phys. **67** (1995) 515 and references therein.

[Harris 96] Harris J M *et al.*, Phys. Rev. B **54** (1996) R15665.

[Harshman 87, 89, 91, 93, 94] Harshman D R *et al.*, Phys. Rev. B **36** (1987) 2386; Phys. Rev. B **39** (1989) 851; Phys. Rev. Lett. **67** (1991) 3152; Phys. Rev. B **47** (1993) 2905; Phys. Rev. B **49** (1994) 12990.

[Hartmann 93] Hartmann U *et al.*, SPIE Conf. Proc. **140** (1993) 1855.

[Hellerqvist 94] Hellerqvist M C *et al.*, Physica C **230** (1994) 170.

[Herlach 90] Herlach D *et al.*, Hyperfine Interactions **63** (1990) 509.

[Hetzel 92] Hetzel R E *et al.*, Phys. Rev. Lett. **69** (1992) 518.

[Hikami 80] Hikami S and Tsuneto T, Prog. Theor. Phys. **63** (1980) 387.

[Hirschfeld 93] Hirschfeld P J and Goldenfeld N, Phys. Rev. B **48** (1993) 4219.

[Houghton 89, 90] Houghton A *et al.*, Phys. Rev. B **40** (1989) 6763; **42** (1990) 906.

[Huebener 79] Huebener R P, *Magnetic Flux Structures in Superconductors* (Springer-Verlag, Berlin 1979).

[Ichimura 95] Ichimura K *et al.*, J. Phys.: Condens. Matter **7** No 42 (1995) L545.

[Idemoto 94] Idemoto Y *et al.*, Physica C **229** (1994) 47.

[Ishida 96, 98] Ishida K *et al.*, Physica C **263** (1996) 371; Phys. Rev.B **58** (1998) R5960.

[Inui 93] Inui M *et al.*, Phys. Rev. B **47** (1993) 12205.

[Ito 81] to M, Prog. Theor. Phys. **66** (1981) 1129.

[Ivlev 91] Ivlev B I *et al.*, Europhys. Lett. **15** (1991) 349.

[Jacobs 95] Jacobs T *et al.*, Phys. Rev. Lett. **75** (1995) 4516.

[Jihong 88] Jihong W *et al.*, Supercond. Sci. Technol. **1** (1988) 27.

[Junod 94] Junod A *et al.*, Physica C **229** (1994) 209.

[Kaminski 00] Kaminski A *et al.*, Phys. Rev. Lett. **84** (2000) 1788.

[Kan 90, 92] Kan X B *et al.*, J. Mater. Res. **5** (1990) 731; Acta Cryst. B **48** (1992) 122.

[Karlsson 95] Karlsson E B, *Solid State Phenomena as seen by Muons, Protons and Excited Nuclei* (Clarendon, Oxford, 1995).

[Keller 94] Keller H, *Materials and Crystallographic Aspects of HT_c–Superconductivity*, edited by E. Kaldis (Kluwer Academic Publishers, Dordrecht, 1994), p. 265; Aegerter C M and Lee S L, Appl. Magn. Reson. **13** (1997) 75.

[Kelley 96] Kelley R J *et al.*, Science **271** (1996) 1255.

[Kendziora 95] Kendziora C and Rosenberg A, Phys. Rev. B **52** (1995) R9867; Phys. Rev. Lett. **77** (1996) 727.

[Kes 91] Kes P H *et al.*, Phys. Rev. Lett. **67** (1991) 2383.

[Ketterson 99] Ketterson J B and Song S N, *Superconductivity*, United Kingdom: Cambridge University Press (1999) p.119.

[Kirtley 96] Kirtley J R *et al.*, Phys. Rev. Lett. **76** (1996) 1336.

[Kleiner 92, 94, 97] Kleiner R *et al.*, Phys. Rev. Lett. **68** (1992) 2394; Phys. Rev. B **49** (1994) 1327; Physica C **282-287**(1997) 2435.

[Klemm 75, 00] Klemm R A *et al.*, Phys. Rev. B **12** (1975) 877; **61** (2000) 5913.

[Kogan 81] Kogan V G and Clem J R, Phys. Rev. B **24** (1981) 2497.

[Koshelev 96, 97] Koshelev A E, Phys. Rev. Lett. **77** (1996) 3901; Phys. Rev. B **53** (1996) 2786; Phys. Rev. B **56** (1997) 11201.

[Kossler 85, 87, 98, 00, 02] Kossler W J *et al.*, Phys. Rev. B **32** (1985) 293; Phys. Rev. B **35** (1987) 7133; Phys. Rev. Lett. **80** (1998) 592; unpublished (2000); *Proceedings of 9th International Conference on Muon Spin Rotation, Relaxation and Resonance*, June 3-7, Williamsburg, Virginia, USA.

[Kosterlitz 73] Kosterlitz J M and Thouless D J, J. Phys. C **6** (1973) 1181; Kosterlitz J M, J. Phys. C **5** (1974) 1046.

[Krakauer 88] Krakauer H and Pickett W E, Phys. Rev. Lett. **60** (1988) 1665.

[Krasnov 01, 02] Krasnov V M *et al.*, Phys. Rev. Lett. **86** (2001) 2657; Phys. Rev. B **65** (2002) 140504.

[Krishana 97] Krishana K *et al.*, Science **277** (1997) 83.

[Landau 37] Landau L D, Phys. Z. Sowiet **11** (1937) 26.

[Lawrence 70] Lawrence W E and Doniach S, in *Proceedings of the Twelfth Conference on Low Temperature Physics, Kyoto, 1970*, edited by Kanda E (Keigaku, Tokyo, 1970), p. 361.

[Lee 93, 95, 97] Lee S L *et al.*, Phys. Rev. Lett. **71** (1993) 3862; Phys. Rev. Lett. **75** (1995) 922; Phys. Rev. B **55** (1997) 5666.

[Lee 96] Lee S F *et al.*, Phys. Rev. Lett. **77** (1996) 735.

[Levi 96] Levi B G, Phys. Today, **49** (1996) 19.

[Lewis 56] Lewis H W, Phys. Rev. **102** (1956) 1508.

[Li 94] Li T W *et al.*, J. Cryst. Growth **135** (1994) 481.

[Li 91, 93, 94] Li Y H and Teitel S, Phys. Rev. Lett. **66** (1991) 3301; Phys. Rev. B **47** (1993) 359; *ibid* **49** (1994) 4136.

[Liu 88] Liu J Z *et al.*, Phys. Lett. **127** (1988) 444.

[Loeser 96] Loeser A G *et al.*, Science **273** (1996) 325.

[Luke 00] Luke G M *et al.*, Physica B **289-290** (2000) 373.

[Maeda 92] Maeda A *et al.*, Phys. Rev. B **46** (1992) 14234.

[Mallozzi 98] Mallozzi *et al.*, Phys. Rev. Lett. **81** (1998) 1485.

[Martin 88, 89] Martin S *et al.*, Phys. Rev. Lett. **60** (1988) 2194; Appl. Phys. Lett. **54** (1989) 72.

[Martoff 81] Martoff C J and Rosenblum S S, Hyp. Int. **8** (1981) 805.

[Massida 88] Massida S it et al., Physica (Amsterdam) **152C** (1988) 251.

[Matsuda 99] Matsuda A *et al.*, Phys. Rev. B **60** (1999) 1377.

[Menon 96] Menon *et al.*, Phys. Rev. B **54** (1996) 16192.

[Michel 87] Michel C *et al.*, Z. Phys. B **68** (1987) 421.

[Misochko 98] Misochko O V, Phys. of the Solid State **40** (1998) 914.

[Motohira 89] Motohira N *et al.*, J. Ceram. Soc. Japan **97** (1989) 994.

[Mourachkine 99] Mourachkine A, Physica C **323** (1999) 137.

[Mühlschlegel 59] Mühlschlegel B, Z. Phys. **155** (1959) 313.

[Murata 87] Murata K *et al.*, Jpn. J. Appl. Phys. **26** (1987) L473.

[Nagao 01] Nagao M it et al., Appl. Phys. Lett. bf 79 (2001) 2612.

[Naughton 88] Naughton M J *et al.*, Phys. Rev. B **38** (1988) 9280.

[Nelson 88] Nelson D R, Phys. Rev. Lett. **60** (1988) 1973.

[Ota 97] Ota H *et al.*, Appl. Phys. Lett. **70** (1997) 1471.

[Palstra 88] Palstra T T M *et al.*, Phys. Rev. B **38** (1988) 5102.

[Pan 98] Pan S H *et al.*, Appl. Phys. Lett. **73** (1998) 58.

[Papadopoulou 02] Papadopoulou E L *et al.*, Phys. Rev. B **65** (2002) 144524.

[Pastoriza 94] Pastoriza H *et al.*, Phys. Rev. Lett. **72** (1994) 2951.

[Petricek 90] Petricek V *et al.*, Phys. Rev. B **42** (1990) 387.

[Petzinger 90] Petzinger K G and Warren G A, Phys. Rev. B **42** (1990) 2023.

[Pint 89] Pint W *et al.*, Physica C **162-164** (1989) 801.

[Pippard 53] Pippard A B, Proc. Roy. Soc. **A216** (1953) 547.

[Poole 00] Poole C P, *Handbook of Superconductivity* (Academic Press, London, 2000).

[Proc 96] Proc. μSR'96: Hyp. Int. **104,105,106** (1997).

[Pümpin 89, 90] Pümpin B *et al.*, Physica C **162-164** (1989) 151; Phys. Rev. B **42** (1990) 8019.

[Ramos 89] Ramos M A and Vieira S, Physica C **162-164** (1989) 1045.

[Ranno 93] Ranno L *et al.*, Phys. Rev. B **48** (1993) 13945.

[Renner 98] Renner Ch *et al.*, Phys. Rev. Lett. **80** (1998) 149.

[Riseman 94, 95] Riseman T M and Brewer J H, Hyperfine Interactions **86** (1994) 597; Riseman T M *et al.*, Phys. Rev. B **52** (1995) 10569.

[Roddick 95] Roddick E and Stroud D, Phys. Rev. Lett. **74** (1995) 1430.

[Rodriguez 97] Rodriguez J P, J. Phys. Cond. Matter **9** (1997) 5117.

[Ruggeri 76] Ruggeri G J and Thouless D J, J. Phys. F **6** (1976) 2063.

[Ryu 96] Ryu S *et al.*, Phys. Rev. Lett. **77** (1996) 2300; Ryu S and Stroud D, Phys. Rev. B **54** (1996) 1320.

[Safar 92] Safar H *et al.*, Phys. Rev. B **44** (1992) 7737.

[Saini 97] Saini N L *et al.*, Phys. Rev. Lett. **79** (1997) 3467.

[Scalapino 95] Scalapino D J , Phys. Rep. **250** (1995) 329.

[Schatz and Weidinger 95] Schatz G and Weidinger A, *Nuclear Condensed Matter Physics* (Chichester: Wiley, 1995).

[Schenck 85] Schenck A, *Muon Spin Rotation Spectroscopy* (Bristol: Hilger, 1985).

[Schenck and Gygax 95] Schenck A and Gygax F N in Buschow K H J (ed.), *Handbook on Magnetic Materials*, v. 9 (Elsevier, Amsterdam, 1995), p. 57.

[Schneider 95] Schneider J W *et al.*, Phys. Rev. B **52** (1995) 3790.

[Schneider 99] Schneider T and Singer J M, Physica C **313** (1999) 188.

[Schrieffer 88] Schrieffer J R, *Theory of Superconductivity* (Addison-Wesley, 1988) p.9.

[Seeger 78] Seeger A *et al.*, *Hydrogen in Metals (Springer Topics in Current Physics 28)* (Berlin: Springer, 1978), p. 349.

[Shaw 89] Shaw G *et al.*, Physica C **162-164** (1989) 341.

[Shen 93] Shen Z X *et al.*, Phys. Rev. Lett. **70** (1993) 1553.

[Shrivastava 96] Shrivastava K N, *Superconductivity: Theoretical and Experimental Effects* (Nova Science Publishers, 1996) p.282.

[Sigrist 87, 91] Sigrist M and Rice T M, Z. Phys. B **68** (1987) 9; Sigrist M and Ueda K, Rev. Mod. Phys. **63** (1991) 239.

[Soininen 94] Soininen *et al.*, Phys. Rev. B **50** (1994) 13883.

[Sonier 94, 97, 97A, 00, 00A] Sonier J E *et al.*, Phys. Rev. Lett. **72** (1994) 744; **79** (1997) 2875; Phys. Rev. B **55** (1997) 11789; Phys. Rev. B **61** (2000) 3890; Rev. of Mod. Phys. **72** (2000) 769.

[Sudbø 93] Sudbø A *et al.*, Phys. Rev. Lett. **71** (1993) 1451.

[Sunshine 88] Sunshine S A *et al.*, Phys. Rev. B **38** (1988) 893.

[Tanabe 96] Tanabe *et al.*, Phys. Rev. B **53** (1996) 9348.

[Tao 97] Tao H J *et al.*, Physica C **282-287** (1997) 1507.

[Thompson 97] Thompson A M and Moore M A, Phys. Rev. B **55** (1997) 3856.

[Tinkham 75, 94] Tinkham M, *Introduction to Superconductivity* (McGraw-Hill, New York, 1975); Physica C **235** (1994) 3.

[Tsuei 97] Tsuei C C and Kirtley J R, Physica C **282** (1997) 4.

[Tsuneto 98] Tsuneto T, ***Superconductivity and Superfluidity*** (Cambridge University Press, 1998) p.174.

[Uemura 80, 89, 91] Uemura Y J *et al.*, Phys. Rev. Lett. **45** (1980) 583; Phys. Rev. Lett. **62** (1989) 2317; **66** (1991) 2665.

[Umezawa 88] Umezawa A *et al.*, Physica C **153-155** (1988) 1461.

[Vinnikov 96] Vinnikov L Ya *et al.*, JETP Lett. Vol **63**, No. 5 (1996) 370.

[Vinokur 90] Vinokur V M *et al.*, Physica C **168** (1990) 29.

[Waldmann 96] Waldmann O *et al.*, Phys. Rev. B **53** (1996) 11825.

[Wan 99, 99A] Wan X, unpublished (1999); Wan X *et al.*, Hyp. Int. **122** (1999) 233.

[Wördenweber 99] Wördenweber R, Rep. Prog. Phys. **62** (1999) 187.

[Worthington 88] Worthington T K *et al.*, Physica C **153-155** (1988) 32.

[Welp 89] Welp U *et al.*, Phys. Rev. Lett. **62** (1989) 1908.

[Werthamer 66] Werthamer N R *et al.*, Phys. Rev. **147** (1966) 295.

[Wu 00] Wu X F *et al.*, Physica C **333** (2000) 207.

[Xu 95, 96, 96A] Xu J H *et al.*, Phys. Rev. B **52** (1995) 7663; **53** (1996) R2991; Int. J. Mod. Phys. B **10** (1996) 2699.

[Yang 93, 93A, 96] Yang G *et al.*, Phys. Rev. B **48** (1993) 16873; IEEE Trans. Appl. Supercond. **3** (1993) 1663; Physica C **260** (1996) 103.

[Yaouanc 97, 97A] Yaouanc A *et al.*, Phys. Rev. B **55** (1997) 11107; cond-mat/9704159.

[Zakharov 00] Zakharov A A *et al.*, Phys. Rev. B **61** (2000) 115.

[Zavaritsky 00] Zavaritsky V N *et al.*, cond-mat/0006089.

[Zeldov 95] Zeldov E *et al.*, Europhys. Lett. **30** (1995) 367; Nature (London) **375** (1995) 373.

[Zhou 95] Zhou R *et al.*, Physica C **249** (1995) 166.

VITA

Xuewen Wan

Xuewen Wan was born on Dec. 12, 1968 (monkey year) to his parents, Mr. Wenpeng Wan and Mrs. Shuzheng Wang, in Huangshi, Hubei Province, P. R. China. He is the youngest of four children. He entered Nanhu Elementary School in 1975, Huangshi Junior High School in 1980 and Senior High School in 1983. In August 1986, he began studying in Fudan University, Shanghai and completed his B.S. in Applied Physics in June 1990. Upon graduation, he studied and worked in the National Accelerator Laboratory of Atomic and Molecular Physics, specializing on the Rutherford BackScattering (RBS) technique and received his M.A. in Nuclear Physics in 1993.

From August 1993 until July 1995, he worked in Shanghai Medical Instrument College as a teacher and research assistant specializing on the Computer Tomography (CT) and Nuclear Magnetic Resonance (NMR) techniques where he was a member of the Chinese Instrument Society.

In July 1995, he was admitted to Virginia State University, Petersburg, VA to fulfill his career dream in the United States. He was the Vice-President of the Society of Physics Students (SPS), a student member of the American Physical Society (APS) and the Mathematics Association of America (MAA). He got his M.S. in physics in 1997.

Since August 1997, he has been studying in the physics department at the College of William and Mary, Williamsburg, VA toward his Ph.D. in physics specializing on Muon

Spin Relaxation (μSR) technique. He participated various extracurricular activities. He was the 1999-2000 Term President of the Chinese Student and Scholar Association (CSSA) and a founding member of Tai Chi Club.

He was baptized on the Easter of 1998 at the Peninsula Chinese Baptist Church and married with Joanne Juan Zhou in Dec. 1999 and living happily in Williamsburg since then.